Doctoral Dissertation

Synthesis and Applications of Biomimetic Monolithic Materials

生体模倣型モノリス材料の合成と応用

ZHANG LUWEI

June 2022

Graduate School of Engineering

Osaka University

Contents

General Introduction

Biomimicry

Throughout hundreds of millions of years of sifting, nature has evolved many strategies that is worthy learning. There are many organisms with special structures that exhibit superior performance. These unique structures provide diverse inspirations for humans in many fields containing architecture, transport and materials. The discipline of mimicking living things to create artificial structures is known as bionics, a concept first introduced by J. Steele in 1960. Biomimetic materials science is an emerging discipline that applies the concept of biomimicry to materials science, mainly involving biology, chemistry, physics, and materials engineering. The aim of biomimetic materials science is to mimic the structure and characteristics of living organisms at the macroscopic or microscopic molecular level in order to obtain superior properties for applications. It has been found that some natural materials have excellent properties in terms of material transport and mechanical properties. For example, nacre structures have extremely strong mechanical strength, honeycomb-like duct in the xylem of plants exhibit high material transport efficiency, and corals possess good mechanical strength and high material transport efficiency. These natural structures have inspired researchers in biomimetics.

Nacre structure

Among the various biological structures in nature, bio-mineralization including bones, teeth, and pearls have become a hot topic in biomimetic materials science. Because there are many unique microstructures in bio-mineralization, and they utilize few substances to evolve optimum status after being selected by nature which is difficult to achieve with conventional artificial materials.[1, 2] As previously reported, the elastic modulus of nacre is commonly found in the shells of shellfishes and is composed of 95%

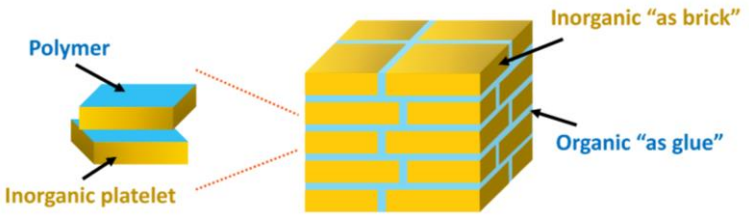

Figure 1. Nacre-like structure.[7]

aragonite ($CaCO_3$) and 5% organic proteins (silk fibroins, chitin, etc.).[3] However, the fracture toughness of nacre is more than 3000 times that of pure aragonite.[4] It is benefit from benefit from the stacked "brick-mud" structure in nacre.[5, 6] Nacre possesses a lamellar structure with the level submicron constructed by a two-dimensional lamellar $CaCO_3$ and one-dimensional proteins, and its cross-sectional morphology is similar to that of a common brick wall (**Figure 1**).[7] In the lamellar structure with the level submicron, the thickness and diameter of the $CaCO_3$ as “brick” are respectively around 500 nm and 6.5 μm, and the thickness of the protein as “mud” is approximately 25 nm. Herein, nacre structure has been widely studied owing to its excellent mechanical properties.

Honeycomb structure

In order to survive and reproduce, bees have built amazing honeycomb with delicate structure. Due to the robust mechanical properties of honeycomb structures, they have been intensively studied in the field of materials science. According to the honeycomb, researchers have developed bionic honeycomb concrete, foam rubber, foam glass, bionic honeycomb tyre and other high-performance materials which were used in construction, transport, aerospace, and other applications.[8-10] In addition, permeable pores with honeycomb-like structure are also found in the xylem of plants, where they are used for the rapid transport of water and nutrients. As the honeycomb-like macropore structure is suitable for the introduction of mesopores or micropores to form hierarchically porous structure, honeycomb-like biomimetic materials possess great potential in adsorption applications. K.P. Gadkaree *et al.* prepared an activated carbon with a honeycomb structure and applied it for the adsorption of butane, toluene, formaldehyde, and isopropanol.[11]

Coral structure

Over 500 million years, some corals have evolved unique dendritic structures that facilitate to the interaction between their skeletal structure and seawater in favor of their predatory behavior from flowing water.[12] This predatory behavior of corals is very similar to the behavior of porous materials that adsorb dyes, organic substances, and heavy metal ions from solution. Furthermore, the dendritic structure of corals contributes to increase specific surface area and

facilitates the passage of liquids.[13] As nacre, corals utilize the combination of inorganic matter and low amount of organic matter to obtain stronger mechanical strength.[14] Inspired by these properties of coral, researchers have synthesized some bionic materials with coral-like structure for practical applications such as evaporating seawater.[15] Moreover, the dendritic skeletal structure in bionic coral-like material facilitates the introduction of mesopores or micropores to build hierarchically pore, making the material is suitable for adsorption applications.

Protein phosphorylation and glycosylation

Protein is the main bearers and the most direct performers of biological functions, which plays a very important role in human's life activities. Since the 1990s, the main orientation of researchers was moving to postgenomic (proteome) and the exploration of gene function. Protein is the expression product of gene, and thus the investigation of protein is an extension and complement to genomics. Subsequently, proteomics was conceived in response. By the analysis and study of protein expression, translation, and post-translational modifications (PTMs), the researchers can obtain the linkages between protein structure and biological function. PTMs are chemical modifications, side chain processing and other processes of protein precursors, which endow multiple life functions on proteins. Among the more than 300 known PTMs, protein phosphorylation and glycosylation are considered to be two of the most important and widely studied. Almost all cellular activities are regulated by phosphorylation.[16-19] It have been found that abnormal protein phosphorylation strongly associated with more than 400 diseases, including cancer and diabetes.[20-24] Studying protein phosphorylation can provide significant information for identifying cancer markers and developing drugs. Moreover, more than 50% of proteins in human can be modified by glycosylation, and the polysaccharide chains linked to glycosylated proteins are involved in a variety of important life processes.[25, 26] Similarly, abnormal protein glycosylation is strongly associated with many cancers, neurological disorders, and Alzheimer's disease.[27-30] In addition, studies on novel coronavirus disease (COVID-2019) have shown that glycosylated proteins on the surface of coronaviruses play a crucial role when virus invade cells, and these glycosylated proteins are major antibodies.[31, 32] To date, the majority of identified disease markers are glycosylated proteins.[33,

[34] Therefore, the study of protein phosphorylation and glycosylation shows important significance.

Analysis of phosphorylation and glycosylation

At present, in common analytical approach used to explore protein phosphorylation and glycosylation, firstly, proteins are digested into peptides, and then the mass spectrometry (MS) was employed to analyze peptides. It was known as the bottom-up strategy. However, due to the low abundance of phosphopeptides and glycopeptides in protein digestion, a large number of signals from non-phosphopeptide and non-glycopeptide can interfere with the signals of phosphopeptide and glycopeptide, making it difficult to analyze protein digestion directly using MS. Therefore, the development of specific enrichment methods for the analysis of protein phosphorylation and glycosylation is greatly important meaning. Currently, the methods for phosphopeptide enrichment include metal oxide affinity chromatography (MOAC), immobilized metal affinity chromatography (IMAC) and immunoaffinity chromatography (IAC).[35-37] Among these methods, IMAC is the most widely used method for phosphopeptide enrichment because of its high specificity and low steric hindrance effect. In IMAC, phosphopeptides are enriched by static adsorption and chelation between phosphate groups of phosphopeptides and metal ions (**Figure 2**).[38, 39] On the other hand, glycopeptides are commonly enriched by lectin affinity chromatography, hydrazine chemistry, borate chemistry and hydrophilic interaction chromatography (HILIC).[40, 41] Among these strategies, HILIC exhibits many advantages, such as its ability to enrich for a variety of glycopeptides, retaining intact oligosaccharide chain information. Compared with non-glycopeptides, glycopeptides with saccharide chain exhibit

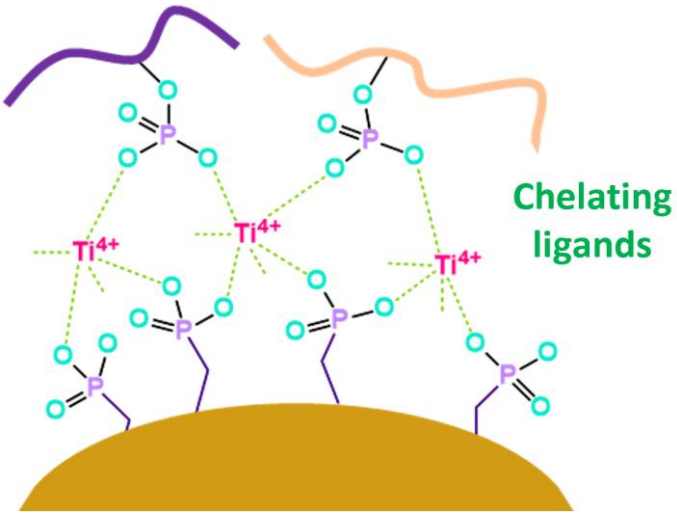

Figure 2. Mechanism of enriching phosphopeptide by IMAC.[39]

stronger hydrophilicity that can be selectively enriched by hydrophilic materials in HILIC (**Figure 3**).[42]

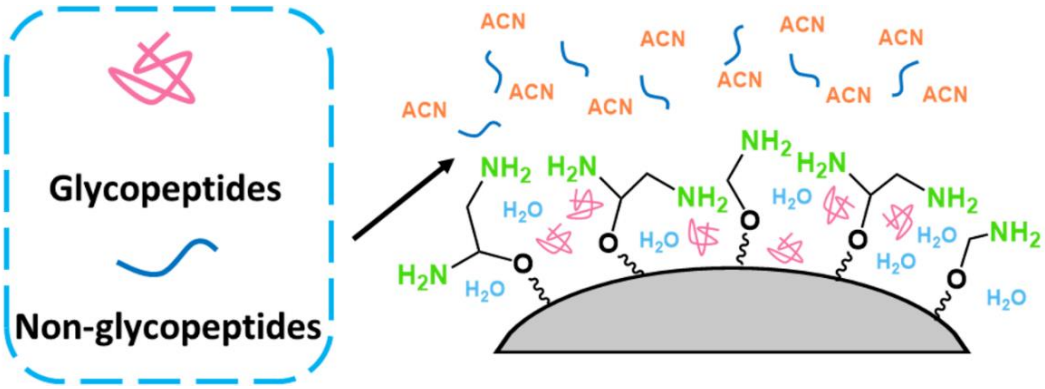

Figure 3. Mechanism of enriching glycopeptides by HILIC.[42]

Wastewater treatment

Since the industrial revolution, human activities exerted profoundly negative impact on the Earth's ecosystem and produced large amount of hazardous waste.[43-45] Currently, nearly two-thirds of the world's population are facing water scarcity, which is likely to continue for decades.[46] On the other hand, industry and agriculture have a huge demand for water and inevitably continue to produce effluent containing heavy metal ion. Heavy metal ions are common and highly toxic contaminants in water and include lead (Pb), arsenic (As), mercury (Hg), cadmium (Cd), copper and chromium (Cr).[47] Heavy metal ions in the aqueous environment mainly originate from industrial wastewater from mining, electroplating, chemical, battery manufacturing and paper industries.[48] Once heavy metals with potentially carcinogenicity enter the water environment, they pose a serious threat to human health and ecosystem balance.[49] Because heavy metals are biodegradable and can be enriched thousands of times by the biomagnification of the food chain.[50, 51] For instance, if heavy metals accumulate in seafood and crops what human eat, the heavy metals can enter the human body. These heavy metals can interact strongly with proteins and enzymes to render them inactive, or may accumulate in certain organs of human, causing chronic poisoning or even triggering death.[52] Therefore, the treatment of heavy metal ions in sewage has great significance in ecological environment.

Outline of this dissertation

In this study, biomimetic monoliths based on cellulose or chitosan were mainly investigated. Through modifying TiO_2, Ti^{4+} and COF on the surface of biomimetic monoliths, these materials have good application potential in enrichment of glycopeptides and phosphopeptides, and heavy metal adsorption.

Chapter 1

In this chapter, cellulose, as a promising, sustainable, and renewable carbon source was chosen as support to prepare a TiO_2-CM with a coral-like structure and nacre-like composition that was applied in enriching phosphopeptides. TiO_2-CM exhibited high surface area and mechanical strength. Because of the increased mechanical strength, the prepared TiO_2-CM is not expected to break during the enrichment process, thus preventing the complicated operation involving multiple centrifugation cycles. The TiO_2-CM exhibited great reusability, contributing to potential application toward the analysis of protein phosphorylation.

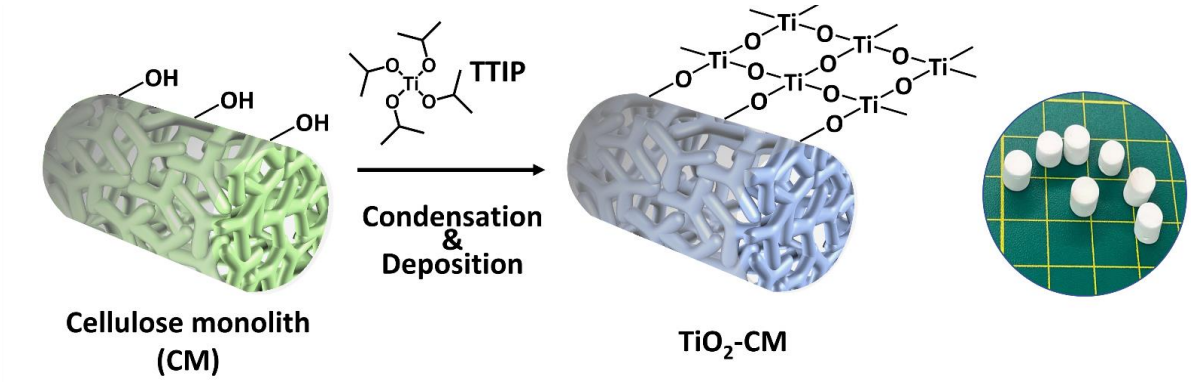

Scheme 1. Schematic illustration for preparation of the TiO_2-CM.

Chapter 2

In this chapter, a Ti^{4+}-phosphorylated cellulose monolith (TiPCM) with a coral-like structure was fabricated for the enrichment of phosphorylated and glycosylated peptides. The phosphorylated cellulose was prepared *via* an esterification reaction, after which the titanium ion (Ti^{4+}) was modified on the surface of its skeleton *via* chelation between the Ti^{4+} and the phosphate group. A large number of phosphate groups on the surface of the TiPCM clearly advanced the hydrophilicity of the cellulose monolith, offering many sites to chelate Ti^{4+}. The resulting TiPCM exhibits satisfactory performance in the analysis of protein phosphorylation

and glycosylation.

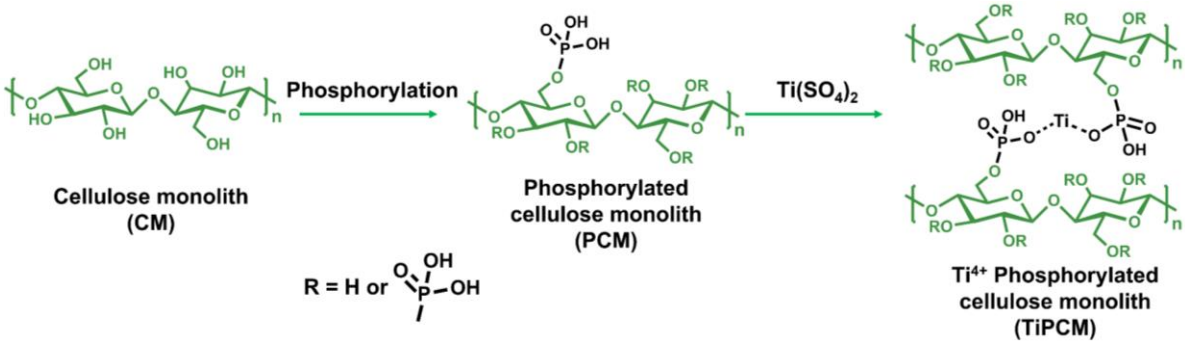

Scheme 2. Schematic illustration for preparation of the TiPCM.

Chapter 3

In Chapter 3, a COF-loaded biomimetic chitosan monolith (ChM) with honeycomb-like structure (ChM-COF) was fabricated, using chitosan, poly(ethylene glycol) diglycidyl ether (PEGDE), 1,3,5-triformylphloroglucinol (TP), oxalyldihydrazide (ODH) and acetic acid as catalyst in the presence of mesitylene and 1,4-dioxane (the structure of the COF is shown in **Fig. 3-1**). The resulting ChM-COF are monolithic materials to overcome disadvantages of COF powder. More importantly, it possessed hierarchical porous structure containing mesoporous and macroporous structure and higher specific surface area. Benefiting from its hierarchical porous structure, ChM-COF showed favorable performance in heavy metal adsorption.

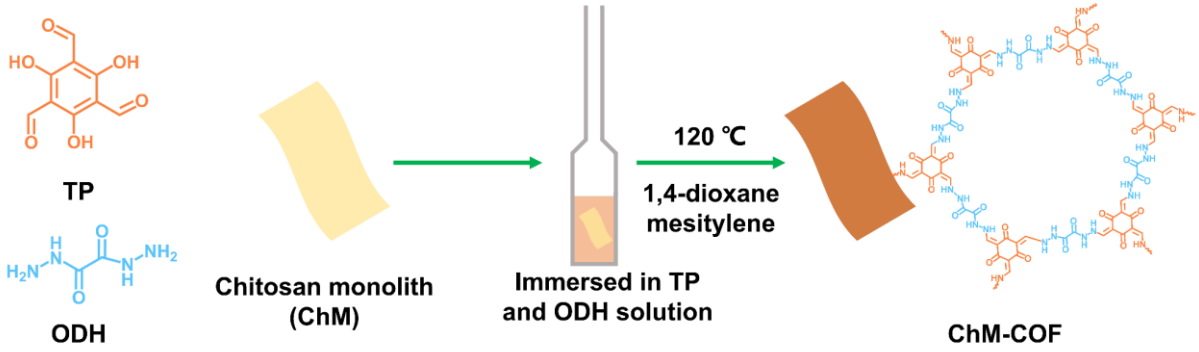

Scheme 3. Schematic illustration for preparation of ChM-COF.

References

1. B. L. Zhou, *Mater. Chem. Phys.* 1996, **45**, 114–119.
2. M. Shahinpoor, *Electrochimica Acta* 2003, **48**, 2343–2353.
3. W. Cui, M. Li, J. Liu, B. Wang, C. Zhang, L. Jiang and Q. Cheng, *ACS Nano* 2014, **8**, 9511–9517.
4. D. R. Katti and K. S. Katti, *J. Mater. Sci.* 2001, **36**, 1411–1417.
5. H. Nakahara, G. Bevelander and M. Kakei, *Jap. Jour. Malae.* 1982, **41**, 33–46.
6. T. E. Schaffer, C. Ionescu-Zanetti, R. Proksch, M. Fritz, D. A. Walters, N. Almqvist, C. M. Zaremba, A. M. Belcher, B. L. Smith, G. D. Stucky, D. E. Morse and P. K. Hansma, *Chem. Mater.* 1997, **9**, 1731–1740.
7. M. Bauchy, M. J. Qomi, F. J. Ulm and R. J. Pellenq, *J Chem Phys* 2014, **140**, 214503.
8. X. Jin, T. Jin, B. Su, Z. Wang, J. Ning and X. Shu, *Journal of Sandwich Structures & Materials* 2017, **19**, 544–571.
9. D. U. Tulyaganov, H. R. Fernandes, S. Agathopoulos and J. M. F. Ferreira, *Journal of Porous Materials* 2006, **13**, 133–139.
10. Y. Zhang, Z. Zong, Q. Liu, J. Ma, Y. Wu and Q. Li, *Materials & Design* 2017, **117**, 396–408.
11. K. P. Gadkaree, *Carbon* 1997, **36**, 981–989.
12. B. Riegl, A. Bruckner, S. L. Coles, P. Renaud and R. E. Dodge, *Ann. N. Y. Acad. Sci.* 2009, **1162**, 136–186.
13. E. Tambutte, S. Tambutte, N. Segonds, D. Zoccola, A. Venn, J. Erez and D. Allemand, *Proc Biol Sci* 2012, **279**, 19–27.
14. L. Ma, Z. Li, J. Liu, L. Duan and J. Wu, *Constr. Build. Mater.* 2019, **199**, 244–255.
15. Z. Zheng, H. Li, X. Zhang, H. Jiang, X. Geng, S. Li, H. Tu, X. Cheng, P. Yang and Y. Wan, *Nano Energy* 2020, **68**, 104298.
16. A. J. Whitmarsh and R. J. Davis, *Science* 2016, **354**, 180–181.
17. P. Cohen, *Nature* 1982, **296**, 613–620.

18. P. Cohen, *Nat. Cell. Biol.* 2002, **4**, 128–130.
19. E. J. Nestler and P. Greengard, *Nature* 1983, **305**, 583–588.
20. P. Cohen, *Eur. J. Biochem.* 2001, **268**, 5001–5010.
21. A. S. Gajadhar, H. Johnson, R. J. Slebos, K. Shaddox, K. Wiles, M. K. Washington, A. J. Herline, D. A. Levine, D. C. Liebler and F. M. White C, *Cancer Res.* 2015, **75**, 1495–1503.
22. G. Giamas, Y. L. Man, H. Hirner, J. Bischof, K. Kramer, K. Khan, S. S. Ahmed, J. Stebbing and U. Knippschild, *Cell Signal* 2010, **22**, 984–1002.
23. Y. Jiang, A. Sun, Y. Zhao, W. Ying, H. Sun, X. Yang, B. Xing, W. Sun, L. Ren, B. Hu, C. Li, L. Zhang, G. Qin, M. Zhang, N. Chen, M. Zhang, Y. Huang, J. Zhou, Y. Zhao, M. Liu, X. Zhu, Y. Qiu, Y. Sun, C. Huang, M. Yan, M. Wang, W. Liu, F. Tian, H. Xu, J. Zhou, Z. Wu, T. Shi, W. Zhu, J. Qin, L. Xie, J. Fan, X. Qian and F. He, *Nature* 2019, **567**, 257–261.
24. P. Blume-Jensen and T. Hunter, *Nature* 2001, **411**, 355–365.
25. A. Helenius and M. Aebi, *Science* 1989, **245**, 2364–2369.
26. Y. Tian, Y. Zhou, S. Elliott, R. Aebersold and H. Zhang, *Nat. Protoc.* 2007, **2**, 334–339.
27. H. H. Freeze, *J. Biol. Chem.* 2013, **288**, 6936–6945.
28. S. Hakomori, *Cancer. Res.* 1985, **45**, 2405–2414.
29. S. S. Pinho and C. A. Reis, *Nat. Rev. Cancer* 2015, **15**, 540–555.
30. C. A. Reis, H. Osorio, L. Silva, C. Gomes and L. David, *J. Clin. Pathol.* 2010, **63**, 322–329.
31. CPE Team, *Cell* 2020, **180**, 1.
32. S. Kumar, V. K. Maurya, A. K. Prasad, M. L. B. Bhatt and S. K. Saxena, *Virusdisease* 2020, **31**, 13–21.
33. G. Durand and N. Seta, *Clin. Chem.* 2000, **46**, 795–805.
34. T. M. Block, M. Comunale, M. Lowman, L. F. Steel, P. R. Romano, C. Fimmel, B. C. Tennant, W. T. London, A. A. Evans, B. S. Blumberg, R. A. Dwek, T. S. Mattu and A. S. Mehta, *P. Natl. Acad. Sci. USA.* 2004, **102**, 779–784.
35. Y. Hu, B. Jiang, Y. Weng, Z. Sui, B. Zhao, Y. Chen, L. Liu, Q. Wu, Z. Liang, L. Zhang and Y. Zhang, *Nat. Commun.* 2020, **11**, 6226.

36. A. Leitner, *TrAC, Trends Anal. Chem.* 2010, **29**, 177–185.
37. M. P. Stokes, C. L. Farnsworth, A. Moritz, J. C. Silva, X. Jia, K. A. Lee, A. Guo, R. D. Polakiewicz and M. J. Comb, *Mol. Cell. Proteomics* 2012, **11**, 187–201.
38. J. Porath, *TrAC - Trends Anal. Chem.* 1988, **7**, 254–259.
39. H. Zhou, M. Ye, J. Dong, E. Corradini, A. Cristobal, A. J. Heck, H. Zou and S. Mohammed, *Nat. Protoc.* 2013, **8**, 461–480.
40. H. Zhang, X. Li, D. B. Martin and R. Aebersold, *Nat. Biotechnol.* 2003, **21**, 660–666.
41. S. Mysling, G. Palmisano, P. Højrup and M. Thaysen-Andersen, *Anal. Chem.* 2010, **82**, 5598–5609.
42. X.-S. Li, G.-T. Zhu, Y.-B. Luo, B.-F. Yuan and Y.-Q. Feng, *TrAC, Trends Anal. Chem.* 2013, **45**, 233–247.
43. Q. Gao, J. Xu and X.-H. Bu, *Coord. Chem. Rev.* 2019, **378**, 17–31.
44. X. Tu, F. Gao, X. Ma, J. Zou, Y. Yu, M. Li, F. Qu, X. Huang and L. Lu, *J. Hazard. Mater.* 2020, **396**, 122776.
45. Y. Xu, T. Liu, Y. Zhang, F. Ge, R. M. Steel and L. Sun, *J. Mater. Chem. A* 2017, **5**, 12001–12014.
46. M. Mon, R. Bruno, J. Ferrando-Soria, D. Armentano and E. Pardo, *J. Mater. Chem. A* 2018, **6**, 4912–4947.
47. P. Samanta, A. V. Desai, S. Sharma, P. Chandra and S. K. Ghosh, *Inorg. Chem.* 2018, **57**, 2360–2364.
48. J. Li, X. Wang, G. Zhao, C. Chen, Z. Chai, A. Alsaedi, T. Hayat and X. Wang, *Chem. Soc. Rev.* 2018, **47**, 2322–2356.
49. J. Wen, Y. Fang and G. Zeng, *Chemosphere* 2018, **201**, 627–643.
50. F. Li, X. Wang, T. Yuan and R. Sun, *J. Mater. Chem. A* 2016, **4**, 11888–11896.
51. S. Venkateswarlu, A. Panda, E. Kim and M. Yoon, *ACS Appl. Nano Mater.* 2018, **1**, 4198–4210.
52. M. Feng, P. Zhang, H. C. Zhou and V. K. Sharma, *Chemosphere* 2018, **209**, 783–800.

Chapter 1.

Robust dual-biomimetic titanium dioxide-cellulose monolith for enrichment of phosphopeptide

1.1 Introduction

Phosphorylation plays a crucial regulatory role in almost all cellular activities; hence, it is extensively being studied.[1-4] Abnormal phosphorylation processes may be the direct or indirect cause of more than 400 diseases, including cancer and diabetes.[5-8] Therefore, the study of protein phosphorylation is highly significant because it may provide vital information for humans to identify cancer markers and discover drug targets.[9-11] However, because of the low abundance of phosphorylated peptides obtained through protein digestion, numerous signals from non-phosphopeptides interfere with those of phosphopeptides.[12] Thus, the development of an enrichment method with specificity for the analysis of protein phosphorylation is highly significant. Among the common enrichment techniques, the material immobilized Ti^{4+} ions were widely applied in immobilized metal affinity chromatography (IMAC).[13-17] Metal oxide affinity chromatography (MOAC) serves as a good substitute for IMAC and is conducted using commonly available compounds such as ZrO_2, Ga_2O_3, Al_2O_3, Fe_3O_4, and TiO_2.[18] However, most of the materials applied in the MOAC-based enrichment of phosphopeptides are powders; thus, this process undesirably necessitates multiple centrifugation cycles to be run during the enrichment process.[19] Thus, the development of monolithic materials for phosphopeptide enrichment is significant.

In general, biomimetic materials show excellent properties.[20-22] Zhao *et al.* prepared a material with a biomimetic nacre structure through combining organic and inorganic substances.[23] The resultant biomimetic material showed strong mechanical properties and overcame the low mechanical strength of inorganic aerogel materials. In addition, the enrichment behavior of biomimetic materials toward peptides in the solution is similar to that of predatory corals in flowing seawater. Therefore, in a previous study, our group fabricated a biomimetic Ti^{4+}-phosphorylated cellulose monolith (TiPCM) that mimicked the structure of corals and applied it in the enrichment processes of glycopeptides and phosphopeptides.[24] The crystal region of the cellulose monolith (CM) was destroyed during the process of phosphorylation and modification using Ti^{4+} ions on the CM surface, and significantly decreased the specific surface area and mechanical strength of the resultant material.

In this study, cellulose, as a promising, sustainable, and renewable carbon source was chosen as support to prepare a titanium dioxide-cellulose monolith (TiO_2-CM) material with a coral-like structure and apply it to enrich phosphopeptides. In comparison to a previously studied TiPCM material, the as-prepared TiO_2-CM material exhibited higher surface area and mechanical strength. Because of the increased mechanical strength, the prepared TiO_2-CM material is not expected to break during the enrichment process, thus preventing the complicated operation involving multiple centrifugation cycles. Most importantly, this preparation process is green, gentle, and simple, and the as-prepared TiO_2-CM material with reusability is expected to show good potential toward the analysis of protein phosphorylation.

1.2 Experimental Section

1.2.1 Chemicals and materials

Cellulose acetate (CA, L30) with an acetylation degree of 55% was provided by Daicel Co., Ltd. (Osaka, Japan). Sodium hydroxide (NaOH), ammonium bicarbonate (NH_4HCO_3), ammonium hydroxide ($NH_3 \cdot H_2O$), acetonitrile (ACN), triethylamine (TEA), titanium isopropoxide (TTIP), 2,5-dihydroxybenzoic acid (DHB), glutamate, isopropyl alcohol, dimethylformamide (DMF), and titanium oxide (TiO_2) were purchased from Fujifilm Wako Pure Chemical Corp. (Osaka, Japan). Dithiothreitol (DTT), iodoacetamide (IAA), β-casein, bovine albumin (BSA), trypsin, and trifluoroacetic acid (TFA) were obtained from Sigma-Aldrich Co. LLC (St Louis, MO, USA). Commercial TiO_2 beads (10 μm) were purchased from GL Sciences Inc. (Tokyo, Japan). Deionized water used in the study was doubly distilled and purified using the Milli-Q system from Millipore Corp. (Milford, MA, USA).

1.2.2 Preparation of TiO_2-CM material

As shown in **Scheme 1-1a**, in the first step, the CM material was fabricated according to the method in our group's earlier study.[25] The typical process of preparation was briefly stated as follows. DMF was selected as the good solvent to completely dissolve a certain mass of CA at 90 ℃. Hexanol as the poor solvent, was slowly dropped into the above-mentioned solution accompanied by strong stirring. After the solution became homogeneous and transparent, it was placed in a water bath at 20 ℃ for 24 h to achieve thermally induced phase separation (TIPS). The sample was washed three times using ethanol to remove residuals and dried using a vacuum dryer to attain the CA monolith. The NaOH aqueous solution (0.5 mol L^{-1}) was employed to hydrolyze the CA monolith. The sample was then washed with deionized water and dried under vacuum to obtain the CM material. In the second step, the TiO_2-CM material was prepared *via* a sol–gel reaction where the CM material was the supporter.[26] Briefly, isopropyl alcohol was used to homogeneously disperse the TTIP with stirring. The prepared CM material was then immersed into the TTIP/isopropyl alcohol mixture, and deionized water was dropped into the mixture under vigorous stirring. The mixture was then heated to 80 °C for 5 h and cooled to

room temperature. The cooled mixture was washed with distilled water and completely dried to obtain the TiO_2-CM material.

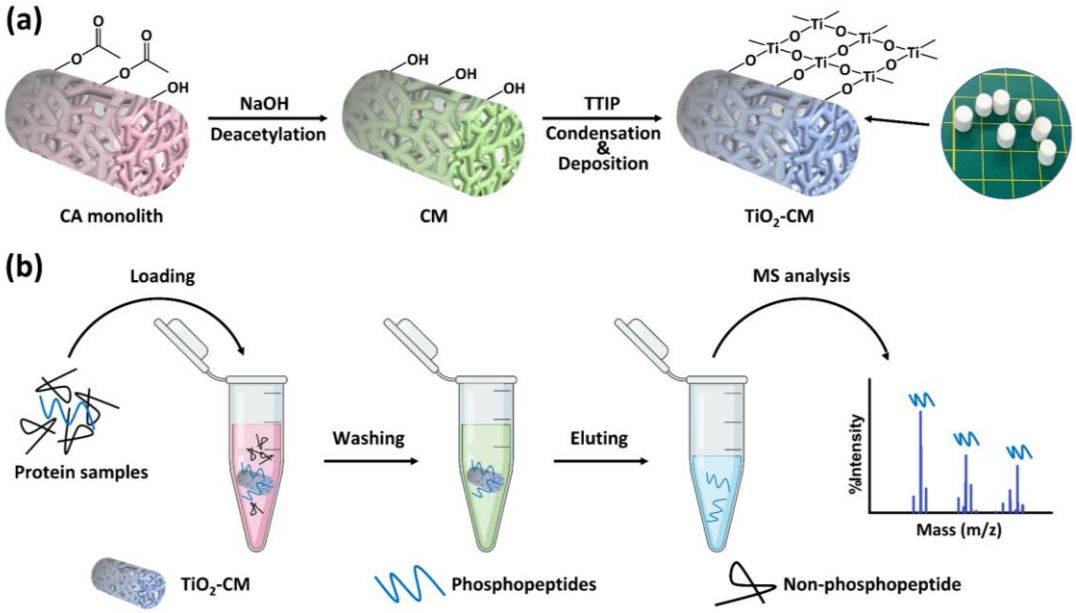

Scheme 1-1. (a) Preparation of the TiO_2-CM material. (b) Workflow of the enrichment process of phosphopeptides. (The length and diameter of TiO_2-CM in the photo are 8 and 6 mm, respectively)

1.2.3 Instruments and methods

The pore structures and morphologies of the materials were observed using scanning electron microscopy (SEM, Hitachi S-3000N, Tokyo, Japan). The thermal stabilities of the materials were investigated through thermogravimetric analysis (TGA, Hitachi TG/DTA7200, Tokyo, Japan). The surface chemistries of the materials were investigated using X-ray photoelectron spectroscopy (XPS, JEOL JPS-9010MC) with monochromatized Al-Kα radiation (1486.6 eV). The X-ray photoelectron spectra of the materials were collected at fixed analyzer pass energies of 160 eV and 10 eV, with binding energies of the C 1s peak C-H (sp3) Cs set at 284.8 eV. The surface elemental composition of the monoliths was measured using energy-dispersive X-ray spectroscopy (EDX, HITACHI, Miniscope TM 3000 equipped with Swift ED

3000). The XRD patterns of the sample were acquired using an X-Pert diffractometer (wavelength = 1.54 Å, generator voltage = 45 kV, and generator current = 200 mA). The mechanical properties of the monoliths in a dried state were evaluated using the universal testing machine (EZ Graph, SHIMADZU) with a compression speed of one mm/min and the maximum compression strain (ε) maintained at 50%. The zeta potential of sample was determined by a zeta-potential and particle size analyzer (ELSZ-2000ZS, Otsuka Electronics). Attenuated total reflectance infrared (ATR-IR) spectroscopy was measured with a Nicolet iS5 spectrometer (Thermo Scientific, Yokohama, Japan) equipped with an iD5 ATR attachment.

1.2.4 Denaturation and enzymatic digestion of protein solutions

Two mg of the BSA (or β-casein, Hela cell exosomes) specimen was dissolved in the one ml denaturation solution composed of 8.0 mol L^{-1} urea and 0.1 mol L^{-1} ammonium bicarbonate, followed by the addition of the DTT solution (20 mmol L^{-1}). The mixture obtained was incubated at 60 °C for one h, and then incubated for a further 30 min in the dark and at room temperature after the addition of the IAA (7.4 mg). The resultant mixture was diluted eight times with the 0.1 mol L^{-1} ammonium bicarbonate solution, and trypsin (80 μg) was added into the mixture. The mixture was then incubated at 37 °C for 16 h. The pH value of the mixture was adjusted to approximately two to three using the 10% TFA aqueous solution. Solid phase extraction (SPE) was then performed on the mixture using the Oasis HLB 3 cc Vac Cartridge column purchased from Waters Co., Ltd. (USA). For subpackage, the peptide solution was eluted, dried under vacuum, and dissolved in the FA aqueous solution (0.1%, 2.0 mL) in sequence. After subpackaging the above solution, a freeze dryer was employed to dry the peptide solution, which was stored at −20 °C.

1.2.5 Enrichment process for phosphopeptides

The enrichment process for phosphopeptides is illustrated in **Scheme 1-1b**. The first step of this process was loading. For enriching phosphopeptides acquired through the tryptic digestions of standard proteins, the enrichment solution (Buffer 1, ACN/H_2O/TFA = 80/14/6, v/v/v, with saturated glutamic acid, 200 μL) was chosen and applied to wash 1 mg of the TiO_2-

CM material three times. Certain amounts of the β-casein or β-casein tryptic digests and the BSA tryptic digest were dissolved in Buffer 1 as the loading solution (200 μL), which was added to the above TiO_2-CM material washed with Buffer 1. A platform shaker was employed to incubate the mixture for 30 min at room temperature. The second step was washing. The TiO_2-CM material was washed using buffer washing solutions (Buffer 2, ACN/H_2O/TFA = 50/44/6, v/v/v, with saturated glutamic acid, 200 μL × 3; Buffer 3, ACN/H_2O/TFA = 30/69.9/0.1, v/v/v, 200 μL). The final step was eluting. The elution solution (10% $NH_3 \cdot H_2O$, 50 μL × 2) was chosen to obtain the captured phosphopeptides using the TiO_2-CM material at room temperature. Eventually, the MALDI-TOF system was employed to analyze the eluted solution.

The enrichment process of phosphopeptides from the complex biological sample (Hela cell exosomes) was as follows. The 500 μL Buffer 1 (ACN/H_2O/TFA = 80/14/6, v/v/v, with saturated glutamic acid) loading solution was employed to dissolve the lyophilized tryptic digest of the Hela cell exosomes (two mg), and 5 mg of the TiO_2-CM material was added into the solution. The resultant mixture was incubated using a platform shaker (30 min, room temperature). After loading the sample on the TiO_2-CM material, it was washed with buffer washing solutions (Buffer 2, ACN/H_2O/TFA = 50/44/6, v/v/v, with saturated glutamic acid, 500 μL × 3, Buffer 3, ACN/H_2O/TFA = 30/69.9/0.1, v/v/v, 500 μL). The eluent solution (10% $NH_3 \cdot H_2O$, 2 × 50 μL) was employed to elute the captured phosphopeptides from the tryptic digest of the Hela cell for 10 min at room temperature. The two eluting solutions obtained were sufficiently mixed and lyophilized, and LC-MS was adapted to analyze the product.

1.2.6 Collection of Hela cells exosome

Cell culture conditioned media was harvested from HeLa cells and centrifuged using a Beckman Optima XPN-100 Ultracentrifuge at 300 g at 4 ℃ for 10 min to remove detached cells. Supernatant was collected and filtered through 0.22 mm filters (Merck Millipore) to remove apoptotic bodies, microvesicles and cell debris. The filtered solution was then centrifuged at 100,000 × g at 4 ℃ for 90 min and the supernatant was carefully discarded, the pellet was resuspended in 1 ml ice-cold PBS using a micropipettor. Then a second round of the

same ultracentrifugation was carried out. The supernatant was removed, and the exosome containing pellet resuspended in 20 μL of PBS for protein digestion. We added the content in supporting information.

1.2.7 Mass spectrometry analysis

MALDI-TOF MS experiments were carried out in positive ion mode on a Autoflex III (Bruker, Germany). The sample solution (0.5 μL) and 0.5 μL DHB solution (25 $mg \cdot mL^{-1}$, ACN/H_2O/H_3PO_4, 70/29/1, v/v/v) were deposited in sequence on the MALDI plate for MS analysis.

Before LC-MS/MS analysis, the peptides were resuspended using 10μl of 0.1% FA aqueous solution and were loaded into an in-house-made 30 cm length reverse-phase column (150 nm id) packed with Ultimate XB-C18 1.9μm resin (Welch materials). The nano-LC-ESI-MS/MS analysis was performed using an U3000 Nano LC system connected to an Orbitrap Fusion Lumos Tribrid Mass Spectrometer (Thermo Fisher Scientific, USA) with an ESI nanospray source. The total flow rate was 600 nL min^{-1}, and binary solvents A (0.1% FA in H_2O) and B (80% ACN/0.1% FA in H_2O) were selected for elution. Gradient elution was performed as follows: 0 min, 6% B; 9 min, 10% B; 104 min, 28% B; 140min, 40% B; 142 min, 95% B; 150 min, 95% B. The spray voltage was set at 2.0 kV. All MS and MS/MS spectra were acquired in the data-dependent acquisition mode, and the full mass scan was acquired from m/z 300 to 1400 with a resolution of 120,000.

1.2.8 Data search of phosphopeptides

All the nano-LC-ESI-MS/MS raw data were searched using Proteome Discoverer software（version 2.4.1.15）with the SEQUEST algorithm. The mass tolerances were 20 ppm for initial precursor ions and 0.5 Da for-fragment ions against a UniProt Human database (December 2021, 20376). Two missed cleavages were allowed for trypsin, Carbamidomethylation（C）was set as a fixed modification, while oxidation (M), acetylation (protein N-term), and phosphorylation (S/T/Y) were set as variable modifications and the cut-off false discovery rate (FDR) for peptide identification was limited to ≤1%.

1.3 Results and discussion

1.3.1 Preparation and Characterization of the TiO2-CM material

Most mollusks have evolved hard shells composed of organic and inorganic components, to protect their soft bodies. Inspired by the shells of mollusks, we placed a layer of the TiO_2 onto the surface of the CM material with a coral-like structure. We expected to fabricate a TiO_2-CM material with good mechanical strength and high surface area because it possesses shell-like composition and coral-like structure. As described in our previous study, the enrichment process of phosphopeptides using materials in solution exhibited similar predatory behavior to the corals in seawater. The TiPCM material with a coral-like structure had shown an excellent ability to enrich glycopeptides and phosphopeptides.[24] However, its mechanical strength and surface area were lower than those of the precursor (CM) because the crystal structure of cellulose was destroyed during the phosphorylation and modification processes. Therefore, in this study, an organic-inorganic TiO_2-CM hybrid material was prepared by combining the inorganic TiO_2 with the organic CM skeleton and was found to imitate the structure of the mollusk shell. This significantly increased the surface area and mechanical strength of the material, while maintaining its coral-like structure. The TiO_2 layer on the surface of the CM material provided a large number of sites for phosphopeptides to adsorb and reduced the steric hindrance between the peptide and the material. Moreover, the TiO_2-CM material prepared did not break during the enrichment process because of its high mechanical strength and indicated that the enrichment process could finish without performing centrifugation. The addition of the TiO_2 layer onto the surface of the CM material greatly simplified the enrichment process.

To verify whether the TiO_2 had successfully coated onto the surface of the CM material, the crystalline structures of the CM, pure TiO_2, and TiO_2-CM samples were investigated using XRD analyses. The XRD pattern of the CM material showed the characteristic cellulose peak of (002) crystal faces at approximately 20° (as shown in **Figure 1-1a**). The peaks of (101), (112), (200), (105), (211), (204), (116), (220), (215) and (303) crystal faces were attributed to the anatase structure of the TiO_2. It is worth noting that in **Figure 1-1a** the signals of the CM and

TiO_2 appear in the XRD pattern of the TiO_2-CM material simultaneously and demonstrate that the TiO_2 was successfully coated onto the surface of the CM material to synthesize the TiO_2-CM material using the sol–gel reaction.

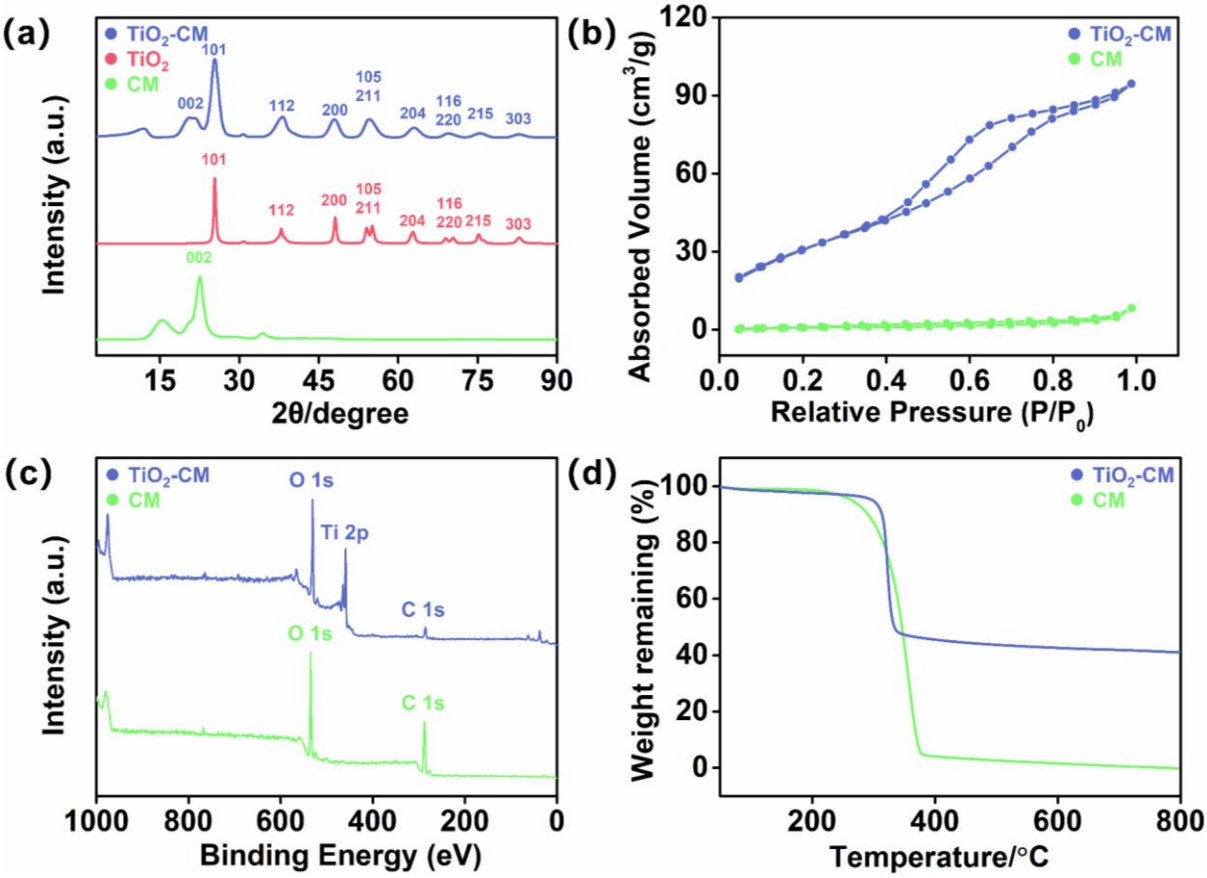

Figure 1-1. (a) XRD patterns of the TiO_2-CM, TiO_2 and CM samples. (b) N_2 adsorption-desorption isotherms, (c) XPS spectra, and (d) thermogravimetric curves at heating rates of 10 °C min^{-1} under nitrogen atmosphere of the TiO_2-CM and CM materials.

To determine whether the coral-like structure had been destroyed after the coating of the TiO_2 layer, the pore morphologies of the CM and TiO_2-CM materials were investigated using SEM. In **Figure 1-2a and b**, the SEM image of the CM material showed a dendritic skeletal structure that mimics a coral, and the wrinkled structure on the surface of its dendritic skeleton that resembles the coral surface is observed in the high magnification. As shown in **Figure 1-2c and d**, after the TiO_2 was evenly coated onto the surface of the CM material, its coral-like

structure was sustained into the TiO_2-CM material. In addition, the biomimetic coral-like structure of the resultant TiO_2-CM material was not only conducive to mass transfer between the material and the solution, but also effectively reduced the steric hindrance between the peptide and the material during the enrichment process of phosphopeptides.

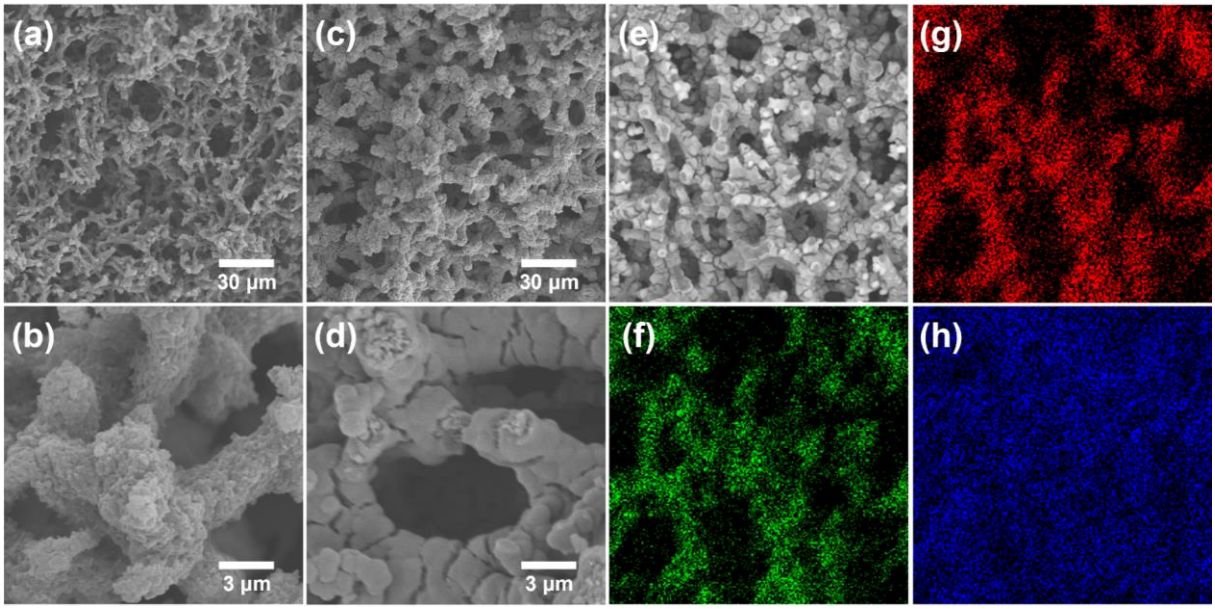

Figure 1-2. SEM images of the (a, b) CM and (c, d) TiO_2-CM materials (at 500×, 5000×, 500×, and 5000× magnification, respectively). Elemental mapping analysis showed (g) C, (f) O and (h) Ti elements distributed in the (e) TiO_2-CM materials.

As mentioned previously, the introduction of the TiO_2 onto the surface of the CM material was expected to increase the surface area of the resultant TiO_2-CM material. To confirm this, N_2 adsorption/desorption tests were performed on the materials to measure their pore size distributions and BET surface areas. As shown in the N_2 adsorption/desorption isotherms obtained, the surface area of the CM material was 2.7 m^2 g^{-1} (**Figure 1-1b**). After the introduction of the TiO_2 layer, the surface area of the TiO_2-CM material was significantly increased to 111.0 m^2 g^{-1}. Furthermore, the mean pore size of the CM material was 2.9 nm, and the mean pore size of the TiO_2-CM material had increased to 4.2 nm. The prepared TiO_2-CM material possessed a significantly higher surface area than the CM material and a larger pore

size, which provided more active sites and reduced steric hindrance between the peptides and the material during the enrichment process of phosphopeptides.

In addition, to further confirm the elemental composition of the TiO_2-CM material, the CM and TiO_2-CM materials were characterized using XPS. In the XPS spectrum of the CM material, only C and O elements were detected (as shown in **Figure 1-1c**). The XPS spectrum of the TiO_2-CM material showed an apparent peak attributed to the Ti element; however, the intensity of the peak corresponding to the C element in the TiO_2-CM material was lower than that of the C element in the CM material. These results indicated that a large quantity of the TiO_2 was coated onto the surface of the TiO_2-CM material. The atomic percentages (%) of the CM and TiO_2-CM material surfaces were determined using low-resolution XPS spectra and are shown in **Table 1-1**. The Ti atomic percentage on the TiO_2-CM surface was as high as 20.94%. Moreover, SEM-EDX was employed to investigate the distribution of Ti on the TiO_2-CM surface. As illustrated in **Figure 1-2e-h**, the distributions of the C, O, and Ti elements on the TiO_2-CM surface are consistent and very homogenous. This indicated that the TiO_2 was uniformly coated onto the surface of the CM material, which was consistent with the observations made using the SEM images.

Table 1-1. Elemental composition of XPS analysis of CM and TiO_2-CM sample based upon analysis of the survey spectra.

Peak	**Peak BE/eV**	**At. % (CM)**	**At. % (TiO_2-CM)**
C 1s	284.61	67.47	23.28
O 1s	531.61	32.53	55.78
Ti 2p	456.61	0	20.94

To verify the thermal stability of the TiO_2-CM material and determine its TiO_2 content, the CM and TiO_2-CM materials were characterized using TGA. As observed in **Figure 1-1d**, the CM material started to decompose at 220 °C and was almost completely decomposed at approximately 380 °C, with nothing remaining at 800 °C. Similar to the CM material, the TGA

curve of the TiO_2-CM material also showed apparent weight loss from 300 to 340 °C owing to the decomposition of cellulose at higher temperatures. However, the decomposition temperature of TiO_2-CM was 80 °C higher than CM, possibly caused by the crosslinking between hydroxyl group of cellulose and TiO_2. And the residual weight of the TiO_2-CM material above 800 °C was maintained at 40% because TiO_2 possesses extremely high thermal stability and remains stable even at a higher temperature. These results verified the successful preparation of the TiO_2-CM material and showed that its TiO_2 content was approximately 40%. The higher modification density of the TiO_2-CM material could provide more adsorption sites for enriching phosphopeptiedes.

By introducing the inorganic TiO_2 onto the organic CM material, we synthesize an inorganic-organic hybrid TiO_2-CM material with good mechanical properties such as a nacre-like composition. After they had completely dried, the CM, TiO_2-CM, and TiO_2 monoliths (TiO_2-CM removed CM template at 800 °C and resulted in a TiO_2 monolith) with the same shape were characterized using compression tests. As shown in **Figure 1-3**, the skeleton of the CM material was broken when subjected to a pressure of approximately 2.5 MPa, and that of the TiO_2-CM material was broken when subjected to a pressure of approximately 4.0 MPa. When compared, the compression curves of the TiO_2-CM and TiO_2 monoliths show that the mechanical strength of the TiO_2 monolith significantly reduced after the CM template was removed. Because the cellulose inside the material was removed at the high temperature and the nacre-like composition was destroyed. Similarly, in nature, nacre with high mechanical strength became fragile after high temperature treatment owing to losing support from organic substance. Meanwhile, with strains ranging

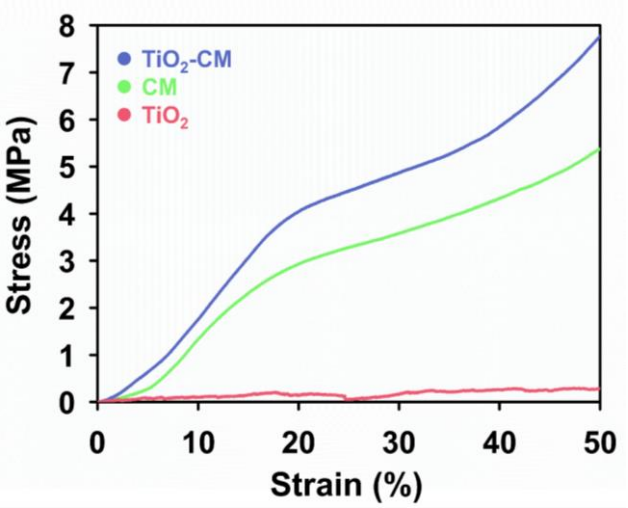

Figure 1-3. Mechanical strength test results of the dried TiO2-CM, CM and TiO2 monoliths compressed up to a 50% strain.

from 0 to 20%, it could be found that the values of the compressive modulus of TiO_2-CM was 22.6 MPa and higher than that of CM (17.5 MPa). These results demonstrated that the TiO_2-CM materials successfully mimicked the mollusk shell in terms of composition, where CM as the "organic glue" was used to fix the inorganic matter (TiO_2), and thereby produced "shells" with higher mechanical strengths. Two benefits to having a high mechanical strength were that the TiO_2-CM material did not shatter into powder during the enrichment process of phosphopeptides, and the enrichment process was carried out without the employment of centrifugation. This avoided the loss of materials and peptides experienced when using commercial TiO_2 microspheres, and significantly simplified the enrichment process.

1.3.2 Application in enriching phosphopeptides

The phosphate group of the phosphopeptide cooperated with the TiO_2 component of the TiO_2-CM material under acidic conditions. Thus, phosphopeptides were retained on the surface of the TiO_2-CM material, while non-phosphopeptides were eluted using the washing buffer solution. Then, the alkaline aqueous ammonia solution

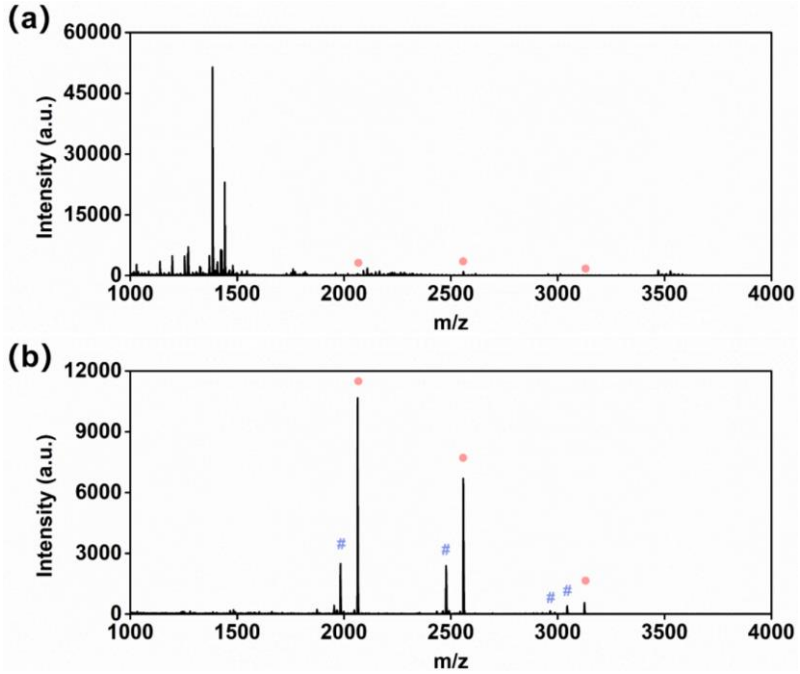

Figure 1-4. MALDI-TOF mass spectra of the tryptic digest of β-casein. (a) Direct analysis and (b) analysis after enrichment using TiO_2-CM. Phosphopeptide are peaks identified using the symbol ●, dephosphorylated peptide peaks are identified using the symbol #.

eluted the phosphopeptides enriched by the TiO_2-CM material, and the eluates were collected. It was worth noting that TiO_2 possesses a positive charge at low pH values. Therefore, when phosphopeptides with negative charges are enriched, a large quantity of acidic non-phosphopeptides will also be enriched. To reduce the interferences from non-phosphopeptides, DHB and glutamic acid were added in the loading and washing process to achieve competitive inhibition for the acidic non-phosphopeptides.[27-30] For the above reason, we investigated three different conditions for phosphopeptide enrichment: (1) The sample was loaded onto the prepared TiO_2-CM material using the ACN/H_2O/TFA (80/14/6, v/v/v) solution as the loading buffer, washed three times with the ACN/H_2O/TFA (50/44/6, v/v/v) solution, washed once with the ACN/H_2O/TFA (30/69.9/0.1, v/v/v) solution, and the peptides were then eluted using the 10% aqueous ammonia eluent, successively; (2) The sample was loaded onto the prepared TiO_2-CM material using the ACN/H_2O/TFA (80/14/6, v/v/v) loading buffer solution with added saturated glutamic acid, washed three times with the ACN/H_2O/TFA (50/44/6, v/v/v) solution with added saturated glutamic acid, washed once with the ACN/H_2O/TFA (30/69.9/0.1, v/v/v) solution, and the peptides were eluted using the 10% aqueous ammonia eluent in the correct order; (3) The saturated glutamic acid solution in (2) was changed to 20 mmol L^{-1} DHB aqueous solution, and the other conditions remained the same. The prepared TiO_2-CM and commercial TiO_2 materials were utilized separately in the enrichment processes of phosphopeptides obtained from the tryptic digests of β-casein, under the three different conditions. As shown in **Figure 1-4a**, the MALDI-TOF mass spectrum was directly adapted to analyze the tryptic digests of the β-casein before enrichment, and the signal from the phosphopeptides can hardly

be detected owing to the presence of the large quantity of non-phosphopeptides. After enrichment using the prepared TiO_2-CM and commercial TiO_2 materials under condition (1), respectively, the signals of the phosphopeptides were detected as shown in **Figure 1-5a** and **b**, however, at approximately 1250, 2000, 2500 and 3000 m/z, there are still interferences from the non-phosphopeptides. It is worth mentioning that the interferences of the non-phosphopeptides were less pronounced when the prepared TiO_2-CM material was used in the enrichment process, indicating that its enrichment performance was higher than that of the commercial TiO_2 material. This is because the cellulose in the TiO_2-CM material showed a negative charge under the acidic condition; thus, neutralizing part of the TiO_2 charge.[31] Furthermore, glutamic acid was introduced into the enrichment process. As shown in **Figure 1-5c** and **d**, the phosphopeptides were successfully enriched by the two materials (commercial TiO_2 and TiO_2-CM materials) from the tryptic digests of β-casein. In particularly, in **Figure 1-5d**, the signals of non-phosphopeptides had almost completely disappeared, which indicated that the TiO_2-CM material has a higher enrichment performance than the commercial TiO_2 material. Finally, DHB was introduced into the enrichment process. However, the introduction of DHB did not significantly improve the enrichment performance of either of the two materials. Therefore, we chose to employ condition (2) to enrich the phosphopeptides in the experiment that followed.

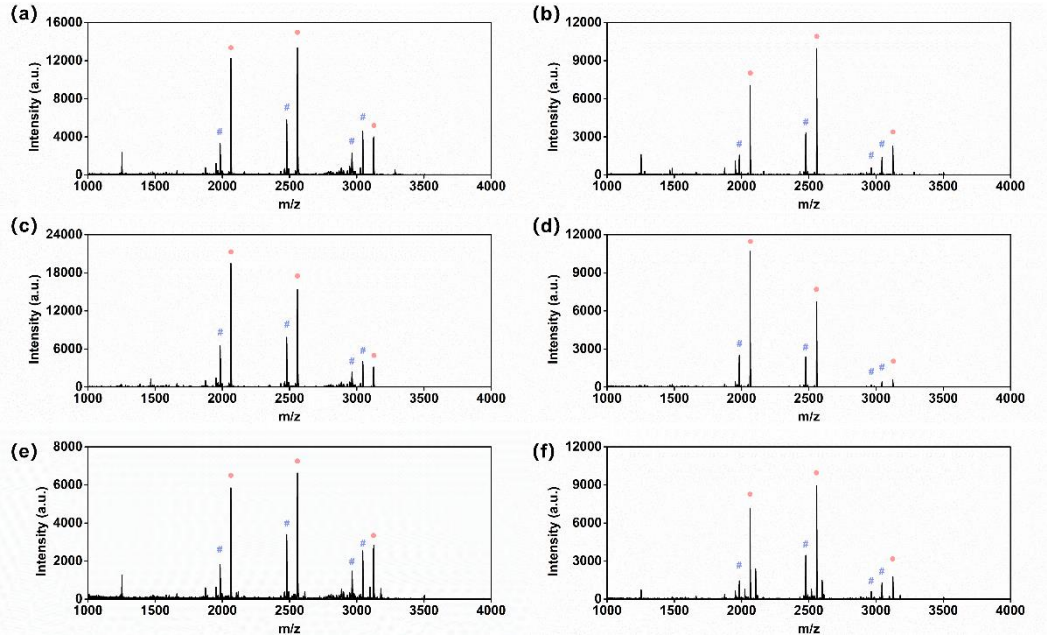

Figure 1-5. MALDI-TOF mass spectra of phosphopeptides from β-casein digest after enrichment by commercial TiO_2 material (a, c and e) and TiO_2-CM (b, d and f) with different condition. (a, b) ACN/H_2O/TFA (80/14/6, v/v/v) as loading buffer, washing with ACN/H_2O/TFA (50/44/6, v/v/v) 3 times, washing with ACN/H_2O/TFA (30/69.9/0.1, v/v/v) once, and eluting peptides using 10% aqueous ammonia. (c, d) ACN/H_2O/TFA (80/14/6, v/v/v) with saturated glutamic acid as loading buffer, washing with ACN/H_2O/TFA with saturated glutamic acid (50/44/6, v/v/v) 3 times, washing with ACN/H_2O/TFA (30/69.9/0.1, v/v/v) once, and eluting peptides using 10% aqueous ammonia. (e, f) ACN/H_2O/TFA (80/14/6, v/v/v) with 20 mmol L^{-1} DHB as loading buffer, washing with ACN/H_2O/TFA (50/44/6, v/v/v) with 20 mmol L^{-1} DHB 3 times, washing with ACN/H_2O/TFA (30/69.9/0.1, v/v/v) once, and eluting peptides using 10% aqueous ammonia. Phosphopeptide peaks identified are marked with the symbol "●", dephosphorylated peptide peaks identified are marked with the symbol "#".

To verify the enrichment ability of the TiO_2-CM material from standard proteins, the tryptic digest of β-casein was chosen to use in enriching phosphopeptides. As illustrated from **Figure 1-4a**, numerous signals from the non-phosphopeptides are detected in the tryptic digest of β-casein before the enrichment process, which seriously interferes with the signals of phosphopeptides. As a result, only three phosphopeptides with very low intensities were detected. After enrichment by TiO_2-CM, non-phosphopeptides are almost completely

undetectable, and only high intensity signals from the phosphopeptides are observed in **Figure 1-4b**. The results demonstrated that the TiO_2-CM material had enrichment abilities for phosphopeptides obtained from standard proteins.

The selectivities of the materials chosen for enriching phosphopeptides are crucial for their practical applications because of the complexities of biosamples. The tryptic digest of the BSA without phosphopeptides was added into the tryptic digest of the β-casein to increase the complexity of sample, which was used to investigate the selectivity of the resultant TiO_2-CM material. As illustrated in **Figure 1-6**, even if the quantity of the BSA digest increases to 500 times that of the β-casein, the TiO_2-CM material could still successfully enrich all three phosphopeptides from the complicated mixture. The phosphopeptide signals were less interfered with by those of the non-phosphopeptides and showed that the enrichment performance of the resultant TiO_2-CM material was higher than that of commercial TiO_2 material. Compared with similar materials used in MOAC and IMAC, TiO_2-CM material exhibited good selectivity on phosphopeptides.[32-36] This indicated that the resultant TiO_2-CM material possessed excellent selectivity for phosphopeptide enrichment and a stronger anti-interfering ability for non-phosphopeptides than the commercial TiO_2 material.

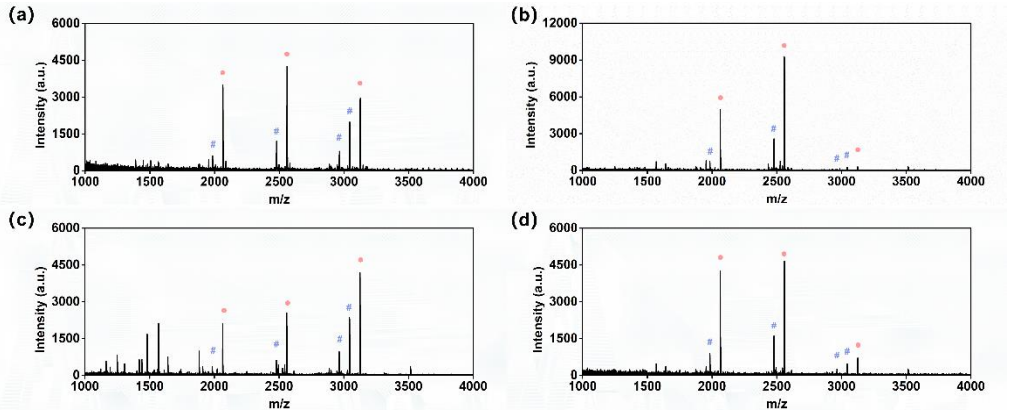

Figure 1-6. MALDI-TOF mass spectra of phosphopeptides from β-casein and BSA tryptic

digest with mass ratios of (a, b) 1/100, (c, d) 1/500 after enrichment by commercial TiO_2 material (a, c) and TiO_2-CM (b, d). Phosphopeptide peaks identified are marked with the symbol "●", dephosphorylated peptide peaks identified are marked with the symbol "#".

Because of the extremely low abundance of phosphopeptides in the biosample, it was necessary to evaluate the detection limit of the materials. Therefore, different concentrations of the β-casein (1, 5 and 10 fmol μL^{-1}) sample were chosen to investigate the detection limit of the resultant TiO_2-CM material in the enrichment process of phosphopeptides. As observed in **Figure 1-7**, three phosphopeptides were selectively captured by the resultant TiO_2-CM material when the concentration of β-casein was maintained at one fmol μL^{-1}. It was proven that the TiO_2-CM material possessed a lower detection limit and could be applied to enrich phosphopeptides with low abundance in samples. In addition, the reusability of materials is meaningful sustainable development. To evaluate its reusability, five enrichments of phosphopeptide were carried out using a piece of

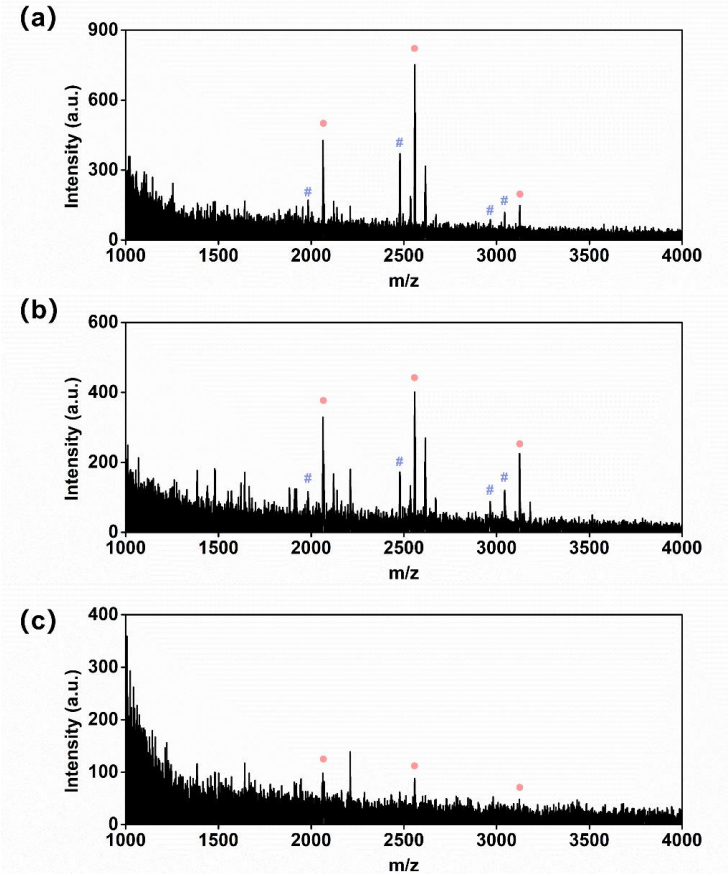

Figure 1-7. MALDI-TOF-MS spectra of (a) 50, (b) 5 and (c) 1 fmol μL^{-1} of β-casein tryptic digest after enrichment by TiO_2-CM. Phosphopeptide peaks identified are marked with the symbol "●", dephosphorylated peptide peaks identified are marked with the symbol "#".

TiO_2-CM material. As shown in **Figure 1-8**, there is no significant difference between the results of the first and fifth enrichments, which demonstrated that TiO_2-CM has reusability.

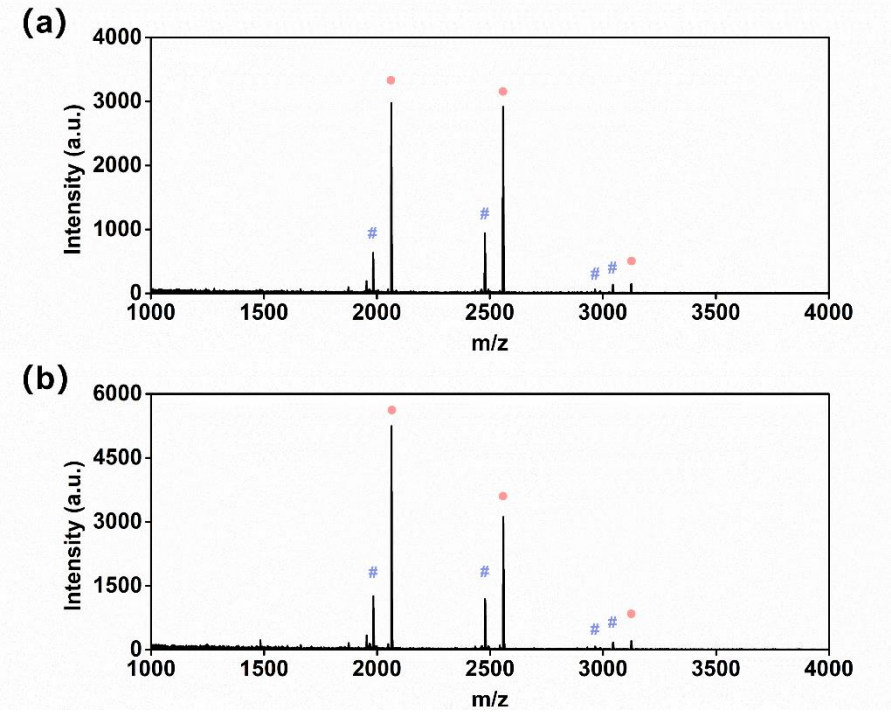

Figure 1-8. MALDI-TOF-MS spectra of β-casein tryptic digest after enrichment by TiO_2-CM for the (a) first time and (b)after recycled 5 times. Phosphopeptide peaks identified are marked with the symbol "●", dephosphorylated peptide peaks identified are marked with the symbol "#".

To illustrate the applicability of the TiO_2-CM material in the practical analyses of real biological samples, the tryptic digest of the Hela cell exosomes was chosen as the biosample and phosphopeptides enrichment was carried out using the TiO_2-CM material. After an analysis using a database search, 9287 unique phosphopeptides derived from the 2661 phosphoproteins were successfully identified from the two mg tryptic digests of the Hela cell exosomes obtained through five independent replications after enrichment by the TiO_2-CM material (as shown in **Figure 1-9a**). Furthermore, the motif composition of the identified phosphorylation sites after processing can be observed in **Figure 1-9b**. The above results sufficiently demonstrated that the resultant TiO_2-CM material exhibited large potential in the analysis of phosphorylation for complex biological samples.

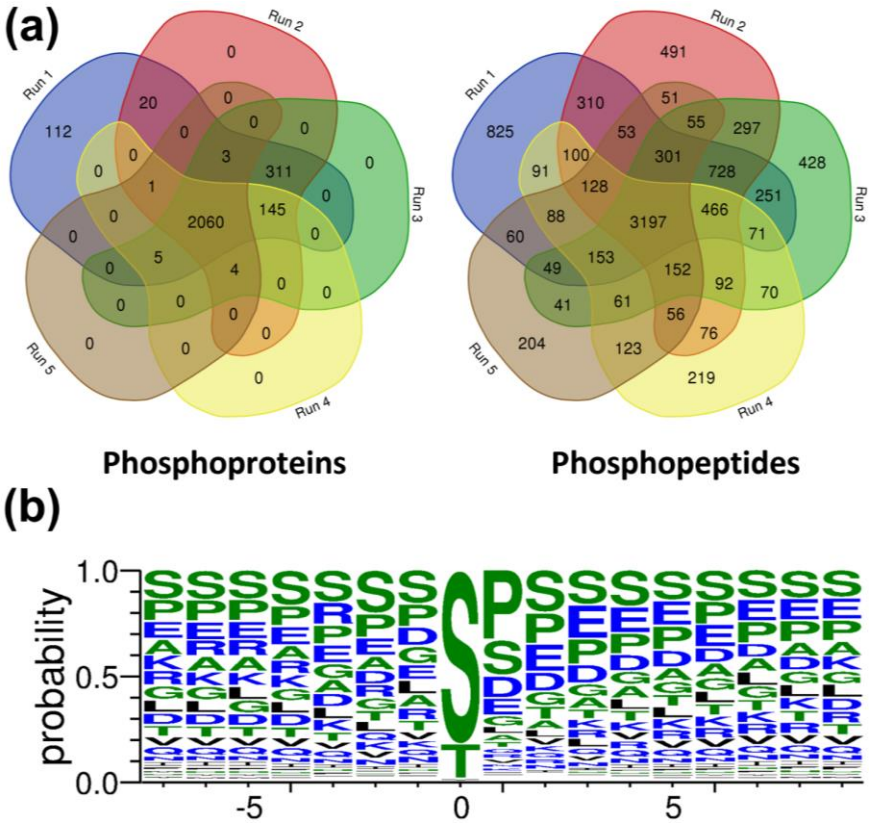

Figure 1-9. Identification results of the tryptic digest of Hela cell exosomes after enrichment with the TiO_2-CM material *via* LC-MS/MS. (a) Venn diagrams of identified unique phosphoproteins and phosphopeptides. (b) Motif analysis of the phosphopeptides.

1.4 Conclusions

Using an environmentally friendly and economic cellulose material (CM) with a coral-like structure as a supporter, a biomimetic TiO_2-CM material was prepared *via* the sol–gel method. This method allowed the combination of the organic and inorganic substances in a manner that the material mimicked the mollusk shells in terms of composition. The resultant TiO_2-CM material exhibited high mechanical strength and stable during the enrichment process, preventing the tedious procedure of multiple centrifugation cycles. The CM material provided macropores that improved the mass transfer efficiency between the material and the peptide. Moreover, a high TiO_2 content promoted a significant increase in the surface area of the corresponding TiO_2-CM material, which provided more active sites for phosphopeptide capture. As a result, the performance of the as-prepared TiO_2-CM material toward the enrichment process for phosphopeptides was higher than that of commercial TiO_2 beads, and it has reusability. In addition, the TiO_2-CM material was successfully employed in the analysis of complex biological samples, confirming its applicability in the analysis of protein phosphorylation.

1.5 References

1. A. J. Whitmarsh and R. J. Davis, *Science* 2016, **354**, 179–180.
2. P. Cohen, *Nature* 1982, **296**, 613–620.
3. P. Cohen, *Nat. Cell Biol.* 2002, **4**, E127–E130.
4. E. J. Nestler and P. Greengard, *Nature* 1983, **305**, 583–588.
5. Y. Jiang, A. Sun, Y. Zhao, W. Ying, H. Sun, X. Yang, B. Xing, W. Sun, L. Ren, B. Hu, C. Li, L. Zhang, G. Qin, M. Zhang, N. Chen, M. Zhang, Y. Huang, J. Zhou, Y. Zhao, M. Liu, X. Zhu, Y. Qiu, Y. Sun, C. Huang, M. Yan, M. Wang, W. Liu, F. Tian, H. Xu, J. Zhou, Z. Wu, T. Shi, W. Zhu, J. Qin, L. Xie, J. Fan, X. Qian, F. He and C. Chinese Human Proteome Project, *Nature* 2019, **567**, 257–261.
6. P. Blume-Jensen and T. Hunter, *Nature* 2001, **411**, 355–365.
7. A. S. Gajadhar, H. Johnson, R. J. Slebos, K. Shaddox, K. Wiles, M. K. Washington, A. J. Herline, D. A. Levine, D. C. Liebler, F. M. White and C. Clinical Proteomic Tumor Analysis, *Cancer Res.* 2015, **75**, 1495–1503.
8. G. Giamas, Y. L. Man, H. Hirner, J. Bischof, K. Kramer, K. Khan, S. S. Ahmed, J. Stebbing and U. Knippschild, *Cell Signal* 2010, **22**, 984–1002.
9. M. Labots, J. C. van der Mijn, R. Beekhof, S. R. Piersma, R. R. de Goeij-de Haas, T. V. Pham, J. C. Knol, H. Dekker, N. C. T. van Grieken, H. M. W. Verheul and C. R. Jimenez, *J. Proteomics* 2017, **162**, 99–107.
10. H. Chu, H. Zheng, N. Sun and C. Deng, *Anal. Chim. Acta* 2022, **1195**, 338693.
11. F. E. McAllister, M. Niepel, W. Haas, E. Huttlin, P. K. Sorger and S. P. Gygi, *Anal. Chem.* 2013, **85**, 4666–4674.
12. X. Li, N. Zhang, R. Tang, J. Lyu, Z. Liu, S. Ma, J. Ou and M. Ye, *Nanoscale* 2021, **13**, 2923–2930.
13. H. Zhou, M. Ye, J. Dong, E. Corradini, A. Cristobal, A. J. Heck, H. Zou and S. Mohammed, *Nat. Protoc.* 2013, **8**, 461–480.
14. J. Porath, *TrAC, Trends Anal. Chem.* 1988, **7**, 254–259.

15. Y. He, S. Zhang, C. Zhong, Y. Yang, G. Li, Y. Ji and Z. Lin, *Talanta* 2021, **235**, 122789.
16. Y. He, Q. Zheng, H. Huang, Y. Ji and Z. Lin, *Anal. Chim. Acta* 2022, **1198**, 339552.
17. J. Li, C. Fan, Y. Yao, Z. Liu, F. Li and B. Jiang, *J. Sep. Sci.* 2022, **45**, 1336–1344.
18. G. T. Cantin, T. R. Shock, S. K. Park, H. D. Madhani and J. R. Yates, *Anal. Chem.* 2007, **79**, 4666–4673.
19. A. B. Wijeratne, D. N. Wijesundera, M. Paulose, I. B. Ahiabu, W. K. Chu, O. K. Varghese and K. D. Greis, *ACS Appl. Mater. Interfaces* 2015, **7**, 11155–11164.
20. F. Yan, L. Liu, T. R. Walsh, Y. Gong, P. Z. El-Khoury, Y. Zhang, Z. Zhu, J. J. De Yoreo, M. H. Engelhard, X. Zhang and C. L. Chen, *Nat. Commun.* 2018, **9**, 2327.
21. X. T. Luo and C. J. Li, *Small* 2019, **15**, e1901919.
22. L. Zhang, S. Ma, Y. Chen, Y. Wang, J. Ou, H. Uyama and M. Ye, *Anal. Chem.* 2019, **91**, 2985–2993.
23. H. Zhao, Y. Yue, L. Guo, J. Wu, Y. Zhang, X. Li, S. Mao and X. Han, *Adv. Mater.* 2016, **28**, 5099–5105.
24. L. Zhang, Y. Wang, L. Pan, R. Tang, T.-A. Asoh, J. Ou and H. Uyama, *Green Chem.* 2021, **23**, 7674–7684.
25. Y. Xin, Q. Xiong, Q. Bai, M. Miyamoto, C. Li, Y. Shen and H. Uyama, *Carbohydr. Polym.* 2017, **157**, 429–437.
26. Y. Lyu, T.-A. Asoh and H. Uyama, *Mater. Chem. Front.* 2021, **5**, 3877–3885.
27. H. Zhou, T. Y. Low, M. L. Hennrich, H. van der Toorn, T. Schwend, H. Zou, S. Mohammed and A. J. Heck, *Mol. Cell. Proteomics* 2011, **10**, 2673–2673.
28. N. Sugiyama, T. Masuda, K. Shinoda, A. Nakamura, M. Tomita and Y. Ishihama, *Mol. Cell. Proteomics* 2007, **6**, 1103–1109.
29. M. R. Larsen, T. E. Thingholm, O. N. Jensen, P. Roepstorff and T. J. Jorgensen, *Mol. Cell. Proteomics* 2005, **4**, 873–886.
30. L. Yu, Z. Zhu, K. C. Chan, H. J. Issaq, D. S. Dimitrov and T. D. Veenstra, *J. Proteome Res.* 2007, **6**, 4150–4162.

31. A. Goswami, K. M. Alam, P. Kumar, P. Kar, T. Thundat and K. Shankar, *Carbohydr. Polym.* 2020, **246**, 116393.
32. U. Cernigoj, J. Gaspersic, A. Fichtenbaum, N. Lendero Krajnc, J. Vidic, G. Mitulovic and A. Strancar, *Anal. Chim. Acta* 2016, **942**, 146–154.
33. C. Lei, L. Zhou, C. Xu, X. Sun, A. Nouwens and C. Yu, *Aust. J. Chem.* 2016, **69**, 1396–1401.
34. K. Salimi, C. Kip, O. Celikbicak, D. D. Usta, A. Pinar, B. Salih and A. Tuncel, *Biomed Chromatogr* 2019, **33**, e4488.
35. K. Salimi, D. D. Usta, O. Celikbicak, A. Pinar, B. Salih and A. Tuncel, *Colloids Surf B Biointerfaces* 2017, **153**, 280–290.
36. H. Wang, J. Duan, H. Yu, L. Zhao, Y. Liang, Y. Shan, L. Zhang, Z. Liang and Y. Zhang, *J. Sep. Sci.* 2011, **34**, 2113–2121.

Chapter 2.

Fabrication of Reusable Bifunctional Biomimetic Ti^{4+}-Phosphorylated Cellulose Monolith with Coral-Like Structure for Enrichment of Phosphorylated and Glycosylated Peptides

2.1 Introduction

The post-translational modifications (PTMs) of proteins refer to processes such as the chemical modification and side-chain processing of protein precursors, which endow various life functions to proteins. Among more than 300 known PTMs, protein phosphorylation and glycosylation are considered to be the two most important and widely studied. Almost all cellular activities are regulated by phosphorylation.[1-4] Abnormal protein phosphorylation has been found to be closely related to more than 400 diseases, including cancer and diabetes.[5-9] Studying protein phosphorylation can provide important information for identifying cancer markers, discovering drug targets, *etc*. Similarly, more than 50% of human proteins can be modified through glycosylation, the polysaccharide chains attached to glycosylated proteins being involved in a variety of important life processes.[10, 11] Generally, aberrant protein glycosylation is closely associated with many cancers, neurological diseases, and Alzheimer's.[12-15] Moreover, studies on the novel coronavirus disease (COVID-2019) has shown that glycosylated proteins on the surface of coronaviruses play a crucial role. When they invade cells, these glycosylated proteins also being major targets of antibodies.[16, 17] Thus far, most of the identified disease markers are glycosylated proteins.[18, 19] Consequently, the study of protein phosphorylation and glycosylation is of great importance.

A current analytical method commonly used to explore protein phosphorylation and glycosylation is to digest proteins into peptides and then to analyze them using mass spectrometry (MS). However, due to the low abundance of phosphorylated and glycosylated peptides in protein digestion, a large number of non-phosphopeptide and non-glycopeptide

signals interfere with the phosphopeptide and glycopeptide signals, making it difficult to analyze protein digestion samples directly using MS. Consequently, the development of enrichment methods with specificity is of great importance for the analysis of protein phosphorylation and glycosylation. Currently, phosphopeptide enrichment methods include metal oxide affinity chromatography (MOAC), immobilized metal affinity chromatography (IMAC), immunoaffinity chromatography (IAC) and so on.[20-23] Among these methods, IMAC is the most widely used in phosphopeptide enrichment due to its high specificity and low steric effects, which are achieved by the chelation and static adsorption between phosphate groups in phosphopeptides and metal ions.[24] Moreover, some strategies—including lectin affinity chromatography, hydrazine chemistry, boric acid chemistry, and hydrophilic interaction chromatography (HILIC)—have been commonly applied to glycopeptide enrichment.[25, 26] Of these strategies, HILIC exhibits many advantages, such as its ability to enrich various glycosylated peptides, retaining intact oligosaccharide chain information. Compared to non-glycopeptides, glycopeptides with saccharide chains exhibit stronger hydrophilicity which can be selectively enriched by hydrophilic materials. The materials that have been used in glycopeptide enrichment have been widely reported.[27] However, there are disadvantages, namely their complicated and environmentally unfriendly preparation processes and high cost. Most importantly, there are few reports of materials that can simultaneously enrich both phosphopeptides and glycopeptides, although various materials used in phosphopeptide and glycopeptide enrichment processes have been extensively reported.

Conversely, some corals—as one of the oldest marine organisms on Earth—have evolved a unique dendritic structure which allows them to efficiently capture food from flowing seawater. Their predatory behavior is very similar to that of IMAC and HILIC materials in capturing phosphopeptides and glycopeptides from a loading solution. Consequently, the dendritic coral-like structure can increase permeability to improve the mass transfer rate between the material and the enrichment solution, reducing the steric effect between the peptides and the material during enrichment. Moreover, the microstructure that exists in dendritic surfaces is beneficial in providing more sites for the material to adsorb

phosphopeptides and glycopeptides.

Inspired by coral, we fabricated a Ti^{4+}-phosphorylated cellulose monolith (TiPCM) with a coral-like structure for the enrichment of phosphorylated and glycosylated peptides in this study. Cellulose is considered to be the most promising, sustainable, and renewable carbon source as it is one of the most widely distributed and abundant polysaccharides in nature.[28] It has the advantages of being environmentally friendly, non-toxic, inexpensive, and widely available. In recent years, our group fabricated a cellulose monolith (CM) with a coral-like structure by changing its preparation conditions.[29-32] We prepared phosphorylated CM *via* an esterification reaction, after which the titanium ion (Ti^{4+}) was modified on the surface of its skeleton *via* chelation between the Ti^{4+} and the phosphate group. A large number of phosphate groups on the surface of the TiPCM clearly advanced the hydrophilicity of the CM, offering many sites to chelate Ti^{4+}. Most importantly, the entire process is green, placid, and simple, the resulting TiPCM exhibiting satisfactory performance in the analysis of protein phosphorylation and glycosylation.

2.2 Experimental Section

2.2.1 Chemicals and materials

Cellulose acetate (CA, L30) with an acetylation degree of 55% was provided by Daicel Co., Ltd. Japan. Sodium dihydrogen phosphate (NaH_2PO_4), sodium hydrogen phosphate (Na_2HPO_4), sodium hydroxide, urea, ammonium bicarbonate, ammonia water, and acetonitrile (ACN) were purchased from FUJIFILM Wako Pure Chemical Corporation, Japan. Dithiothreitol (DTT), Iodoacetamide (IAA), β-casein, immunoglobulin G (IgG), bovine albumin (BSA), trypsin, and trifluoroacetic acid (TFA) were purchased from Sigma Co., Ltd. USA. Titanium (IV) sulfate solution was purchased from Kishida Chemical Co., Ltd. Japan. Deionized water was doubly distilled and purified using the Milli-Q system (Millipore Inc., Milford, MA, USA).

2.2.2 Preparation of the cellulose monolith (CM)

The preparation process of the CM was described in our previous report.[31] In brief, a certain amount of CA was dissolved in dimethylformamide (DMF) at 90 ^{o}C. Then, 1-hexanol was added dropwise into the solution whilst it was stirred. The solution was placed into a water bath at 20 ^{o}C for 24 h to achieve phase separation after it had become transparent. Subsequently, the product was washed three times using ethanol before being dried under vacuum to obtain the CA monolith. The resulting CA monolith was hydrolyzed using 0.5 mol L^{-1} NaOH aqueous solution, and then washed with deionized water and dried under vacuum to obtain the CM.

2.2.3 Preparation of the Ti^{4+}-phosphorylated CM (TiPCM)

As shown in **Scheme 2-1a**, the 40 mL aqueous solution containing urea (18.7 g), Na_2HPO_3 (11.1 g), and NaH_2PO_3 (24.9 g) was circulated through the prepared CM for 1 h using a pump. The CM filled with the aqueous solution was heated in an oven at 140 ^{o}C overnight, and then washed with water and dried to obtain the phosphorylated cellulose monolithic (PCM) material. Subsequently, the titanium phosphate solution was passed through the PCM for 4 h using a

pump to achieve the incorporation of Ti^{4+} and the PCM. The product was washed using deionized water, and then dried under vacuum to acquire the TiPCM.

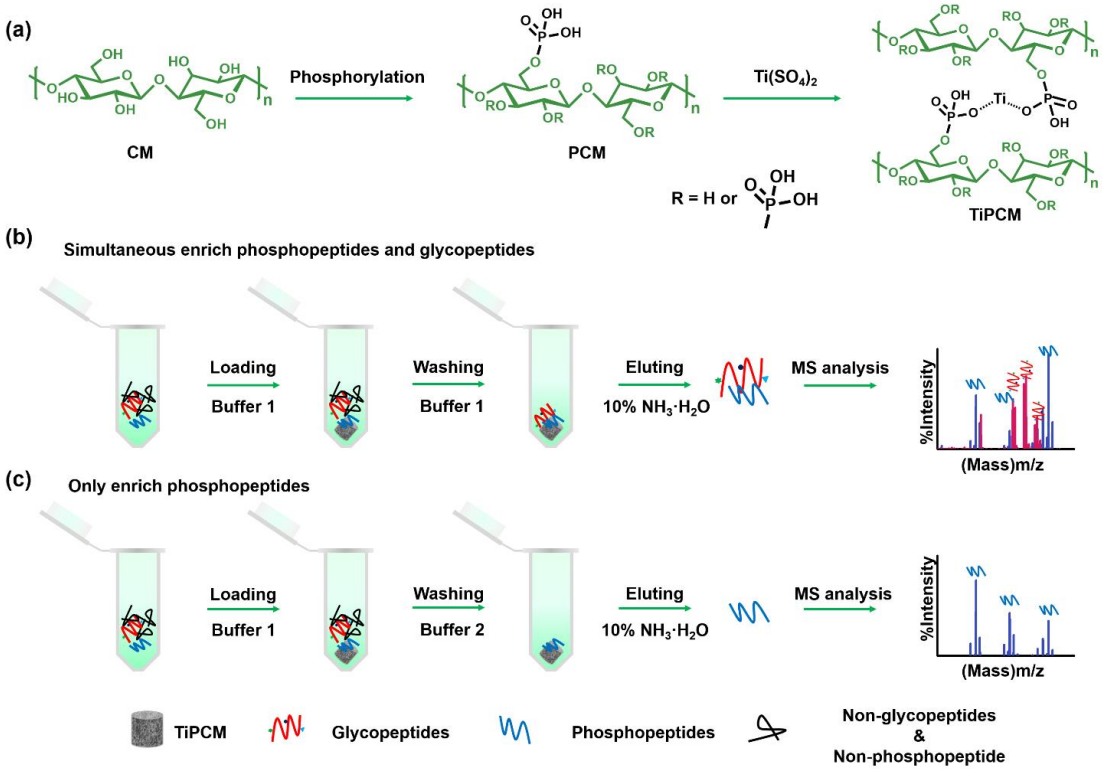

Scheme 2-1. (a) Preparation of the TiPCM. (b) Workflow of the simultaneous enrichment of phosphopeptides and glycopeptides. (c) Workflow of the individual enrichment of phosphopeptides. Buffer 1: 79% ACN + 3% TFA + 18% H_2O, Buffer 2: 50% ACN + 3% TFA + 47% H_2O.

2.2.4 Instruments and methods

Attenuated total reflection Fourier transform infrared (ATR-FTIR) spectroscopy (Thermo Scientific Nicolet iS 5) was used to confirm the synthesis of the CM and PCM. The pore structure and morphology of the materials were examined by means of scanning electron microscopy (SEM, Hitachi S-3000N, Tokyo, Japan). The thermal stability of the materials was confirmed through thermogravimetric analysis (TGA, Hitachi TG/DTA7200, Tokyo, Japan). The hydrophilicity of the materials was evaluated by means of the water contact angle obtained using a Drop Master DM300 (Kyowa Interface Science, Japan) with 1.0 μL water drops. The Brunauer-Emmett-Teller (BET) surface area of the materials was evaluated by using a nitrogen adsorption–desorption analyzer (Quantachrome Instruments, USA). X-ray photoelectron

spectroscopy (XPS, JEOL JPS-9010MC) was employed to investigate the surface chemistry of the materials, using monochromatized Al-Kα radiation (1486.6 eV). The XPS spectra were determined at fixed analyzer pass energies of 160 eV and 10 eV, respectively. The binding energies were referred to as C-H (sp^3) carbon for the C 1s peak set at 284.8 eV.

2.2.5 Denaturation and enzymatic digestion of protein solutions

One militer of denaturing solution containing 8.0 mol · L^{-1} urea and 0.1 mol · L^{-1} ammonium bicarbonate was used to dissolve 2 mg BSA/IgG/β-casein/milk specimens, followed by the addition of 20 mmol · L^{-1} DTT solution. The mixture was incubated at 60 °C for 1 h, after which it was incubated further for 30 min in the dark at room temperature after IAA (7.4 mg) was added. The ammonium bicarbonate solution (0.1 mol · L^{-1}) was used to dilute the mixture 8 times, and 80 μg of trypsin was added for the BSA/IgG/β-casein/milk specimens to incubate at 37 °C for 16 h. Subsequently, a 10% TFA aqueous solution was adapted to adjust the pH of the mixture to approximately 2–3. A custom C18 column was selected to perform solid phase extraction (SPE). The eluted peptide solution was dried under vacuum and dissolved in a 0.1% FA (2.0 mL) aqueous solution. Eventually, the resulting peptide solution was dispensed and dried using a freeze dryer, followed by storage at −20 ºC.

2.2.6 Enrichment of phosphopeptides and glycopeptides

The process of enrichment of phosphopeptides and glycopeptides usually includes loading, washing and elution, as shown in **Scheme 2-1**. For simultaneous enrichment of phosphopeptides and glycopeptides, as shown in **Scheme 2-1b**. The loading solution (100 μL × 3, Buffer 1, ACN/H_2O/TFA = 79/18/3, v/v/v) was used in washing a certain amount of the TiPCM 3 times, and then the loading solution (100 μL, Buffer 1, ACN/H_2O/TFA = 79/18/3, v/v/v) with a certain amount of BSA/IgG/β-casein tryptic digest was added. A bio shaker was employed to incubate the mixture at 25 °C for 0.5 h. Subsequently, the mixture was centrifugated at 5,000 g for 2 min to remove solution, and washing solution (100 μL × 3, Buffer 1, ACN/H_2O/TFA = 79/18/3, v/v/v) was used in washing the residual substance for 15 min 3 times. The elution solution (50 μL × 2, 10% $NH_3 \cdot H_2O$) was adopted in eluting the captured

glycopeptides for 10 min at 25 °C twice. Finally, MALDI-TOF was employed to analyze the eluted solution.

Conversely, **Scheme 2-1c** shows the process of enriching only phosphopeptieds. A certain amount of the TiPCM was washed with loading solution (100 μL × 3, Buffer 1, ACN/H_2O/TFA = 79/18/3, v/v/v) 3 times. Then, loading solution (100 μL, Buffer 1, ACN/H_2O/TFA = 79/18/3, v/v/v) with a certain amount of BSA/IgG/β-casein tryptic digest was added to load sample. enriching process of only enriching phosphopeptieds is similar with simultaneous enrichment of phosphopeptides and glycopeptides except for wasing solution. For only enriching phosphopeptieds, Buffer 2 (ACN/H_2O/TFA = 50/47/3, v/v/v) was chosen as washing solution.

To enrich the phosphopeptides and glycopeptides from complex sample, a certain amount of the TiPCM was washed with loading solution (100 μL × 3, Buffer 1, ACN/H_2O/TFA = 79/18/3, v/v/v), and then 200 μg tryptic digest of milk dissoved in 500 μL Buffer 1 was added to load sample. A bio shaker was employed to incubate the mixture at 25 °C for 0.5 h. Subeseuqently, the mixture was centrifugated at 5,000 g for 2 min to remove solution, and washing solution (500 μL × 3, Buffer 1, ACN/H2O/TFA = 79/18/3, v/v/v) was used in washing the TiPCM for 15 min 3 times. The elution solution (50 μL × 2, 10% $NH_3 \cdot H_2O$) was adopted in eluting the captured phosphopeptides and glycopeptides for 10 min at 25 °C twice. Finally, the glycopeptide solutions from the two elution solutions were mixed, lyophilized, deglycosylated, and analyzed by liquid-chromatography–mass-spectrometry (LC-MS). The LC-MS experiments are detailed in the Supporting Information section.

2.3 Results and discussion

2.3.1 Preparation of the TiPCM

Corals, as one of the oldest marine organisms on Earth, possess unique dendritic structures which allow them to efficiently use flowing seawater to capture food. Inspired by their unique structure, a monolithic material (TiPCM) with a coral-like structure was fabricated to apply in the field of phosphopeptide and glycopeptide enrichment in this work. The unique coral-like structure in the TiPCM facilitates the reduction of steric effects between the peptide and the material during enrichment and provides more sites to adsorb peptides. As previously reported, our group discovered that the skeleton of the CM could be changed by adjusting the CA concentration.[31] As shown in **Figure 2-1**, when the CA concentrations were 80 and 100 mg · mL^{-1}, respectively, the prepared CM-1 and CM-2 specimens exhibited a dendritic coral-like structure on which many villi exist. As the CA concentrations increased to 120 mg · mL^{-1}, the CM-3 skeleton changed to a network structure as shown in **Figures 2-1c** and **2-1f**. It can be seen from **Table 2-1**, that the CM-1 exhibited excellent permeability (3.07×10^{-12} m^2) when the CA concentration was 80 mg · mL^{-1}. Consequently, the CM-1 was chosen for the preparation of the TiPCM in the subsequent experiments.

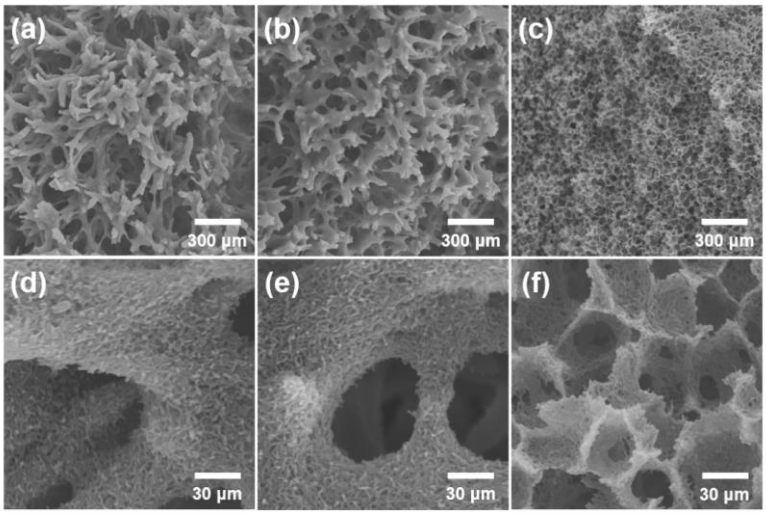

Figure 2-1. SEM images of (a, d) CM-1, (b, e) CM-2 and (c, f) CM-3 (at 500 ×, 5000 ×, 500 ×, 5000 ×, 500 × and 5000 × magnification, respectively).

Table 2-1. Detailed composition for fabrication of the CM.

Monolith	DMF (mL)	1-Hexanol (mL)	CA concentration ($mg \cdot mL^{-1}$)	Permeability ($\times 10^{-12}$ m^2)
CM-1	10	15	80	3.07
CM-2	10	15	100	0.12
CM-3	10	15	120	0.01

2.3.2 Physical properties of the TiPCM

To explore whether the skeleton of the material could successfully mimic the structure of coral, SEM was used to observe the microscopic morphology of the CM, PCM and TiPCM. As shown in **Figures 2-2a**[33]**, b, e,** and **f**, the prepared CM material had the dendritic skeleton structure of coral. After magnified observation, the surface of the dendritic structure could be seen to have a fluff-like structure similar to the surface of the dendritic structure in coral. After phosphorylation and chelation, both the PCM and TiPCM maintained the coral-like skeleton structure of the CM. The coral-like structure still had a rough surface, but the fluff-like structure on the surface of the coral-like structure had been destroyed, which may have been due to the destruction of cellulose crystals by urea during the phosphorylation process (**Figures 2-2c, d, g,** and **h**).

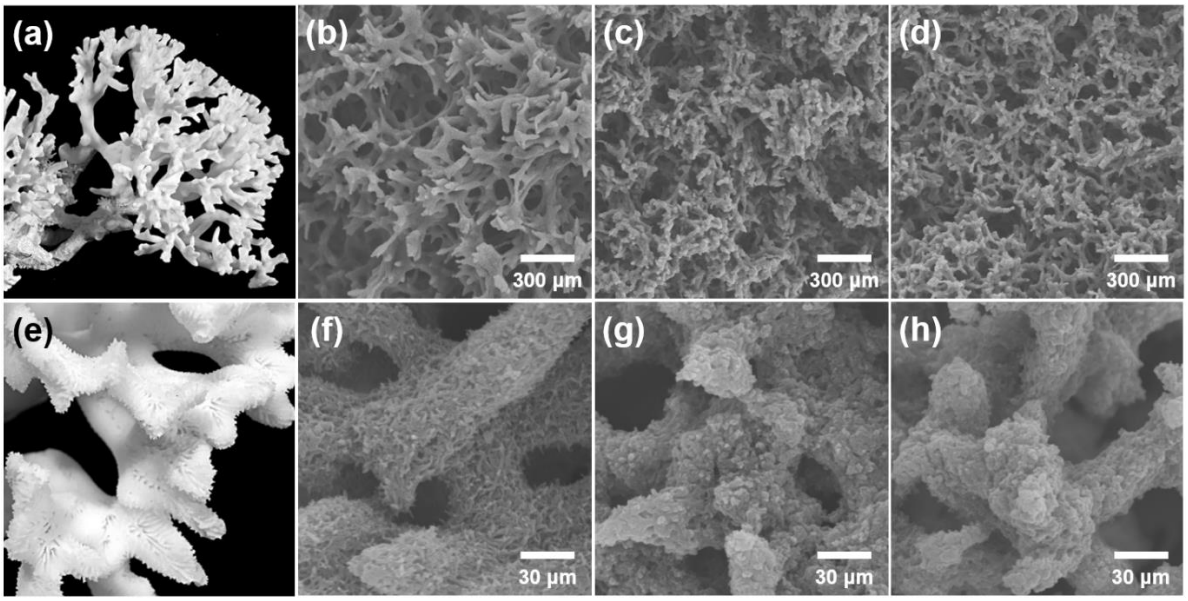

Figure 2-2 (a, e) Photograph of Paraclavarina, a type of coral that lives in Australia.33 SEM images of (b, f) the CM, (c, g) PCM, and (d, h) TiPCM (at 500×, 5000×, 500×, 5000×, 500×, and 5000× magnification, respectively).

Furthermore, the CM, PCM and TiPCM materials were characterized by ATR-FTIR to verify if the phosphorylation of cellulose had been successful. As seen in **Figure 2-3a**, when compared with the spectrum of the CM, the signals appeared at 1,232 (P=O), 924 (P-OH), and 827 cm^{-1} (P-O-P) which were assigned to be the characteristic peaks of the phosphate group in the PCM and TiPCM. This result demonstrated that the CM had been successfully phosphorylated into the PCM, and that the phosphate group still existed in the TiPCM.

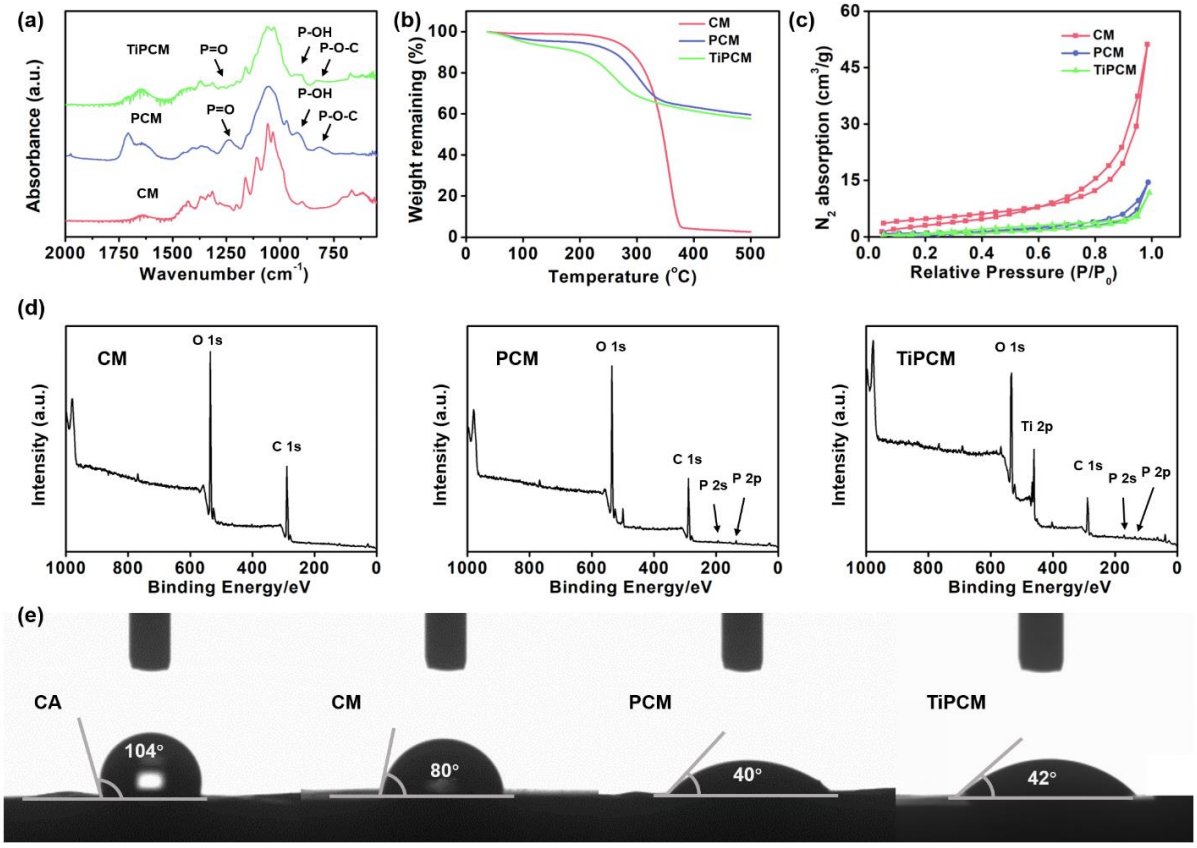

Figure 2-3. (a) ATR-FTIR spectra, (b) thermogravimetric curve at a heating rate of 10 °C · min−1 within a nitrogen atmosphere, (c) nitrogen adsorption-desorption isotherms, (d) XPS spectra of the CM, PCM and TiPCM and (e) the water contact angle of CA, CM, PCM, and TiPCM.

The thermal stability of the materials was evaluated by TGA. As shown in **Figure 2-3b**, the CM, PCM, and TiPCM exhibited good stability before 200 °C. Among the three materials,

the CM showed the best thermal stability because there was no obvious weight loss until 250 °C. By contrast, obvious weight loss of the PCM and TiPCM were found in the range of 200–300 ^{o}C (**Figure 2-3b**). It is worth mentioning that the remaining weight of the CM approached zero above 400 ^{o}C, while the weight of the PCM and TiPCM were 59.6% and 57.7%, respectively. Because high temperature will lead to hydrolysis of ester groups and release the phosphoric acid on the surface of cellulose. The phosphoric acid as a catalyst for the dehydration of cellulose chains, charring the surface and leading to the formation of a thermally resistant coating capable of protecting the remaining internal material at over 400 ^{o}C.[34] The above results showed that phosphate groups had been successfully introduced to the CM. Moreover, the specific surface area of these materials was examined by measuring the nitrogen adsorption/desorption isotherm. As shown in **Figure 2-3c,** the BET specific surface area of the CM was 16.7 $m^2 \cdot g^{-1}$. However, after phosphorylation, the specific surface area of the PCM and TiPCM decreased to 3.3 and 2.9 $m^2 \cdot g^{-1}$, respectively. This phenomenon was possibly caused by the destruction of cellulose crystals, the addition of urea leading to the collapse of mesopores in the CM which was consistent with the SEM images (**Figure 2-2**). The XPS spectra was utilized to confirm the introduction of Ti^{4+} onto the surface of the PCM. It could be seen from the spectrum of the CM (**Figure 2-3d**) that the signals at 535.11 and 288.88 eV, respectively, corresponded to O 1s and C 1s. As for the PCM, the peaks of P 2s and P 2p also appeared at 193.96 and 136.07 eV (**Figure 2-3d**) except for the peaks of O 1s at 535.04 eV and C 1s at 288.95 eV, demonstrating that the phosphate groups had been modified on the surface of the PCM. Furthermore, the peaks of Ti 2p could be seen at 461.01 eV (**Figure 2-3d**), proving that the Ti^{4+} successfully chelated with the phosphate groups in the TiPCM. In addition, the hydrophilicity of the material showed a strong influence on the enrichment of the glycosylated peptides. The water contact angle technique was employed to examine the hydrophilicity of the materials. To avoid the effects of surface roughness and porous structure, the CA monolith, CM, PCM, and TiPCM were compressed to smooth sheets to determine their hydrophilicity. As shown in **Figure 2-3e**, the water contact angle of the CA monolith was 104°, indicating that it was a hydrophobic material because of the presence of many ester groups on its surface.

Compared with the CA monolith, the water contact angle of the CM decreased to 80°, exhibiting hydrophilicity as the ester groups had been hydrolyzed by NaOH to hydroxyl groups. After the CM was phosphorylated, the hydrophilicity of the PCM and TiPCM was significantly strengthened, and their water contact angles diminished to 40° and 42°, respectively. The phenomenon demonstrated that a large number of hydrophilic phosphate groups had been introduced onto the surface of the CM, and phosphorylation had succeeded. As a result, the TiPCM exhibited good hydrophilicity and has the potential to enrich glycopeptides.

2.3.3 Enrichment of phosphopeptides and glycopeptides

The content of the organic phase in the loading buffer is an important factor for the enrichment of peptides.[35] As for phosphopeptides and glycopeptides, their retention behavior on the surface of the materials was significantly influenced by the content of the organic solvent. To enrich glycopeptides and phosphopeptides simultaneously, the effect of different ACN concentrations in the loading buffer was examined, as shown in **Figure 2-4**. When ACN/H_2O/TFA (83/14/3, v/v/v) was used as the loading solution, a high non-phosphopeptide signal intensity was observed in **Figure 2-4a**, and strong non-glycopeptide signals could be observed in **Figure 2-4e**. As the ACN content decreased to 81%, the non-phosphopeptide signal intensity decreased (**Figure 2-4b**) but was not weak, and the number of non-glycopeptides was reduced (**Figure 2-4f**). When ACN/H_2O/TFA (79/18/3, v/v/v) was selected as the loading solution, the number of non-phosphopeptides diminished, and the phosphopeptide signals could be clearly seen, as shown in **Figure 2-4c**. Moreover, the glycopeptide signals were prominent (**Figure 2-4g)**. However, when the organic phase further decreased to ACN/H_2O/TFA (77/20/3, v/v/v), the enrichment performance for phosphopeptides (**Figure 2-4d**) was not perceptibly different from the ACN/H_2O/TFA (79/18/3, v/v/v) case (**Figure 2-4c**). With regard to the glycopeptide enrichment results, the non-glycopeptide signals virtually completely disappeared, the glycopeptides becoming weak at the same time as observed in **Figure 2-4h**. Consequently, ACN/H_2O/TFA (79/18/3, v/v/v) was chosen to be the loading solution in the subsequent experiments.

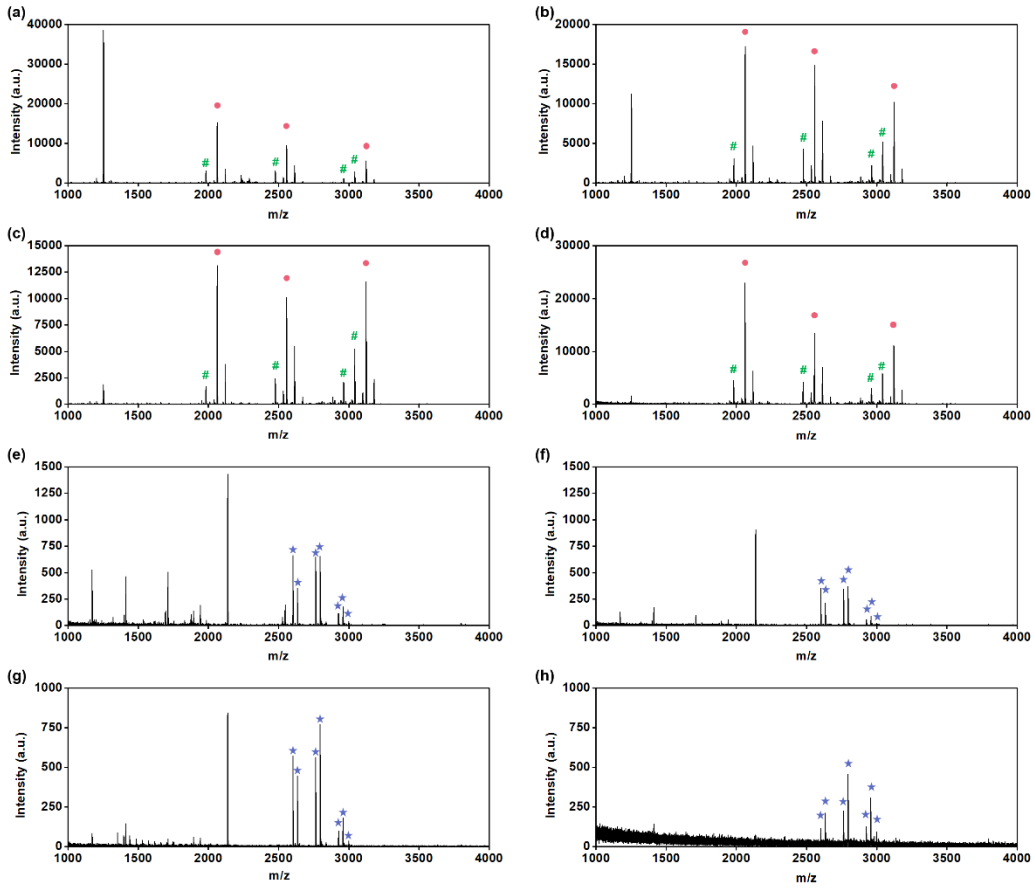

Figure 2-4. MALDI-TOF mass spectra of phosphopeptides from β-casein digest after enrichment by TiPCM with different ACN content. (a) 83% ACN + 3% TFA, (b) 81% ACN + 3% TFA, (c) 79% ACN + 3% TFA and (d) 77% ACN + 3% TFA. And MALDI-TOF mass spectra of glycopeptides from IgG digest after enrichment by TiPCM with different ACN content. (e) 83% ACN + 3% TFA, (f) 81% ACN + 3% TFA, (g) 79% ACN + 3% TFA and (h) 77% ACN + 3% TFA. Phosphopeptide peaks identified are marked with the symbol ●, dephosphorylated peptide peaks identified are marked with the symbol #, and glycopeptide peaks identified are marked with the symbol ★.

The TFA content in the enrichment solution system also effects the retention behavior of glycopeptides and phosphopeptides. To further optimize the enrichment conditions of the two kinds of peptides, different TFA content (1%, 3%, and 5%, v/v) in the loading and washing solutions was used to examine the enrichment ability of the TiPCM. As shown in **Figures 2-5a–c**, there was no obvious difference between the three concentrations when they were used to enrich phosphopeptide. However, different results appeared for the enrichment of

glycopeptide. When ACN/H_2O/TFA (79/20/1, v/v/v) was chosen to be the loading and washing solution, the glycopeptide signal was too weak, indicating that it is not suitable to use in enrichment (**Figure 2-5d**). When ACN/H_2O/TFA (79/18/3, v/v/v) and ACN/H_2O/TFA (79/16/5, v/v/v), respectively, were used to enrich glycopeptide, the number of non-glycopeptides decreased, and the glycopeptide signals grew stronger, as shown in **Figures 2-5e** and **f**. Because there was no significant difference in the enrichment performance at the two conditions, the phosphopeptides should be eluted in a basic solution. Consequently, ACN/H_2O/TFA (79/18/3, v/v/v) was used to load and wash the phosphopeptides and glycopeptides, and 10% ammonia was used for elution, as shown in **Scheme 2-1b**.

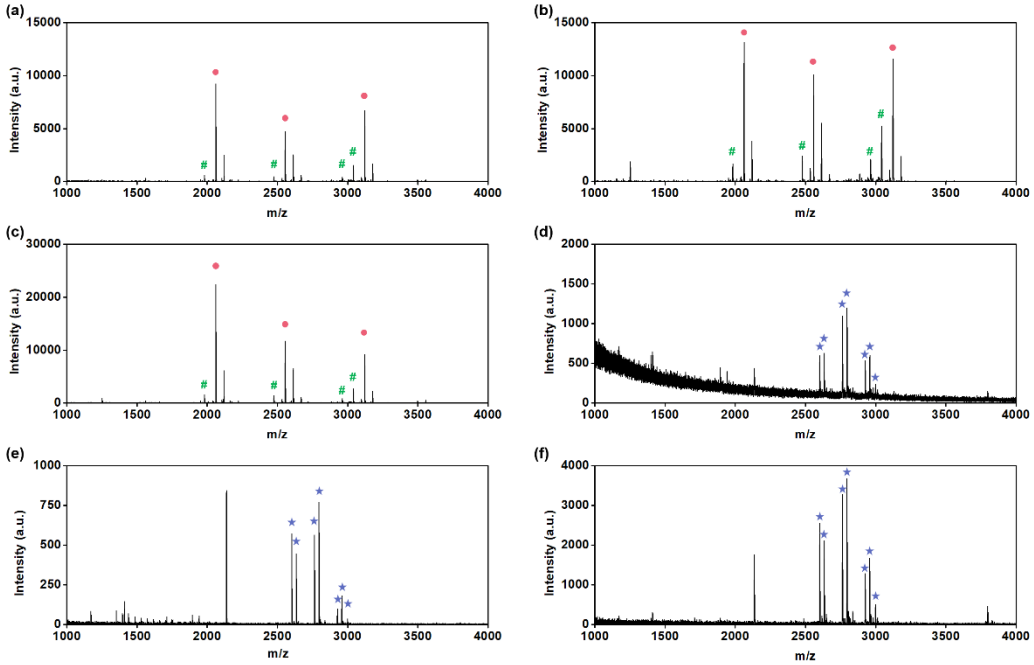

Figure 2-5. MALDI-TOF mass spectra of phosphopeptides from β-casein digest after enrichment by TiPCM with different TFA content. (a) 79% ACN + 1% TFA, (b) 79% ACN + 3% TFA and (c) 79% ACN + 5% TFA. And MALDI-TOF mass spectra of glycopeptides from IgG digest after enrichment by TiPCM with different TFA content. (d) 79% ACN + 1% TFA, (e) 79% ACN + 3% TFA and (f) 79% ACN + 5% TFA. Phosphopeptide peaks identified are marked with the symbol ●, dephosphorylated peptide peaks identified are marked with the symbol #, and glycopeptide peaks identified are marked with the symbol ★.

As shown in **Figure 2-6a**, the glycopeptide signals were restrained due to the abundant non-glycopeptide signals. Consequently, only some glycopeptides could be detected when the unenriched and purified trypsin digests of IgG were directly analyzed using the MALDI-TOF system. After enrichment using the TiPCM, 33 glycopeptides could be detected, and the non-glycopeptide interference was almost completely eliminated, as can be seen in **Figure 2-6b**. Similarly, as shown in **Figure 2-6c,** the phosphopeptides could be hardly detected when the unenriched and purified trypsin digests of β-casein was analysed because of the existence of non-phosphopeptide. However, all 3 phosphopeptides could be clearly detected after the trypsin digests of β-casein were enriched using the TiPCM. Meanwhile, 4 dephosphorylated peptides corresponding with the 3 phosphopeptides (**Figure 2-6d**) could also be detected, and the non-phosphopeptide interference was almost completely eliminated. To evaluate the ability to simultaneously enrich both glycopeptides and phosphopeptides, a mixture of trypsin digests of IgG and β-casein (molar ratio, 10/1) was chosen for analysis. As shown in **Figure 2-6e**, 30 glycopeptides, 3 phosphopeptides, and the corresponding 4 dephosphorylated peptides were detected, and the non-glycopeptide and non-phosphopeptide interferences were virtually eliminated. These results showed that the TiPCM possessed great potential for the simultaneous enrichment of both glycopeptides and phosphopeptides. Moreover, to use the TiPCM material to enrich target peptides (phosphopeptides), we investigated the individual enrichment ability for phosphopeptides from a mixture of trypsin digests of IgG and β-casein (molar ratio, 10/1) based on the process shown in **Scheme 2-1c**. As shown in the MALDI-TOF spectrum (**Figure 2-6f**), the signals of 3 phosphopeptides and the corresponding 4 dephosphorylated peptides appeared, the signals of several glycopeptides becoming very weak. Meanwhile, non-glycopeptide and non-phosphopeptid interferences were almost completely eliminated. These results showed that the TiPCM could be used to simultaneously enrich glycopeptides and phosphopeptides, as well as individually enrich

phosphopeptides. The resulting materials exhibited high selectivity and flexible application potential in the enrichment of phosphopeptides and glycopeptides.

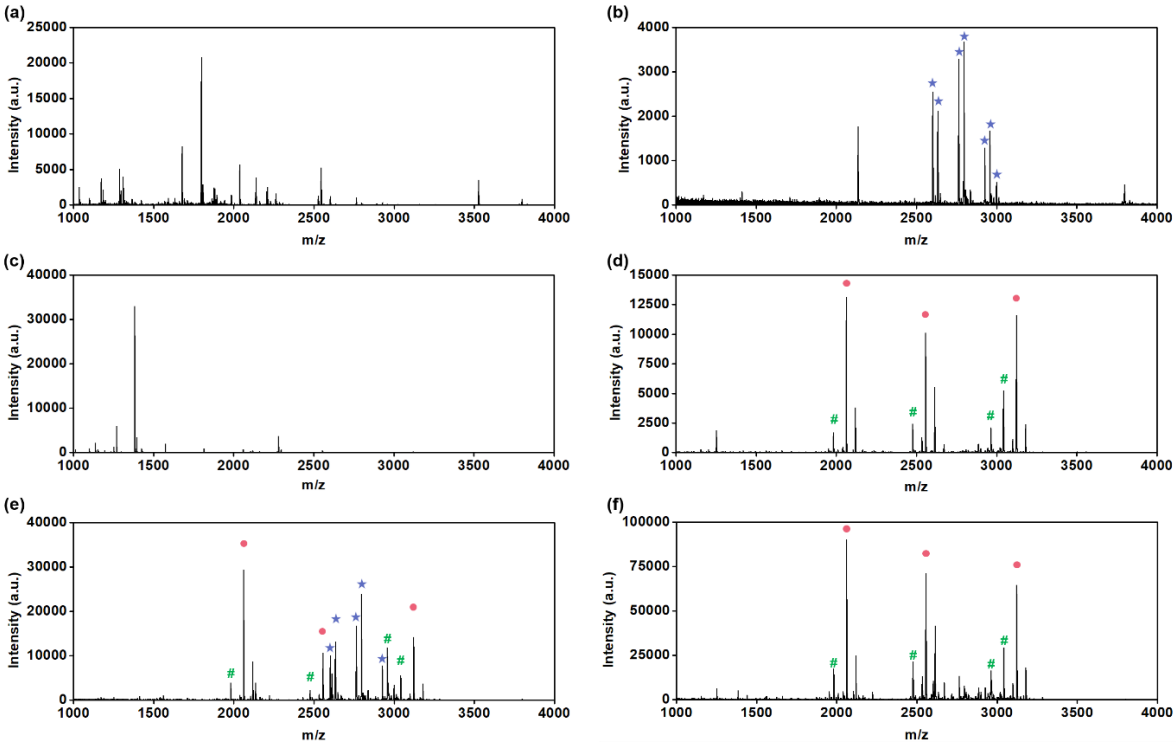

Figure 2-6. MALDI-TOF mass spectra of the tryptic digest of IgG. (a) Direct analysis and (b) analysis after enrichment by the TiPCM. MALDI-TOF mass spectra of the tryptic digest of β-casein. (c) Direct analysis and (d) analysis after enrichment by the TiPCM. MALDI-TOF mass spectra of the tryptic digest of IgG/β-casein mixture. (e) Simultaneous enrichment of phosphopeptides and glycopeptides and (f) enrichment of only phosphopeptides. Phosphopeptide peaks identified are marked with the symbol ●, dephosphorylated peptide peaks identified are marked with the symbol #, and glycopeptide peaks identified are marked with the symbol ★.

To further evaluate the enrichment selectivity of the TiPCM, the phosphopeptides and glycopeptides were enriched from composite samples that the trypsin digests of BSA was combined with the trypsin digests of β-casein or IgG in different molar ratios, as shown in **Figures 2-7a-c**. When the TiPCM was used to enrich phosphopeptides from a 1/500 molar ratio of the tryptic digests of β-casein and BSA, the 3 phosphopeptides and their corresponding 4 dephosphorylated peptides were detected, and the non-phosphopeptide interferences were

almost completely eliminated, as seen in **Figure 2-7a**. When the molar ratio of the β-casein to BSA trypsin digest was set to be 1/1000, the 3 phosphopeptides and their corresponding 4 dephosphorylated peptides could still be detected after enrichment by the TiPCM, the non-phosphopeptide signals could hardly be detected (**Figure 2-7b**). Most importantly, when the molar ratio was increased to 1/5000 (mass ratio of approximately 1/13000), all 3 phosphopeptides and their corresponding 4 dephosphorylated peptides were clearly detected despite the presence of a few non-phosphopeptide signals, as shown in **Figure 2-7c**. Moreover, the selectivity of the TiPCM for glycopeptide was also explored. It can be seen in **Figures 2-7d–f**, that 26, 20, and 17 glycopeptides could be detected from the mixture of the tryptic digests of IgG and BSA at different molar ratios of 1/100, 1/500, and 1/1000, respectively.

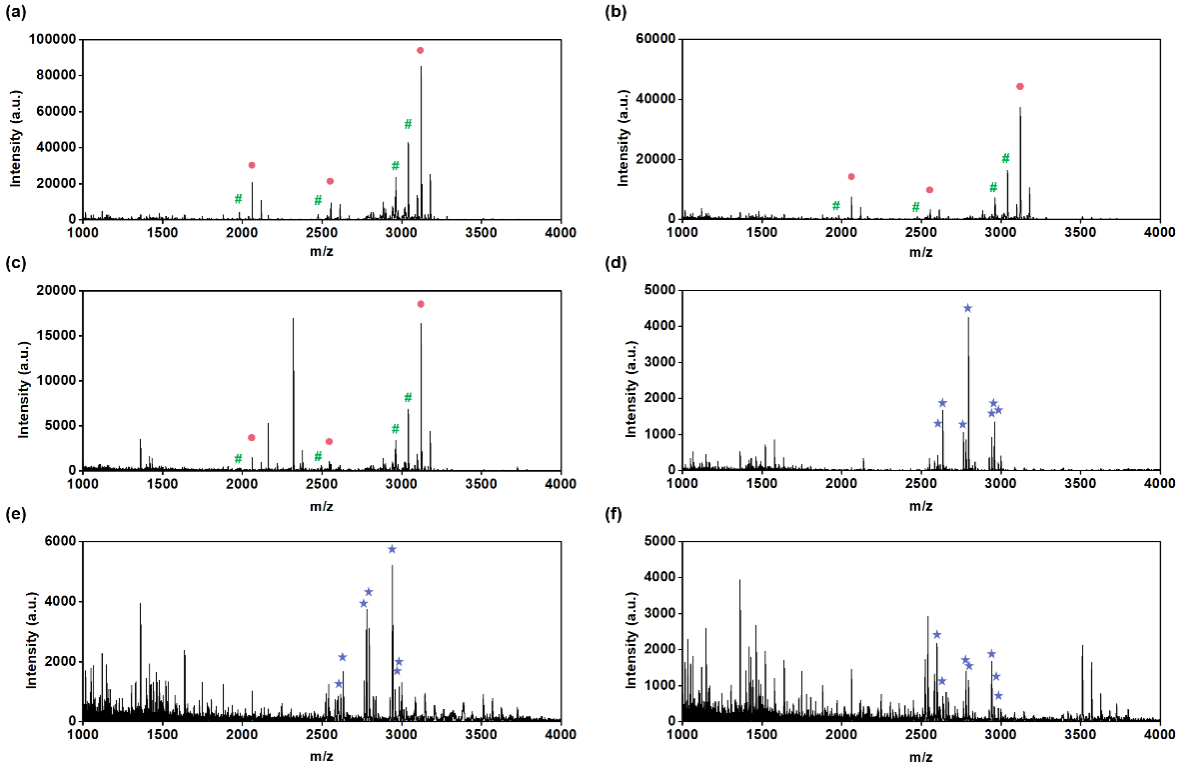

Figure 2-7. MALDI-TOF mass spectra of phosphopeptides from β-casein and BSA tryptic digest with molar ratios of (a) 1/500, (b) 1/1000 and (c) 1/5000 after enrichment by TiPCM. And MALDI-TOF mass spectra of glycopeptides from IgG and BSA tryptic digest with molar ratios of (d) 1/100, (e) 1/500 and (f) 1/1000 after enrichment by TiPCM. Phosphopeptide peaks identified are marked with the symbol ●, dephosphorylated peptide peaks identified are marked with the symbol #, and glycopeptide peaks identified are marked with the symbol ★.

Based on the low abundance of glycopeptide and phosphopeptide in the biological specimens tested, the detection sensitivity of the TiPCM was assessed, as shown in **Figure 2-8**. For the phosphopeptide enrichment, all 3 phosphopeptides could be detected from 50 fmol of trypsin digest of β-casein (**Figure 2-8a)**. When the content of the trypsin digest of β-casein was reduced to 5 fmol, all 3 phosphopeptides could still be observed (**Figure 2-8b)**. By contrast, the 23 glycopeptides could be enriched from 50 fmol of the trypsin digest of IgG, as shown in **Figure 2-8c**. Moreover, when the content of the trypsin digest of IgG was decreased to 5 fmol, the 15 glycopeptides could still be detected (**Figure 2-8)**. The above results showed that the TiPCM material exhibited a high sensitivity for the enrichment of phosphopeptides and glycopeptides.

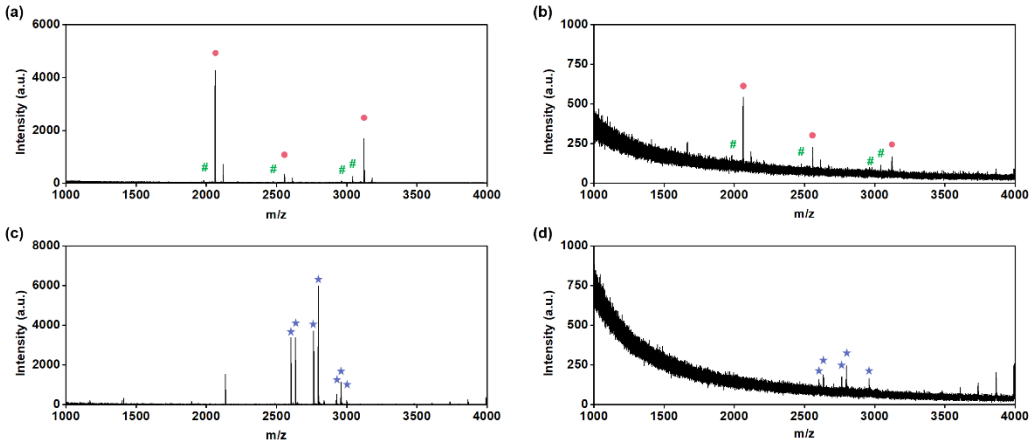

Figure 2-8. MALDI-TOF-MS spectra of (a) 50 and (b) 5 fmol of β-casein tryptic digest after enrichment by TiPCM. And MALDI-TOF-MS spectra of (c) 50 and (d) 5 fmol of IgG tryptic digest after enrichment by TiPCM. Phosphopeptide peaks identified are marked with the symbol ●, dephosphorylated peptide peaks identified are marked with the symbol #, and glycopeptide peaks identified are marked with the symbol ★.

In **Table 2-2**, the selectivity and detection sensitivity of the TiPCM are compared with other reported materials for phosphopeptides and glycopeptides. As a result, the TiPCM exhibited excellent selectivity in phosphopeptide and glycopeptide enrichment, especially in phosphopeptides which was better than other reported materials used in phosphopeptide

enrichment and the bifunctional materials used in phosphopeptide and glycopeptide enrichment. Meanwhile, **Table 2-2** can be used to compare the detection sensitivity of the TiPCM with other materials. It can be seen that its detection sensitivity exceeded the average level.

Table 2-2. Comparison of enrichment performance of different materials for phosphopeptides and glycopeptides.

Material	Selectivity of phosphopeptide [a]	Selectivity of glycopeptide [b]	Limit of detecion (fmol)	Bifunctional	Reusable [c]	Ref.
Ti^{4+}-IMAC carbonaceous spheres	1/1000	/ [d]	5	No	/	[36]
$CuFeMnO_4$	1/100	/	20	No	/	[37]
Ti^{4+}-IMAC HPHMs	1/1000	/	5	No	/	[38]
Ti_3AlC_2	1/1000	/	5	No	Yes	[39]
SPMA	1/1000	/	10	No	/	[40]
Fe_3O_4-TiNbNS	1/38	/	16	No	/	[41]
N-wood & D-wood	/	1/345	10	No	/	[42]
PSDVB–PAM	/90	1/364	/	No	/	[43]
Glu-Schiff base@SiO_2	/	1/5000	/	No	/	[44]
chitosan monolith	/	1/500	50	No	/	[45]
MoS_2/Au-NP–L-cysteine	/	1/1250	10	No	/	[46]
PNI-*co*-ATBA0.2@SiO_2	1/193	1/500	/	Yes	/	[47]
magOTfP5SOF-Ga^{3+}	1/385	1/1200	0.05	Yes	/	[48]
Ti^{4+}-immobilized MARs	1/77	1/10	1	Yes	/	[49]
TiPCM	1/5000	1/1000	5	Yes	Yes	This work

[a] β-casein/BSA (molar ratio); [b] IgG or HRP or fetuin/BSA (molar ratio); [c] For phosphopeptides enrichment; [d] The "/" means no mention in the article.

Furthermore, reusability is an important indicator for evaluating whether a material is suitably green and environmentally friendly. Generally, ammonia has been used to elute enriched phosphopeptides from a material in the process of phosphopeptide enrichment, though the combination of Ti^{4+} and the material may be destroyed in alkaline conditions. Consequently, reusability has not been considered in most studies on phosphopeptide enrichment (as shown in **Table 2-2**). To verify that the TiPCM material is indeed environmentally friendly, we used 1 mg TiPCM to enrich phosphopeptides from 0.1 μg β-casein for 5 cycles. The results are shown in **Figure 2-9**. During 5 cycles, there was no obvious difference in the phosphopeptide enrichment results, demonstrating that the TiPCM possessed good reusability.

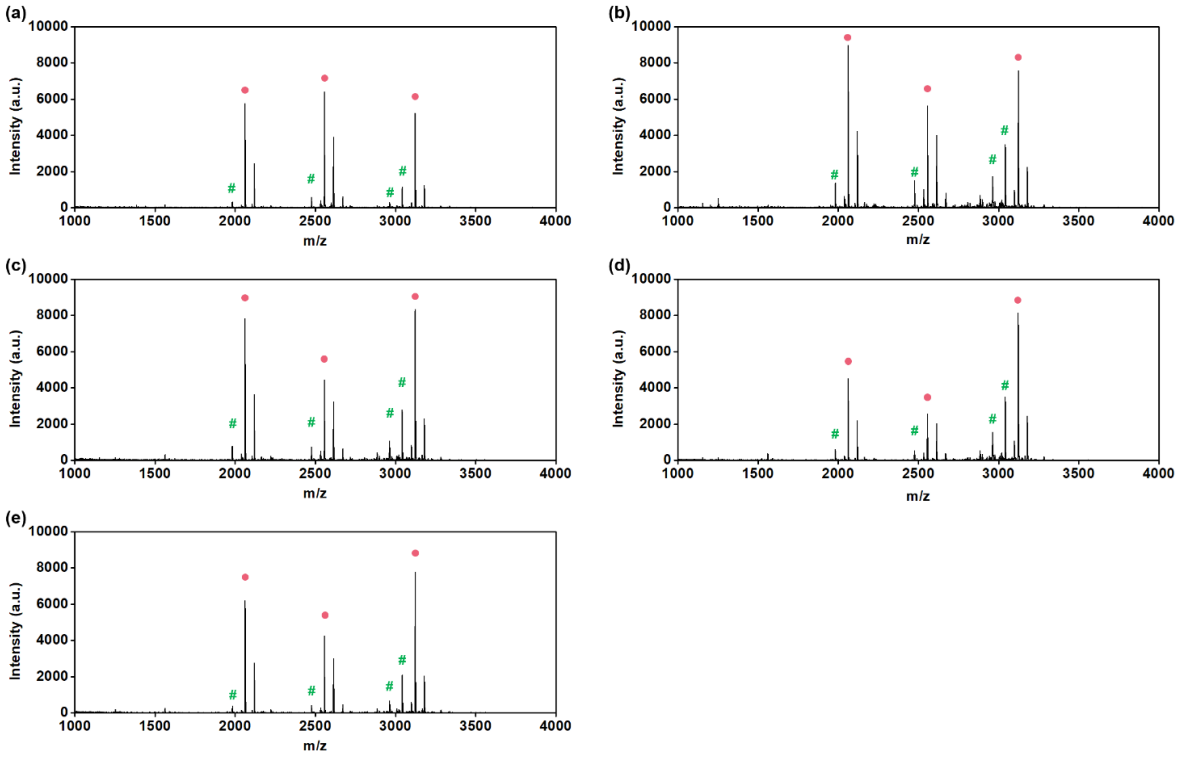

Figure 2-9. MALDI-TOF mass spectra of the tryptic digest of β-casein. The TiPCM was reused (a) 1, (b) 2, (c) 3, (d) 4, and (e) 5 times. The phosphopeptide peaks identified are marked with the symbol ●, the dephosphorylated peptide peaks identified are marked with the symbol #.

To further evaluate its phosphopeptide and glycopeptide enrichment ability, the tryptic digest of milk after enrichment with the TiPCM was analyzed via LC-MS/MS. Three parallel identifications were implemented based on **Scheme 1b**, the chromatogram obtained being analyzed by database search. It could be found that 180 unique glycopeptides and the corresponding 148 glycosylation sites from 93 glycosylated proteins could be identified from the 3 parallel tests (**Figure 2-10a**). Moreover, when 200 μg of the tryptic digest of milk enriched by the TiPCM was analyzed via LC-MS/MS, 119 unique phosphopeptides from 38 phosphorylated proteins could be identified from the 3 parallel tests (**Figure 2-10b**). The motif composition of the identified glycosylation and phosphorylation sites are shown in **Figures 2-10c** and **d**. The TiPCM exhibited promising potential for phosphopeptide and glycopeptide enrichment and is expected to be a green and efficient bifunctional material in the future.

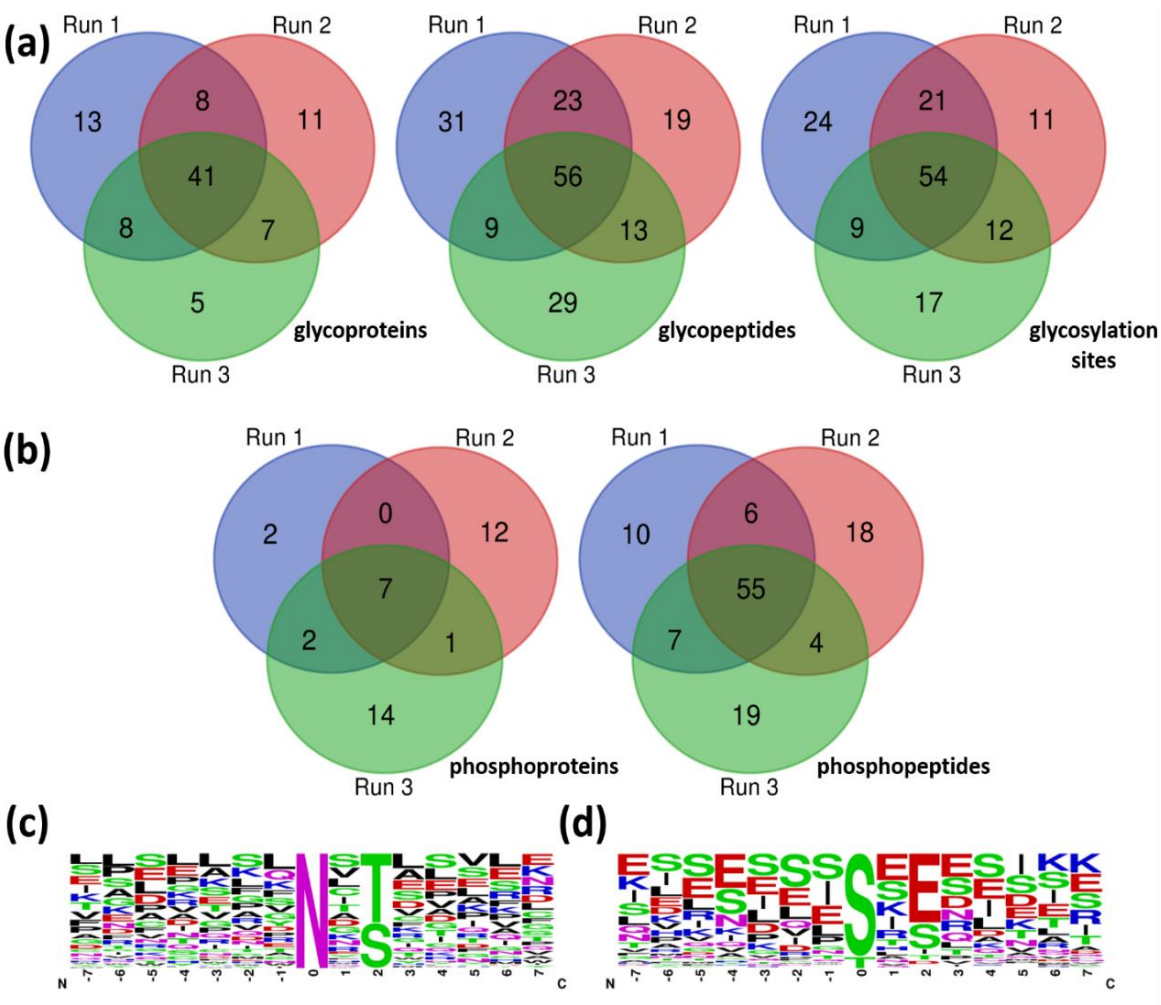

Figure 2-10. Identification results of the tryptic digest of milk after enrichment with the TiPCM via LC-MS/MS. (a) Venn diagrams of identified unique glycoproteins, glycopeptides, and glycosylation sites. (b) Venn diagrams of identified unique phosphoproteins and phosphopeptides. Motif analysis of (c) glycopeptides and (d) glycopeptides.

2.4 Conclusions

In this study, green and inexpensive cellulose as precursor was utilized to prepare a hierarchically porous monolithic material (TiPCM) with a coral-like structure. The resulting TiPCM exhibited satisfactory hydrophilicity after the CM prepared *via* TIPS was phosphorylated, resulting in a large number of metal ion affinity sites to chelate Ti^{4+}. Moreover, the TiPCM possessed the ability to simultaneously enrich both phosphopeptides and glycopeptides. Its coral-like structure increased permeability to improve the mass transfer rate between the material and the enrichment solution, and greatly reduced steric effects between the peptide and the material. Moreover, its rough surface offered myriad adsorption sites during enrichment. Consequently, the TiPCM showed excellent selective specificity and detection sensitivity for both phosphopeptides and glycopeptides. Compared with IMAC and HILIC materials with similar functions, preparation of the TiPCM was proved to be simple and green. Moreover, it could be reused to enrich phosphopeptides and flexibly enrich only phosphopeptides or both phosphopeptides and glycopeptides. It is expected to advance research on protein glycosylation and phosphorylation in the future.

2.5 References

1. P. Cohen, *Nature*, 1982, **296**, 613–620.
2. E. J. Nestler and P. Greengard., *Nature*, 1983, **305**, 583–588.
3. P. Cohen, *Nat. Cell Biol.*, 2002, **4**, E127–E130.
4. A. J. Whitmarsh and R. J. Davis., *Science*, 2016, **354**, 179–180.
5. A. S. Gajadhar, H. Johnson, R. J. Slebos, K. Shaddox, K. Wiles, M. K. Washington, A. J. Herline, D. A. Levine, D. C. Liebler and F. M. White, *Cancer Res.*, 2015, **75**, 1495–1503.
6. G. Giamas, Y. L. Man, H. Hirner, J. Bischof, K. Kramer, K. Khan, S. S. Ahmed, J. Stebbing and U. Knippschild, *Cell. Signal.*, 2010, **22**, 984–1002.
7. P. Cohen, *Eur. J. Biochem.*, 2001, **268**, 5001–5010.
8. Y. Jiang, A. Sun, Y. Zhao, W. Ying, H. Sun, X. Yang, B. Xing, W. Sun, L. Ren, B. Hu, C. Li, L. Zhang, G. Qin, M. Zhang, N. Chen, M. Zhang, Y. Huang, J. Zhou, Y. Zhao, M. Liu, X. Zhu, Y. Qiu, Y. Sun, C. Huang, M. Yan, M. Wang, W. Liu, F. Tian, H. Xu, J. Zhou, Z. Wu, T. Shi, W. Zhu, J. Qin, L. Xie, J. Fan, X. Qian and F. He, *Nature*, 2019, **567**, 257–261.
9. P. Blume-Jensen and T. Hunter., *Nature*, 2001, **411**, 355–365.
10. Y. Tian, Y. Zhou, S. Elliott, R. Aebersold and H. Zhang, *Nat. Protoc.*, 2007, **2**, 334–339.
11. A. Helenius and M. Aebi., *Science*, 2001, **291**, 2364–2369.
12. S. Hakomori, *Cancer Res.*, 1985, **45**, 2405–2414.
13. H. H. Freeze, *J. Biol. Chem.*, 2013, **288**, 6936–6945.
14. C. A. Reis, H. Osorio, L. Silva, C. Gomes and L. David, *J. Clin. Pathol.*, 2010, **63**, 322–329.
15. S. S. Pinho and C. A. Reis, *Nat. Rev. Cancer*, 2015, **15**, 540–555.
16. T. Cell Press Editorial, *Cell*, 2020, **180**, 1.
17. S. Kumar, V. K. Maurya, A. K. Prasad, M. L. B. Bhatt and S. K. Saxena, *Virusdisease*, 2020, **31**, 13–21.
18. G. Durand and N. Seta., *Clin. Chem.*, 2000, **46**, 795–805.
19. T. M. Block, M. A. Comunale, M. Lowman, L. F. Steel, P. R. Romano, C. Fimmel, B. C.

Tennant, W. T. London, A. A. Evans, B. S. Blumberg, R. A. Dwek, T. S. Mattu and A. S. Mehta., *Proc. Natl. Acad. Sci. U. S. A.*, 2005, **102**, 779–784.

20. A. Leitner, *Trends Anal. Chem.*, 2010, **29**, 177–185.
21. Matthew P. Stokes, Charles L. Farnsworth, Albrecht Moritz, Jeffrey C. Silva, Xiaoying Jia, Kimberly A. Lee, Ailan Guo, Roberto D. Polakiewicz and M. J. Comb., *Mol. Cell. Proteomics*, 2012, **11**, 187–201.
22. H. Zhou, M. Ye, J. Dong, E. Corradini, A. Cristobal, A. J. Heck, H. Zou and S. Mohammed, *Nat. Protoc.*, 2013, **8**, 461–480.
23. Y. Hu, B. Jiang, Y. Weng, Z. Sui, B. Zhao, Y. Chen, L. Liu, Q. Wu, Z. Liang, L. Zhang and Y. Zhang, *Nat. Commun.*, 2020, **11**, 6226.
24. J. Porath, *Trends Anal. Chem.*, 1988, **7**, 254–259.
25. H. Zhang, X. J. Li, D. B. Martin and R. Aebersold, *Nat. Biotechnol.*, 2003, **21**, 660–666.
26. S. Mysling, G. Palmisano, P. Højrup and M. Thaysen-Andersen., *Anal. Chem.*, 2010, **82**, 5598–5609.
27. G. Qing, J. Yan, X. He, X. Li and X. Liang, *TrAC, Trends Anal. Chem.*, 2020, **124**, 115570.
28. P. Gallezot, *Chem. Soc. Rev.*, 2012, **41**, 1538–1558.
29. Z. T. Xie, T. A. Asoh, Y. Uetake, H. Sakurai and H. Uyama, *Carbohydr. Polym.*, 2020, **247**, 116723.
30. S. Mizuno, T. A. Asoh, Y. Takashima, A. Harada and H. Uyama, *Chem. Commun.*, 2020, **56**, 14408–14411.
31. Y. Xin, Q. Xiong, Q. Bai, M. Miyamoto, C. Li, Y. Shen and H. Uyama, *Carbohydr. Polym.*, 2017, **157**, 429–437.
32. Y. Huang and Y. Fu, *Green Chem.*, 2013, **15**, 1095.
33. D. Huang, F. Benzoni, H. Fukami, N. Knowlton, N. D. Smith and A. F. Budd, *Zool. J. Linn. Soc.*, 2014, **171**, 277–355.
34. B. G. Fiss, L. Hatherly, R. S. Stein, T. Friščić and A. Moores, *ACS Sustainable Chem. Eng.*, 2019, **7**, 7951–7959.
35. Z. Xiong, Y. Chen, L. Zhang, J. Ren, Q. Zhang, M. Ye, W. Zhang and H. Zou, *ACS applied*

materials & interfaces, 2014, **6**, 22743–22750.

36. H. Zhang, X. Li, S. Ma, J. Ou, Y. Wei and M. Ye, *Green Chem.*, 2019, **21**, 2052–2060.
37. X. Y. Long, Z. J. Zhang, J. Y. Li, D. Sheng and H. Z. Lian, *Anal. Chem.*, 2017, **89**, 10446–10453.
38. H. Zhang, J. Ou, Y. Yao, H. Wang, Z. Liu, Y. Wei and M. Ye, *Anal. Chem.*, 2017, **89**, 4655–4662.
39. X. Li, N. Zhang, R. Tang, J. Lyu, Z. Liu, S. Ma, J. Ou and M. Ye, *Nanoscale*, 2021, **13**, 2923–2930.
40. B. Luo, M. Yang, P. Jiang, F. Lan and Y. Wu, *Nanoscale*, 2018, **10**, 8391–8396.
41. X. Chen, S. Li, X. Zhang, Q. Min and J. J. Zhu, *Nanoscale*, 2015, **7**, 5815–5825.
42. Y. Zhou, X. Sheng, J. Garemark, L. Josefsson, L. Sun, Y. Li and Å. Emmer, *Green Chem.*, 2020, **22**, 5666–5676.
43. Y. Song, X. Li, J. B. Fan, H. Kang, X. Zhang, C. Chen, X. Liang and S. Wang, *Adv. Mater.*, 2018, **30**, e1803299.
44. Y. Xiong, X. Li, M. Li, H. Qin, C. Chen, D. Wang, X. Wang, X. Zheng, Y. Liu, X. Liang and G. Qing, *J. Am. Chem. Soc.*, 2020, **142**, 7627–7637.
45. L. Zhang, S. Ma, Y. Chen, Y. Wang, J. Ou, H. Uyama and M. Ye, *Anal. Chem.*, 2019, **91**, 2985–2993.
46. C. Xia, F. Jiao, F. Gao, H. Wang, Y. Lv, Y. Shen, Y. Zhang and X. Qian, *Anal. Chem.*, 2018, **90**, 6651–6659.
47. Q. Lu, C. Chen, Y. Xiong, G. Li, X. Zhang, Y. Zhang, D. Wang, Z. Zhu, X. Li, G. Qing, T. Sun and X. Liang, *Anal. Chem.*, 2020, **92**, 6269–6277.
48. H. Zheng, J. Jia, Z. Li and Q. Jia, *Anal. Chem.*, 2020, **92**, 2680–2689.
49. R. Tang, Y. Yu, J. Dong, Y. Yao, S. Ma, J. Ou and M. Ye, *Anal. Chim. Acta*, 2021, **1144**, 111–120.

Chapter 3.

Integration of covalent organic frameworks into hydrophilic membrane with hierarchical porous structure for fast adsorption of metal ions

3.1 Introduction

There are generally two or three types of pore structures in hierarchical porous materials (micropores, < 2 nm; mesopores, 2-50 nm; macropores, > 50 nm), and the hierarchically porous structures commonly exist in both animal and plant tissues[1, 2]. The evolution by natural selection has endowed many classes of organisms with hierarchically porous networks, to achieve transfer and exchange of substances with extremely high efficiency and minimum energy consumption. To date, depending on the chemical composition, the hierarchical porous monoliths mainly include silica monolithic materials[3], organic polymer monoliths[4-6], zeolite monoliths[7, 8], carbon-based monoliths[9, 10], and metal-organic framework (MOF) monoliths[11], which benefit from their unique pore structure and physicochemical properties, and are widely used in adsorption, energy storage and catalysis[12-16]. Among them, zeolite and MOF generally are powder, and have adjustable microporous or mesoporous structure. The most common method for preparing them into monolithic materials is freeze-drying[17-19]. The powder material is first dispersed in a solvent and frozen at a low temperature, and then the bulk hierarchical porous material can be obtained by freeze-drying. The prepared hierarchical porous monolith by the method possesses various kinds of pore structure containing macropores, micropores and mesopores which can independently exert their function.

In recent years, covalent organic frameworks (COFs) fast developed that are a new type of porous organic materials with high crystallinity and ordered nanopores structure[20-23]. COFs showed many advantages including adjustable pore structure, high surface area, high thermal stability which can applied in in various fields as gas storage, adsorption, catalysis, and other fields. However, the prepared COFs are generally powder which makes them inconvenient to

use in practical application. Meanwhile, the highly stacked structure existed in COF restrict the diffusion rate of ions that lead to slow adsorption rate in heavy metal adsorption. So far, there is a challenge that is the preparation of hierarchical porous monolithic COFs. Although COF membrane with a thickness of 4 μm has been fabricated [24], such COF membrane showed poor mass transfer efficiency due to the lack of macropores[25-27]. Therefore, a method that could use in the preparation hierarchical porous COF monolith with macropores should be developed. Recent years, a number of materials based on chitosan have been reported and used for adsorption[28, 29]. Although those chitosan-based materials showed poor capability in heavy metal adsorption due to low specific surface area, it enlightened us to fabricate a chitosan-based hierarchical porous COF monolith.

Considering those matters, our group fabricated a COF-loaded chitosan films (ChM-COF and COF-ChM) using chitosan, poly(ethylene glycol) diglycidyl ether (PEGDE), 1,3,5-triformylphloroglucinol (TP), oxalyldihydrazide (ODH) and acetic acid as catalyst in the presence of mesitylene and 1,4-dioxane. The resulting ChM-COF are monolithic membrane materials to overcome disadvantages of COF powder. More importantly, it possessed hierarchical porous structure containing mesoporous and macroporous structure and higher specific surface area. Benefiting from its hierarchical porous structure, ChM-COF showed favorable performance in heavy metal adsorption.

3.2 Experimental Section

3.2.1 Chemicals and materials

Chitosan, TP, ODH, potassium dichromate ($K_2Cr_2O_7$) and cupric chloride ($CuCl_2$) were purchased from Macklin Biochemical Co., Ltd. (Shanghai, China). 1,4-Dioxane, tetrahydrofuran (THF), N,N-dimethylformamide (DMF), acetone, mesitylene hydrochloric acid, phosphoric acid and sulfuric acid were acquired from Tianjin Kermel Chemical Plant (Tianjin, China). Acetic acid, PEGDE, sodium diethyldithiocarbamate and 1,5-diphenylcarbazide were obtained from Aladdin (Shanghai, China). Deionized water used in whole experiments was gotten from a Milli-Q system (Millipore Inc., Milford, MA).

3.2.2 Individual preparation of COF and chitosan membrane

The preparation process of COF was described in our previous report[30]. ODH (0.15 mmol) and Tp (0.10 mmol) were weighed at an ampoule bottle and dissolved in anhydrous 1,4-dioxanec (500 μL) and mesitylene (500 μL). After the solution was sonicated for 30 min, aqueous acetic acid (6 mol L^{-1}, 0.4 mL) was added in the ampoule bottle. The ampoule bottle was then placed in liquid nitrogen which made the solution rapidly frozen, and evacuated air until its interior pressure dropped below 5 kPa. Subsequently, the ampoule bottle was sealed with flame of butane, and placed in oil bath at 120 ℃ for 72 h. The resulting brown solid was washed by DMF and THF, then dried in vacuum drying oven at 100 ℃ for 12 h to obtain final COF materials.

The synthetic method of chitosan membrane has been recently reported by our group[31]. In brief, a 1-mm-thick biomimetic honeycomb chitosan membrane (chitosan monolith) with honeycomb-like accessible macropores was directly prepared by the freeze-casting method.

3.2.3 Preparation of COF-loaded chitosan films

As show in **Scheme 3-1a**, a certain mass of ODH and TP were dissolved in anhydrous 1,4-dioxanec and mesitylene, respectively, and sonicated for 15 min, which were added in an ampoule bottle containing a certain amount of chitosan membrane and sonicated for 15 min

again. The ampoule bottle was placed in liquid nitrogen to rapidly freeze the mixture, and evacuated air until its pressure of interior dropped below 5 kPa. Other experimental procedures were same as Section 2.2. Finally, the resulting material of ChM-COF was synthesized.

As show in **Scheme 3-1b**, a certain mass of COF and a solution containing chitosan, acetic acid, H_2O and PEGDE were sonicated to form a suspension solution. The resulting mixture was transferred to a metal plate as a mold, and a film was fabricated by the freeze-casting method as mentioned above[31]. Then, the resulting membrane was washed by DMF and THF, and dried in vacuum drying oven at 100 ℃ for 12 h to obtain final materials COF-ChM.

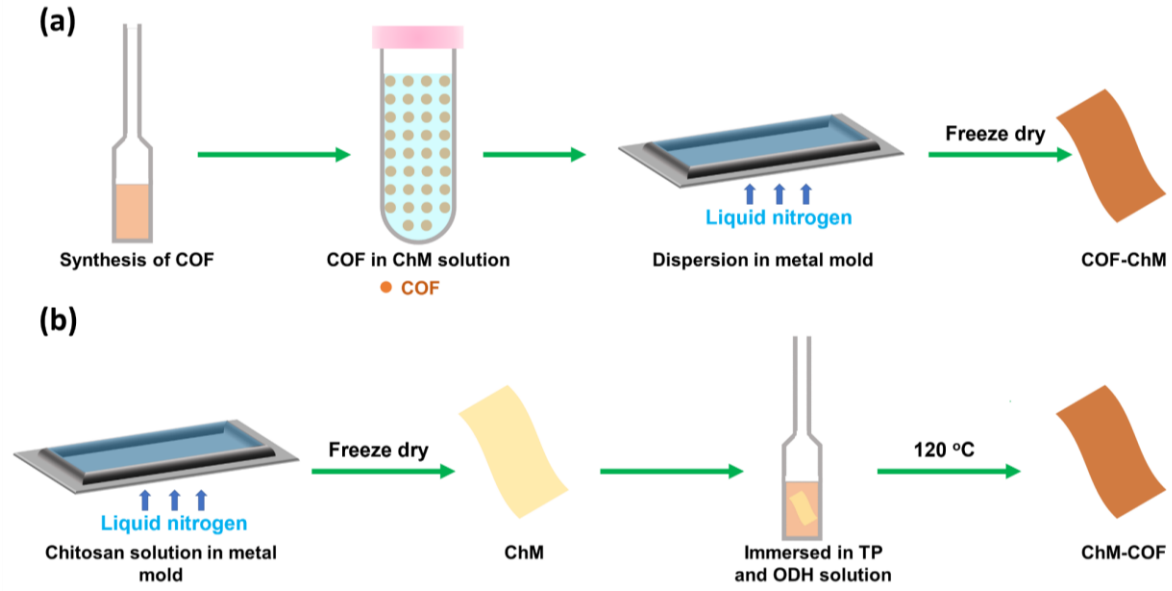

Scheme 3-1. Schematic representation for construction of (a) ChM-COF and (b) COF-ChM.

3.2.4 Adsorption of metal ions

A 50 mL brown volumetric flask was added with 500 mg sodium diethyldithiocarbamate and deionized water to tick mark as copper reagent. A series of standard solutions were prepared at concentrations 0.5, 1.0, 1.5, 2.0 and 2.5 μg mL^{-1} Cu(II) aqueous solution (25 mL) containing starch indicator (1 mL, 10 g L^{-1}), NH_4Cl-$NH_3 \cdot H_2O$ buffer solution (2 mL, pH 9.25) and sodium diethyldithiocarbamate (0.2 μL). Standard curve could be obtained through measuring absorbance of Cu(II) ion standard solutions.

A certain amount of $CuCl_2 \cdot 2H_2O$ was dissolved in the appropriate amount of deionized water with a 500 mL beaker, and the pH of solution was adjusted to 6 by 1 mol L^{-1} NaOH

aqueous. Then the solution was poured into a 500 mL volumetric flask and calibrated to its mark using deionized water. Ten milligrams of chitosan-loaded COF films were weighed at a 15 mL centrifuge tube containing 10 mL $CuCl_2$ aqueous solution above mentioned, which was shaken at room temperature for 24 h. Then, a certain amount of $CuCl_2$ solution adsorbed by chitosan-loaded COF film was transferred to 25 mL volumetric flask, added starch-iodide indicator (1 mL, 10 g L^{-1}), NH_4Cl-$NH_3 \cdot H_2O$ buffer solution (2 mL, pH 9.25) and copper reagent (0.2 μL) and then deionized water to tick mark. Finally, absorbance of the solution was measured to calculate adsorption capacity of chitosan-loaded COF film for Cu(II) ion.

A 50 mL brown volumetric flask was added 200 mg diphenyl carbamide and acetone to calibrated mark as chromogenic agent. A series of standard solutions were prepared at concentrations 0.1, 0.2, 0.3, 0.5, 0.7 and 0.9 μg mL^{-1} Cr(VI) aqueous solution (25 mL) containing diphenyl carbamide indicator (2 mL, 4 g L^{-1}), 50% phosphoric acid solution (0.5 mL) and 50% sulfuric acid solution (0.5 mL). Standard curve could be obtained through measuring absorbance of Cr(VI) ion standard solutions.

A 500 mL volumetric flask was added a certain amount of potassium dichromate then the pH was adjusted to 6 and deionized water to tick mark. Ten milligrams of ChM-COF were weighed at a 15 mL centrifuge tube containing 10 mL $K_2Cr_2O_7$ aqueous solution above mentioned, which was shaken at room temperature for 24 h. Then, a certain amount of $K_2Cr_2O_7$ solution adsorbed by chitosan-loaded COF film was transferred to 25 mL volumetric flask, added diphenyl carbamide solution (2 mL, 4 g L^{-1}), 50% phosphoric acid solution (0.5 mL) and 50% sulfuric acid solution (0.5 mL) and calibrated to mark of volumetric flask using deionized water. Finally, absorbance of the solution was measured to calculate adsorption capacity of chitosan-loaded COF film for Cr(VI) ion.

3.2.5 Instruments and methods

The microstructure and pore morphology of materials were observed by scanning electron microscopy (SEM) (JEOL JSM-5600, Tokyo, Japan). Thermogravimetric analysis curve was carried out SDT Q600 (TA Instrument Corp., USA). The attenuated total reflection-Fourier transformed infrared spectroscopy (ATR-FTIR) was collected on Thermo Nicolet 380

spectrometer (Nicolet, Wisconsin, USA). Pore size distribution and specific surface area of materials were measured by Micrometrics Surface (Micrometrics, USA) after outgassed under vacuum for at least 8 h at 120 ℃. The powder X-ray diffraction (XRD) patterns were obtained on PANalytical X'Pert Pro Multipurpose Diffractometer using Cu Kα radiation at 40 kV and 40 mA at room temperature. X-ray photoelectron spectroscopy (XPS) characterization was taken using ESCALAB 250Xi XPS spectrometer with an Al Kα X-ray source (Thermo Scientific, USA).

3.3 Results and discussion

3.3.1 Preparation of COF-loaded chitosan membranes

Although a 1-mm-thick chitosan monolith with accessible macropores in our previous report shows excellent enrichment capability for glycopeptides, low specific surface area limits its application prospects in other fields because chitosan monolith has only macropores and no mesopores/micropores[31]. Therefore, it is necessary to increase the specific surface area of chitosan monolith by loading COFs which could provide a large number of micropores or mesopores. In our previous report, we have tried to synthesize a COF-based monoliths as an adsorbent of bisphenol A through ring-opening polymerization and found that the micropores/mesopores of COF were easily blocked after adsorption of precursors and polymerization, resulting in low specific surface area[32]. Considering the above situation, we designed two ways to load COF on chitosan monolith, as shown in **Scheme 3-1**. First, the COF was fabricated and then used as a precursor to form COF-integrated chitosan membrane, which was assigned as COF-ChM. Second, the 1-mm-thick chitosan monolith was prepared and then used an additive into a suspension containing ODH and TP, resulting in the formation of a layer of COF onto chitosan monolith, that is, ChM-COF. The detailed composition for fabrication of chitosan membrane, COF and COF-loaded chitosan membranes (COF-ChM and ChM-COF) are shown in **Table 3-1**.

Table 3-1. Detailed composition for fabrication of ChM, COF, COF-ChM and ChM-COF and results of Cu(II) adsorption.

Materials	Chitosan (mg)	Tp (mg)	ODH (mg)	COF (mg)	Specific surface area ($m^2 g^{-1}$)	Cu(II) adsorption capacity (mg g^{-1})
ChM	40.0	/	/	/	0.4	20
COF	0	63.0	53.1	/	298.1	/
COF-ChM-1	40.0	/	/	10.0	10.5	/
COF-ChM-2	40.0	/	/	40.0	44.8	37
ChM-COF-1	40.0	63.0	53.1	/	34.5	/
ChM-COF-2	40.0	47.3	26.6	/	65.2	59

ChM-COF-3	40.0	63.0	26.6	/	101.9	104
ChM-COF-4	40.0	94.5	53.1	/	117.4	131
ChM-COF-5	40.0	189.0	53.1	/	110.1	131

3.3.2 Characterization of COF-loaded chitosan membranes

In order to investigate their morphology, both COF and chitosan-loaded COF membranes (COF-ChM and ChM-COF) were characterized through SEM as shown in **Figure. 3-1a** and **b**. It could be found that crystallized COF exhibited chrysanthemum-like structure assembled by the petals about 2 μm long, 150-300 nm wide and 20-40 nm thick, while COF-ChM, in which COF was integrated into chitosan membrane, exhibited various morphology (**Figure. 3-1c** and **d**). As shown in **Figure. 3-1d**, the COF particles were totally wrapped in the membrane, and chrysanthemum-like structure could hardly be observed. Some COF particles were inserted into thin chitosan membrane, looking like transmembrane protein, and their coarse surface still existed in **Figure. 3-1d**. Meanwhile, larger COF particles appeared in the holes of honeycomb-like membrane, and their chrysanthemum-like structure was perfectly preserved (**Figure. 3-1c**). These structures were related to the results why COF-ChM exhibited relatively lower Brunauer–Emmett–Teller (BET) surface area (44.8 m^2 g^{-1}) than ChM-COF (117.4 m^2 g^{-1}). However, in **Figure. 3-1e** and **f**, a layer of COF-based coating uniformly formed on chitosan membrane, and their crystallized morphology was similar as pure COFs.

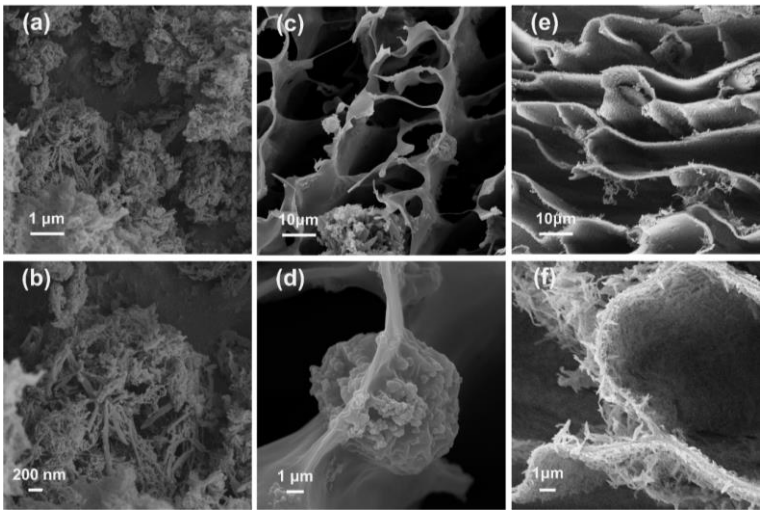

Figure. 3-1. SEM images of (a, b) COF, (c, d) COF-ChM and (e, f) ChM-COF (at 10000×, 20000×, 1000×, 5000×, 1000× and 5000× magnification, respectively).

ATR-FTIR can reflect the functional group construction existed in chitosan, COF, and chitosan-loaded COF membranes (COF-ChM and ChM-COF). In **Figure. 3-2a**, the spectrum of chitosan showed the stretch vibration of −OH and −NH groups at 3354 cm^{-1}, −CH at 2940 and 2870 cm^{-1}, amide II band at 1648 (C−O) and 1593 cm^{-1} (N−H), and C−O at 1058 cm^{-1}. The signals peaks at 1282 and 1593 cm^{-1} were assigned −C−N− and −C=C− stretch in COF, respectively, indicating the characteristic peaks of β-ketoenamine linkages. The ordered structure of COF and two kinds of COF-integrated membranes (COF-ChM and ChM-COF) could be characterized by PXRD. Corresponding to the reflection from the 100 plane, a strong peak at 4.5°±0.2° (2θ) with *d* spacing of 19.4 Å existed in COF. In addition, the 001 plane reflection was reflected by a broad peak at higher 2θ value (~27.6°±0.2°) with *d* spacing of 3.2 Å arose in **Figure. 3-2b**, which proved successive layers in COF with π-π stacking. Other characteristic peaks of COF-ChM and ChM-COF (Fig. 3B) in PXRD pictures were similar with those of COF, further indicating that the COFs successfully formed onto chitosan membrane. **Figure. 3-2c** shows TGA diagrams of COF, ChM-COF and COF-ChM under atmosphere. The weight loss of COF, ChM-COF and COF-ChM were apparently found in the range of 300-700 ℃. These results indicated that the two materials (ChM-COF and COF-ChM) possess good thermal stability.

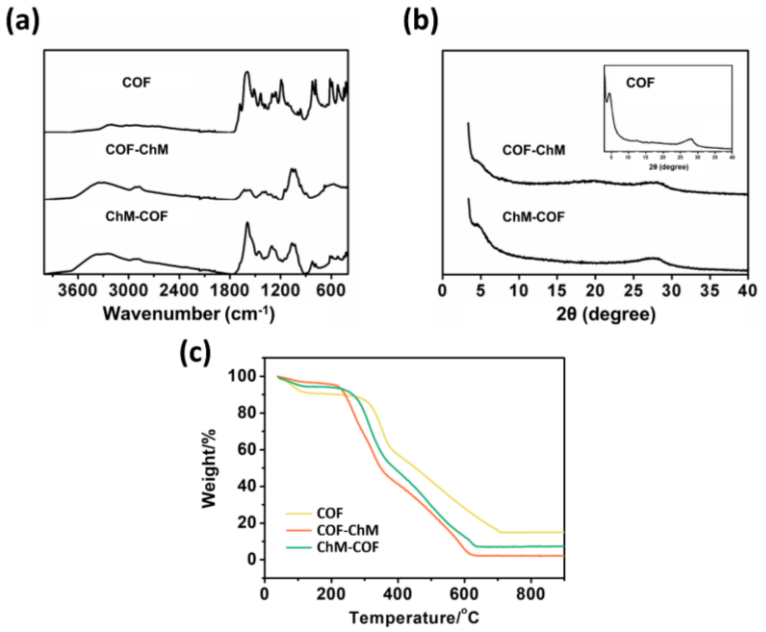

Figure. 3-2. (a) FT-IR spectra, (b) PXRD patterns and (c) TGA analysis results of COF, COF-CHM and CHM-COF.

Pore size distribution and specific surface area of these materials were investigated by using nitrogen sorption/desorption isotherm measurements. As shown in **Figure. 3-3**, the chitosan membrane possessed extremely low BET surface area (0.4 m^2 g^{-1}). On the contrary, the COF exhibited higher BET surface area (298.1 m^2 g^{-1}) and narrow pore size distribution of 4 nm. Chitosan-loaded COF membrane, the combination of COFs and chitosan membrane, showed moderate surface areas ranging in those of COF and chitosan membrane. As shown in **Table 3-1**, the BET surface areas of COF-ChM increased from 10.5 to 44.8 m^2 g^{-1} with an increase of the content of COF. As for ChM-COF-1, the BET surface area of ChM-COF^{-1} was 34.5 m^2 g^{-1} when the molar ratio of TP/ODH was kept at 1.5/1. The BET surface area of ChM-COF-2 increased to 65.2 m^2 g^{-1} with increasing the molar ratio of TP/ODH (2/1). When the molar ratio of TP/ODH in system exceeded to 4/1, the BET surface areas of ChM-COF were constant and approximately maintained 110.4 m^2 g^{-1}. The reason for this phenomenon was due to the consumption of aldehyde group in Tp reacted with amino group in chitosan, which caused the

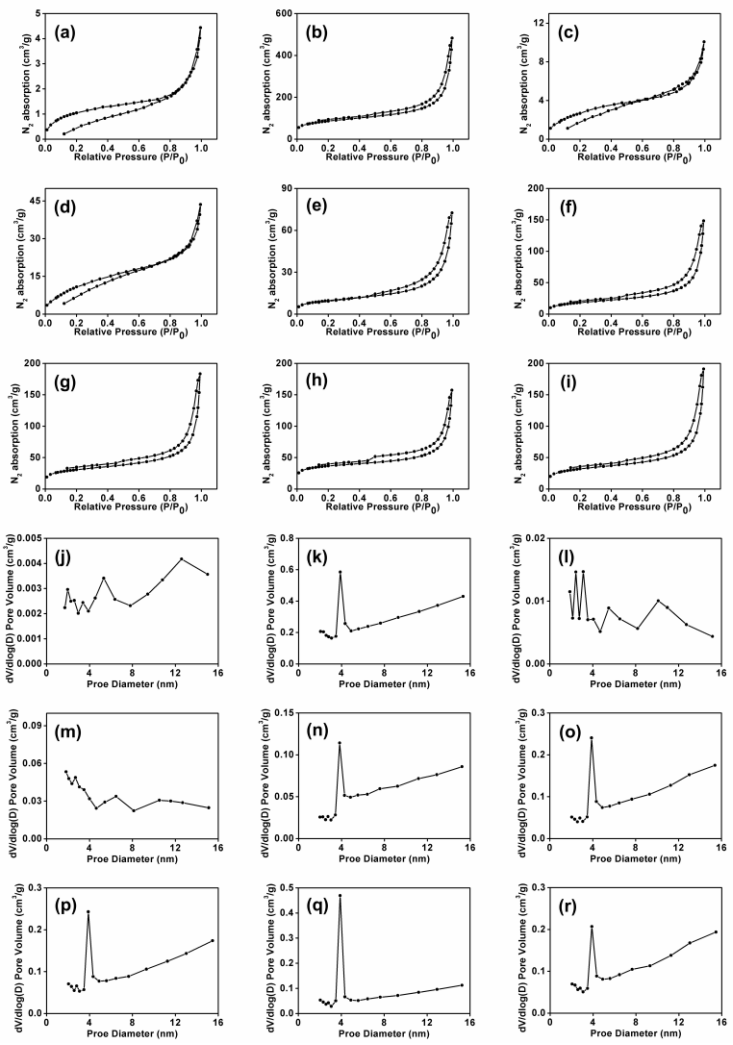

Figure. 3-3. Nitrogen adsorption-desorption isotherms (77 K) of (a) ChM, (b) COF, (c, d) COF-CHM-1 and COF-CHM-2 and (e-i) CHM-COF-1-5, respectively. Pore size distribution of (j) ChM, (k) COF, (l, m) COF-CHM-1 and COF-CHM-2 and (n-r) CHM-COF-1-5, respectively.

overplus of ODH and generated less COFs onto ChM-COF. Additionally, broad pore size distributions (**Figure. 3-3l** and **m**) of COF-ChM-1 and COF-ChM-2 were similar with that of pristine chitosan membrane (**Figure. 3-3j**), while ChM-COF-1-5 possessed narrow pore size distributions of 4 nm (**Figure. 3-3n-r**). These results proved that the resulting chitosan-loaded COF membranes (COF-ChM and ChM-COF) exhibited hierarchical porous structure.

3.3.3 Adsorption ability of COF-loaded chitosan membranes for metal ions

According to the previous report[30], the resulting COF contained aromatic rings and C=N bonds with abundant π-conjugated system and there were considerable −OH bonds in chitosan, which offered the COF-loaded chitosan membranes more possibility to interact with metal ions. In the context, the ChM-COF and COF-ChM was used to adsorb Cu(II). As shown in **Table 3-1**, ChM-COF shows better Cu(II) adsorption performance than COF-ChM in same conditions (pH = 6, Cu(II) concentration = 3 mmol L^{-1}). As mentioned above, COF was wrapped by ChM in the SEM image of COF-ChM and possessed relatively lower specific surface area of COF-ChM. These results demonstrated the COF-ChM did not have the advantage in adsorption of metal ions. Therefore, ChM-COF was selected for subsequent experiments. Adsorption isotherm plays a vital role in the design of adsorption process, which clearly reflects the interaction between the analytes and adsorbent. The adsorption isotherms for Cu(II) and Cr(VI) ions were respectively plotted to evaluate the adsorption ability of ChM-COF for metal ions, and the detailed results were given in **Figure. 3-4**. It could be observed that the saturated adsorption amount of ChM-COF for Cu(II) was 122 mg g^{-1} (**Figure. 3-4a**), the inset shows the Cu(II) adsorption isotherms of COF at room[30]. And the saturated adsorption amount of ChM-COF for Cr(VI) was 388 mg g^{-1} (**Figure. 3-4c**). The adsorption capacity of copper ions of ChM-COF decreased significantly than that of COF in previous report[30] because the specific surface area of ChM-COF was lower than that of COF itself, and adsorption amount of ChM for Cu(II) was only 20 mg g^{-1}. A more detailed result of adsorption for Cu(II) was shown in **Table 3-1**. Although the priority of Cr(VI) was much lower than those of Hg(II) and Cu(II) in competitive adsorption of the COF in previous report[30], the large amounts of C=N bonds and −OH bonds in ChM-COF still endued a favorable performance of Cr(VI) adsorption. Obviously, the

adsorbed amount of ChM-COF was distinctly higher than chitosan membrane and other types materials including nanoparticles[33], porous nanocrystal[34] and double-shelled hollow microspheres[35], which should be related to abundant mesoporous and nitrogen and oxygen with the structure of chitosan-loaded COF membrane to lightly combine with Cu(II) ion.

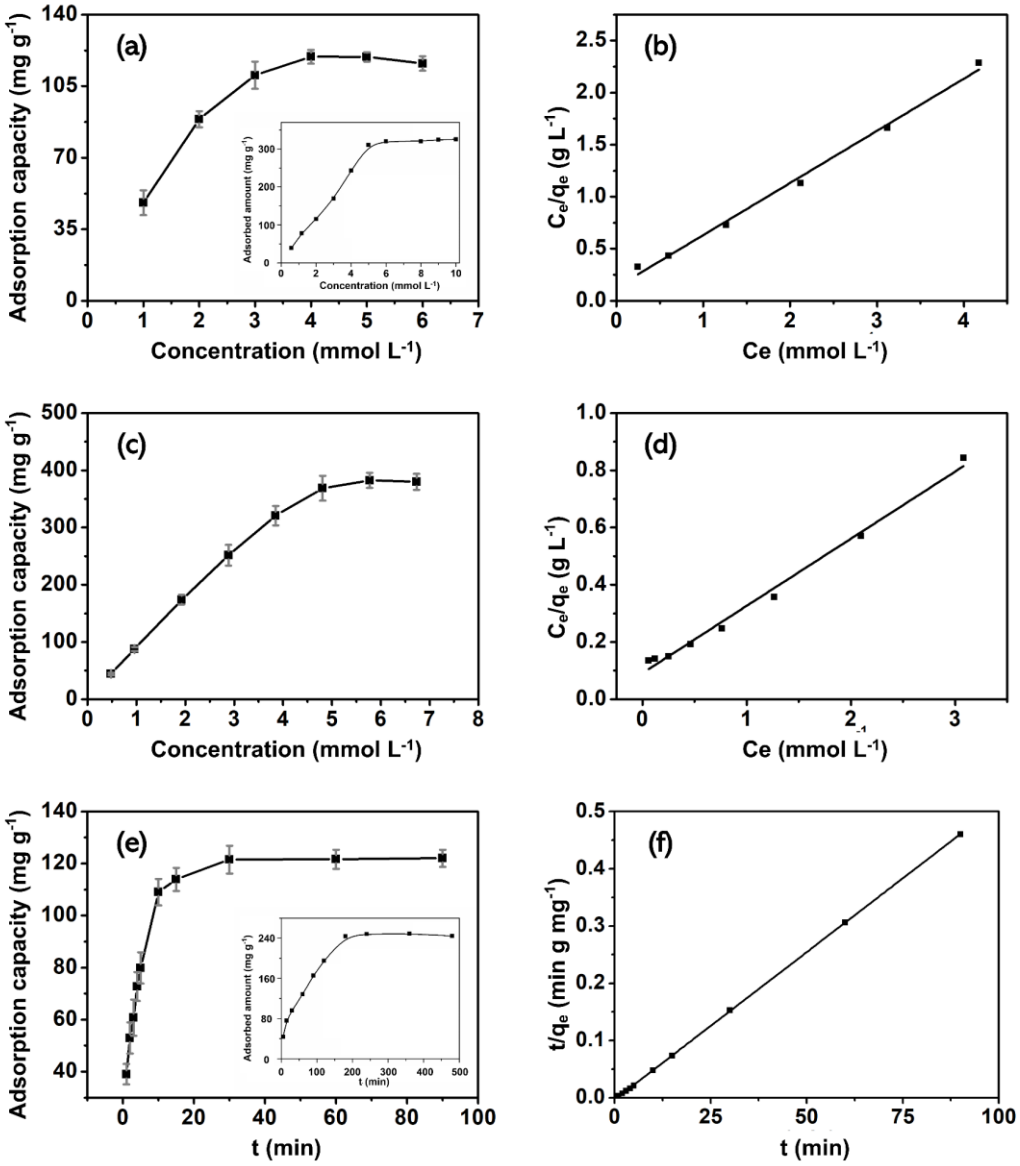

Figure. 3-4. (a) Cu(II) and (c) Cr(VI) adsorption isotherms of ChM-COF at room temperature. Inset shows the Cu(II) adsorption isotherms of COF at room. Linear regression by fitting the equilibrium data with the Langmuir adsorption model of (b) Cu(II) and (d) Cr(VI) adsorption isotherms of ChM-COF at room temperature. (e) Adsorption curve and (f) pseudo-second-order kinetic plot for the adsorption of Cu(II) versus contact time using ChM-COF at room

temperature. Inset shows the adsorption curve for the adsorption of Cu(II) versus contact time using COF at room temperature.

Through fitting the equilibrium adsorption isotherm of Cu(II) and Cr(VI), both of adsorption isotherm well matched with Langmuir model, as both of correlation coefficients were 0.993 and 0.990, respectively (**Figure. 3-4b** and **d**). Furthermore, the Freundlich adsorption models were selected to investigate the adsorption process of Cu(II) and Cr(VI) as shown in **Figure. 3-5.** It could be clearly observed that the values of Freundlich model correlation coefficient of adsorption process of Cu(II) and Cr(VI) were 0.775 and 0.883, respectively, which were lower than those of Langmuir model. These results demonstrated that the adsorption process was more suitable to Langmuir adsorption model, indicating that the adsorption was monolayer.

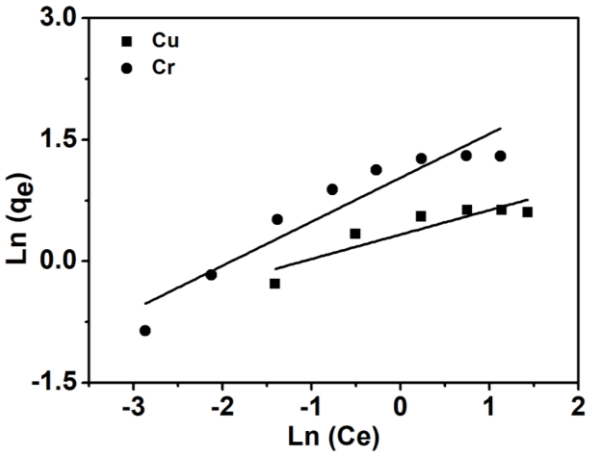

Figure. 3-5. Linear fitting of adsorption isotherm by Freundlich models of Cu(II) (■) and Cr(VI) (●) on CHM-COF at room temperature.

The kinetic behaviour of ChM-COF for Cu(II) adsorption process was presented in **Figure. 3-4e**, indicating that the adsorption process reached an equilibrium after 30 min, and the inset shows the adsorption curve for the adsorption of Cu(II) versus contact time using COF at room temperature[30]. Further fitting the curve of adsorption process, the correlation coefficient of 0.999 was acquired, demonstrating that the adsorption process of Cu(II) by ChM-COF followed the pseudo-second-order kinetic model (**Figure. 3-4f.**). It is worth mentioning that ChM-COF reached saturation of copper adsorption only after about 30 min, and exhibited higher adsorptive rate than the COF in our previous report[30], which would take 180 min to reach saturation of copper adsorption. Although the coordination between −NH− and −C=O in COF and Cu(II) showed its fast adsorption potential, the stacked structure existed in COF restrict the diffusion rate of ions which makes adsorptive rate slow. In this context, the hierarchically porous

structure in ChM-COF would lead to fast adsorptive rate and greatly improve the mass transfer rate. This phenomenon is similar to gas-phase foaming technique *in situ*, which introduce hierarchical porous structure to COF and reduce the time of adsorption equilibrium from 2 h to 10 s[36]. In addition, the resulting ChM-COF showed equal performance with the similar type of COFs, which could reach 95% of its equilibrium adsorption capacity within 30 min[37]. The Cu(II) adsorption performance of ChM-COF and other sorbents[30, 38-44] was compared in **Table 3-2**.

Table 3-2. Comparison of the adsorption performance of ChM-COF for Cu(II) with other reported adsorbents.

Adsorbent	Cu(II) adsorption capacity (mg g^{-1})	Equilibrium time (h)
TpODH[30]	324	3
CD-CA/PDA[38]	73.6	1
PEI-GA[39]	85.1	24
C2@3-HPS#500[40]	493	1
Fe_3O_4@C-SH[41]	28.8	1
GO-EDA-CAC-BPED[42]	220	4
BPA-9[43]	80.6	12
ABC[44]	49	48
ChM-COF	144	0.5

The pH of solution is one of the most important factors for affecting the adsorption of metallic ion on materials. In the context, the influence of pH was investigated from 2 to 7 for adsorption. When the pH increased from 2 to 7, it could be observed that adsorption capacity for Cu(II) and Cr(VI) gradually increased, as shown in **Figure. 3-6a**. Obviously, the reduction of H^+ would weaken the competition relationship between metallic cation and H^+, which led to the improvement of adsorption ability of membrane for metallic cation. In addition, aniline is a common pollutant in the polluted water containing heavy metallic ion. Therefore, we chose 0, 5, 10 and 20 mg L^{-1} aniline at pH 6 to investigate the effect of organic compound on the adsorption performance of ChM-COF on Cu(II) and Cr(VI). During the adsorption process, the

addition of aniline generated some complexes of aniline with metallic ion, while the ChM-COF cannot adsorb the complexes. Thus, the adsorption capacity of ChM-COF decreased with the increasing of aniline concentration, as shown in **Figure. 3-6b**. The regeneration ability and chemical stability of the adsorbent are important indicators to evaluate its adsorption performance. Therefore, the ChM-COF membrane at first were used to adsorb Cu(II) after immersed in 1 mol L^{-1} HCl aqueous and 1 mol L^{-1} NaOH aqueous for 24 h, respectively. It could be observed from **Figure. 3-6c** that the ChM-COF still exhibited good adsorption performance after suffering from HCl and NaOH aqueous. At the same time, there were no significant difference for adsorption capacity in these three conditions (original ChM-COF, 117.4 mg mL^{-1}; ChM-COF immersed in 1 mol L^{-1} HCl, 105.3 mg mL^{-1}; ChM-COF immersed in 1 mol L^{-1} NaOH, 118.6 mg mL^{-1}). In addition, as shown in **Figure. 3-6d**, the adsorption capacity of ChM-COF kept above 82% of the original after 3 times recycles of adsorption-desorption and kept above 74% of the original after 4 times recycles of adsorption-desorption. Moreover, the test of mechanical strength was implemented to explore the ChM-COF material in practical application.

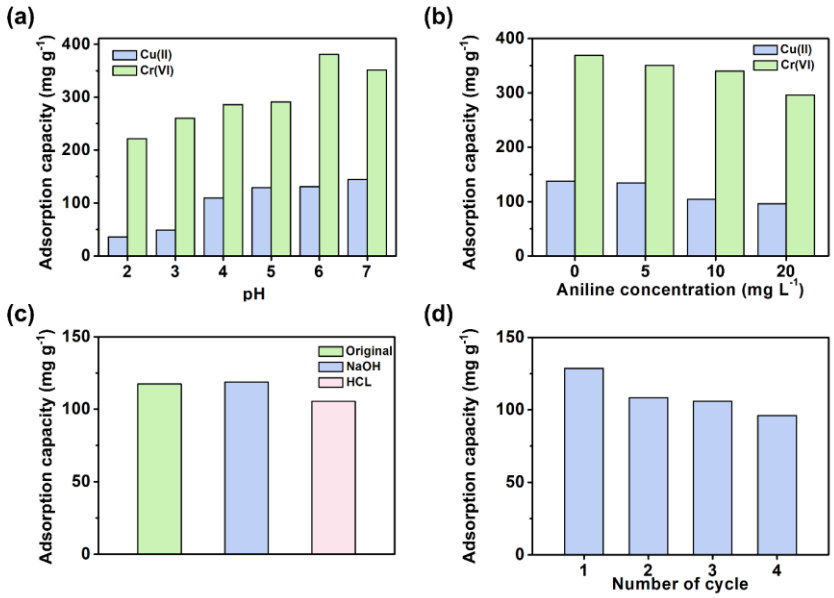

Figure. 3-6. Effects of (a) pH and (b) organic compound of the solution on Cu(II) and Cr(IV) adsorption. (c) The stability of ChM-COF in different solution (NaOH, 1 mol L^{-1}; HCl, 1 mol L^{-1}) for 24 h. (d) Adsorption efficiency of Cu(II) in recycles of adsorption-desorption.

3.3.4 Adsorption mechanism

The XPS was performed to investigate the interactions between Cu(II) ion and COF-ChM.

The XPS survey wide scan spectra of ChM_Cu, ChM-COF_Cu and COF-ChM_Cu were shown in **Figure. 3-7**. As observed in **Figure. 3-7a** and **b**, 5 characteristics peaks of C1s (284 eV), N1s (399 eV), O1s (532 eV), Cu 2p (933 eV) and Cl 2p (199 eV) existed in ChM-COF_Cu (**Figure. 3-7a**) and COF-ChM_Cu (**Figure. 3-7b**), meanwhile they also existed in ChM_Cu (**Figure. 3-7c**). This is due to a large number of amino groups in chitosan, providing the same coordination interaction between copper ions and chitosan membrane. The results proved the existence of Cu and Cl elements in ChM_Cu, ChM-COF_Cu and COF-ChM_Cu, and the metal ions were adsorbed on ChM_Cu, ChM-COF_Cu and COF-ChM_Cu through coordination interaction. In Fig. 5, the binding energies in 934.69, 934.23 and 933.47 eV corresponded to the peaks of Cu $2p_{3/2}$, while the binding energies in 954.63, 954.06 and 953.39 eV corresponded to the peaks of Cu $2p_{1/2}$. Furthermore, the binding energies in about 939, 944 and 963 eV corresponded to the satellite peaks of Cu $2p_{3/2}$ and Cu $2p_{1/2}$, indicating the presence of Cu(II). The satellite peaks were related to the interactions between Cu(II) and functional groups (−NH−, −C=O).

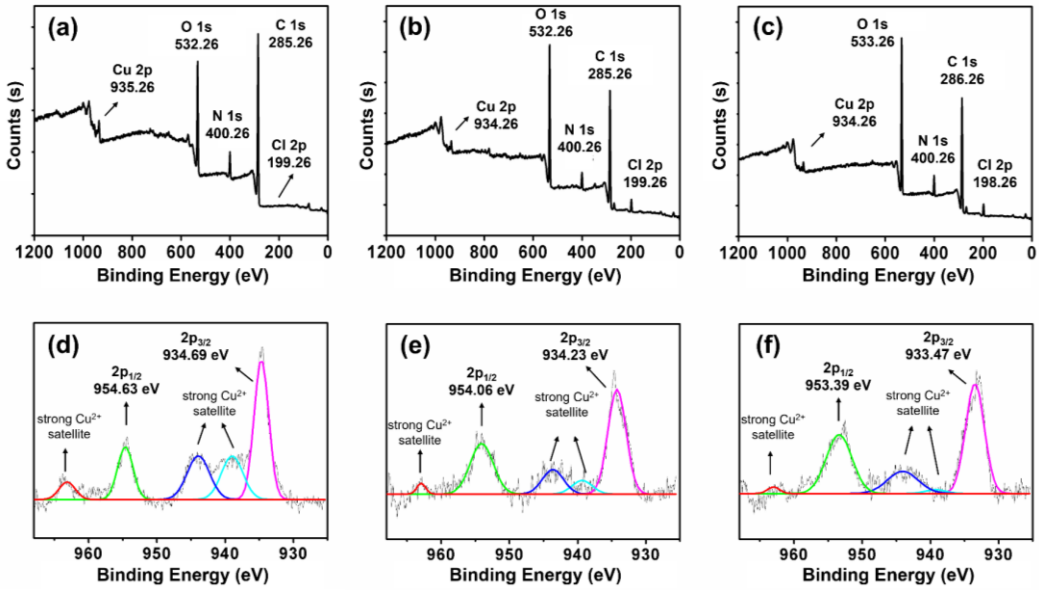

Figure. 3-7. Low-resolution XPS survey wide scans spectra of (A) ChM-COF_Cu, (B) COF-ChM_Cu and (C) ChM_Cu.XPS Cu 2p high-resolution spectra of (D) ChM-COF_Cu, (E) COF-ChM_Cu and (F) ChM_Cu.

As described in previous reports, copper possessed affinity with the especially high affinity capacity for nitrogenous ligands according to hard and soft acids and bases (HSAB) theory[45,

[46]. Moreover, the adsorption mechanism of heavy metal ions adsorbed by COF-ChM mainly depends on the combination of strong chemical interactions and physical interactions (electrostatic interaction). These suggested that coordination interaction between metal ions and functional groups played a greater role in adsorption process.

3.4 Conclusions

In summary, this work has presented a novel COF monolith membrane using chitosan and COF as precursors via the freeze-casting method. Through loading COF into biomimetic honeycomb chitosan membrane, hierarchical porous structure was introduced, which avoided the highly stacked nature of COF and made readily take advantage of their complete structure especially the inside of COF. Consequently, the COF monolith membrane has shown higher adsorptive rate in comparison with that of amorphous COF in metal ions adsorption. Furthermore, its preparation process was very simple, starting materials were inexpensive and possess well processability. The resulting material COF monolith membrane possessed outstanding performance in heavy metal adsorption and demonstrating a great potential on in-depth processing of amorphous COF.

3.5 References

1. A. Feinle, M. S. Elsaesser, N. Husing, Sol-gel synthesis of monolithic materials with hierarchical porosity. Chem. Soc. Rev. 45(2016) 3377-3399
2. N. D. Petkovich, A. Stein, Controlling macro- and mesostructures with hierarchical porosity through combined hard and soft templating. Chem. Soc. Rev. 42(2013) 3721-3739
3. Y. Zhou, J. H. Schattka, M. Antonietti, Room-temperature ionic liquids as template to monolithic mesoporous silica with wormlike pores via a sol-gel nanocasting technique. Nano Lett. 4(2001) 477-481
4. Y. Li, Y. Chen, R. Xiang, et al., Incorporation of single-wall carbon nanotubes into an organic polymer monolithic stationary phase for mu-HPLC and capillary electrochromatography. Anal. Chem. 77(2005) 1398-1406
5. F. Svec, Preparation and HPLC applications of rigid macroporous organic polymer monoliths. J. Sep. Sci. 27(2004) 747-766
6. F. Svec, Organic polymer monoliths as stationary phases for capillary HPLC. J. Sep. Sci. 27(2004) 1419-1430
7. A. Dong, N. Ren, W. Yang, et al., Preparation of hollow zeolite spheres and three-dimensionally ordered macroporous zeolite monoliths with functionalized interiors. Adv. Funct. Mater. 13(2003) 943-948
8. A. Dong, Y. Wang, Y. Tang, et al., Mechanically stable zeolite monoliths with three-dimensional ordered macropores by the transformation of mesoporous silica spheres. Adv. Mater. 14(2002) 1506-1510
9. C. Moreno-Castilla, A. Pérez-Cadenas, Carbon-based honeycomb monoliths for environmental gas-phase applications. Materials 3(2010) 1203-1227
10. M. Ouzzine, G. A. Cifredo, J. M. Gatica, et al., Original carbon-based honeycomb monoliths as support of Cu or Mn catalysts for low-temperature SCR of NO: Effects of preparation variables. Appl. Catal., A 342(2008) 150-158

11. H. Zhu, Q. Zhang, S. Zhu, Assembly of a metal-organic framework into 3D hierarchical porous monoliths using a pickering high internal phase emulsion template. Chem. - Eur. J. 22(2016) 8751-8755
12. G. Guiochon, Monolithic columns in high-performance liquid chromatography. J. Chromatogr. A 1168(2007) 101-168
13. E. Peters, M. Petro, F. Svec, et al., Molded rigid polymer monoliths as separation media for capillary electrochromatography. Anal. Chem. 69(1997) 3646-3649
14. R. Heck, S. Gulati, R. Farrauto, The application of monoliths for gas phase catalytic reactions. Chem. Eng. J. 82(2001) 149-156
15. Y. S. Hu, P. Adelhelm, B. M. Smarsly, et al., Synthesis of hierarchically porous carbon monoliths with highly ordered microstructure and their application in rechargeable lithium batteries with high-rate capability. Adv. Funct. Mater. 17(2007) 1873-1878
16. G. P. Hao, W. C. Li, D. Qian, et al., Rapid synthesis of nitrogen-doped porous carbon monolith for CO2 capture. Adv. Mater. 22(2010) 853-857
17. J.-W. Kim, K. Taki, S. Nagamine, et al., Preparation of poly(L-lactic acid) honeycomb monolith structure by unidirectional freezing and freeze-drying. Chem. Eng. Sci. 63(2008) 3858-3863
18. Z. Z. Pan, H. Nishihara, S. Iwamura, et al., Cellulose nanofiber as a distinct structure-directing agent for xylem-like microhoneycomb monoliths by Unidirectional freeze-drying. ACS nano 10(2016) 10689-10697
19. ZQ. Zhao, DR. Chen, J. XL, Zirconia aerogels with high surface area derived from sols prepared by electrolyzing zirconium oxychloride solution: comparison of aerogels prepared by freeze-drying and supercritical CO2(l) extraction. J. Phys. Chem. C 111(2007) 18738-18743
20. H. M. El-Kaderi, J. R. Hunt, J. L. Mendoza-Cortes, et al., Designed synthesis of 3D covalent organic frameworks. Science 316(2007) 268-272
21. S. Y. Ding, W. Wang, Covalent organic frameworks (COFs): from design to applications. Chem. Soc. Rev. 42(2013) 548-568

22. X. Feng, X. Ding, D. Jiang, Covalent organic frameworks. Chem. Soc. Rev. 41(2012) 6010-6022
23. A. P. Cote, A. I. Benin, N. W. Ockwig, et al., Porous, crystalline, covalent organic frameworks. Science 310(2005) 1166-1170
24. H. Lu, C. Wang, J. Chen, et al., A novel 3D covalent organic framework membrane grown on a porous alpha-Al2O3 substrate under solvothermal conditions. Chem. Commun. 51(2015) 15562-15565
25. S. Ding, J. Gao, Q. Wang, et al., Construction of covalent organic framework for catalysis: Pd/COF-LZU1 in Suzuki-Miyaura coupling reaction. J. Am. Chem. Soc. 133(2011) 19816-19822
26. S. Lin;, C. S. Diercks;, Y. Zhang;, et al., Covalent organic frameworks comprising cobalt porphyrins for catalytic CO2 reduction in water. Science 349(2015) 1208-1213
27. S. Y. Ding, M. Dong, Y. W. Wang, et al., Thioether-based fluorescent covalent organic framework for selective detection and facile removal of mercury(II). J. Am. Chem. Soc. 138(2016) 3031-3037
28. L. Sheng, L. Zhou, Z. Huang, et al., Facile synthesis of magnetic chitosan nano-particles functionalized with N/O-containing groups for efficient adsorption of U(VI) from aqueous solution. J. Radioanal. Nucl. Chem. 310(2016) 1361-1371
29. J. Meng, J. Cui, J. Yu, et al., Preparation of green chelating fibers and adsorption properties for Cd(II) in aqueous solution. J. Mater. Sci. 53(2017) 2277-2289
30. Y. Li, C. Wang, S. Ma, et al., Fabrication of hydrazone-linked covalent organic frameworks using alkyl amine as building block for high adsorption capacity of metal ions. ACS Appl. Mater. Interfaces 11(2019) 11706-11714
31. L. Zhang, S. Ma, Y. Chen, et al., Facile fabrication of biomimetic chitosan membrane with honeycomb-like structure for enrichment of glycosylated peptides. Anal. Chem. 91(2019) 2985-2993
32. Z. Liu, H. Wang, J. Ou, et al., Construction of hierarchically porous monoliths from covalent organic frameworks (COFs) and their application for bisphenol A removal. J.

Hazard. Mater. 355(2018) 145-153

33. N. Wang, D. Yang, X. Wang, et al., Highly efficient Pb(II) and Cu(II) removal using hollow Fe3O4@PDA nanoparticles with excellent application capability and reusability. Inorg. Chem. Front. 5(2018) 2174-2182
34. K. Zhu, C. Chen, H. Xu, et al., Cr(VI) reduction and immobilization by core-double-shell structured magnetic polydopamine@zeolitic idazolate frameworks-8 microspheres. ACS Sustainable Chem. Eng. 5(2017) 6795-6802
35. W. Tu, W. Cai, Y. Jiang, et al., Facile synthesis of novel rare-rarth elements-modified SiO2 films for effective Cr(VI) removal from electroplating effluent. J. Chem. Eng. Data 64(2019) 2677-2685
36. S. Karak, K. Dey, A. Torris, et al., Inducing disorder in order: hierarchically porous covalent organic oramework nanostructures for rapid removal of persistent organic pollutants. J. Am. Chem. Soc. 141(2019) 7572-7581
37. Q. Sun, B. Aguila, L. D. Earl, et al., Covalent organic frameworks as a decorating platform for utilization and affinity enhancement of chelating sites for radionuclide sequestration. Adv. Mater. 30(2018) 1-9
38. H. Chen, Y. Zhou, J. Wang, et al., Polydopamine modified cyclodextrin polymer as efficient adsorbent for removing cationic dyes and Cu2+. J. Hazard. Mater. 389(2020)
39. S. Wang, K. Xiao, Y. Mo, et al., Selenium(VI) and copper(II) adsorption using polyethyleneimine-based resins: Effect of glutaraldehyde crosslinking and storage condition. J. Hazard. Mater. 386(2020)
40. C. Xu, S. Shi, X. Wang, et al., Electrospun SiO2-MgO hybrid fibers for heavy metal removal: Characterization and adsorption study of Pb(II) and Cu(II). J. Hazard. Mater. 381(2020)
41. N. Li, Z. Li, L. Zhang, et al., One-step fabrication of bifunctional self-assembled oligopeptides anchored magnetic carbon nanoparticles and their application in copper (II) ions removal from aqueous solutions. J. Hazard. Mater. 382(2020)
42. L. Chaabane, E. Beyou, A. El Ghali, et al., Comparative studies on the adsorption of metal

ions from aqueous solutions using various functionalized graphene oxide sheets as supported adsorbents. J. Hazard. Mater. 389(2020)

43. W. Zhang, J. Song, Q. He, et al., Novel pectin based composite hydrogel derived from grapefruit peel for enhanced Cu(II) removal. J. Hazard. Mater. 384(2020)

1. A. Feinle, M. S. Elsaesser and N. Husing, *Chem. Soc. Rev.* 2016, **45**, 3377–3399.
2. N. D. Petkovich and A. Stein, *Chem. Soc. Rev.* 2013, **42**, 3721–3739.
3. Y. Zhou, J. H. Schattka and M. Antonietti, *Nano Lett.* 2001, **4**, 477–481
4. Y. Li, Y. Chen, R. Xiang, D. Ciuparu, L. Pfefferle, C. Horwath and J. Wilkins, *Anal. Chem.* 2005, **77**, 1398–1406.
5. F. Svec, *J. Sep. Sci.* 2004, **27**, 747–766.
6. F. Svec, *J. Sep. Sci.* 2004, **27**, 1419–1430.
7. A. Dong, N. Ren, W. Yang, Y. Wang, Y. Zhang, D. Wang, H. Hu, Z. Gao and Y. Tang, *Adv. Funct. Mater.* 2003, **13**, 943–948.
8. A. Dong, Y. Wang, Y. Tang, Y. Zhang, N. Ren and Z. Gao, *Adv. Mater.* 2002, **14**, 1506–1510.
9. C. Moreno-Castilla and A. Pérez-Cadenas, *Materials* 2010, **3**, 1203–1227.
10. M. Ouzzine, G. A. Cifredo, J. M. Gatica, S. Harti, T. Chafik and H. Vidal, *Appl. Catal., A* 2008, **342**, 150–158.
11. H. Zhu, Q. Zhang and S. Zhu, *Chem. - Eur. J.* 2016, **22**, 8751–8755.
12. G. Guiochon, *J. Chromatogr. A* 2007, **1168**, 101–168.
13. E. Peters, M. Petro, F. Svec and J. Frechet, *Anal. Chem.* 1997, **69**, 3646–3649.
14. R. Heck, S. Gulati and R. Farrauto, *Chem. Eng. J.* 2001, **82**, 149–156.
15. Y. S. Hu, P. Adelhelm, B. M. Smarsly, S. Hore, M. Antonietti and J. Maier, *Adv. Funct. Mater.* 2007, **17**, 1873–1878.
16. G. P. Hao, W. C. Li, D. Qian and A. H. Lu, *Adv. Mater.* 2010, **22**, 853–857.
17. J.-W. Kim, K. Taki, S. Nagamine and M. Ohshima, *Chem. Eng. Sci.* 2008, **63**, 3858-3863.
18. Z. Z. Pan, H. Nishihara, S. Iwamura, T. Sekiguchi, A. Sato, A. Isogai, F. Kang, T. Kyotani and Q. H. Yang, *ACS nano* 2016, **10**, 10689–10697.

19. ZQ. Zhao, DR. Chen and J. XL, *J. Phys. Chem. C* 2007, **111**, 18738–18743.
20. H. M. El-Kaderi, J. R. Hunt, J. L. Mendoza-Cortes, A. P. Cote, R. E. Taylor, M. O'Keeffe and O. Yaghi, *Science* 2007, **316**, 268–272.
21. S. Y. Ding and W. Wang, *Chem. Soc. Rev.* 2013, **42**, 548–568.
22. X. Feng, X. Ding and D. Jiang, *Chem. Soc. Rev.* 2012, **41**, 6010–6022.
23. A. P. Cote, A. I. Benin, N. W. Ockwig, M. O'Keeffe, A. J. Matzger and O. M. Yaghi, *Science* 2005, **310**, 1166–1170.
24. H. Lu, C. Wang, J. Chen, R. Ge, W. Leng, B. Dong, J. Huang and Y. Gao, *Chem. Commun.* 2015, **51**, 15562–15565.
25. S. Ding, J. Gao, Q. Wang, Y. Zhang, W. Song, C. Su and W. Wang, *J. Am. Chem. Soc.* 2011, **133**, 19816–9822.
26. S. Lin, C. S. Diercks, Y. Zhang, N. Kornienko, E. M. Nichols, Y. Zhao, A. R. Paris, D. Kim, P. Yang, O. M. Yaghi and C. J. Chang, *Science* 2015, **349**, 1208–1213
27. S. Y. Ding, M. Dong, Y. W. Wang, Y. T. Chen, H. Z. Wang, C. Y. Su and W. Wang, *J. Am. Chem. Soc.* 2016, **138**, 3031–3037.
28. L. Sheng, L. Zhou, Z. Huang, Z. Liu, Q. Chen, G. Huang and A. A. Adesina, *J. Radioanal. Nucl. Chem.* 2016, **310**, 1361–1371.
29. J. Meng, J. Cui, J. Yu, W. Huang, P. Wang, K. Wang, M. Liu, C. Song and P. Chen, *J. Mater. Sci.* 2017, **53**, 2277–2289.
30. Y. Li, C. Wang, S. Ma, H. Zhang, J. Ou, Y. Wei and M. Ye, *ACS Appl. Mater. Interfaces* 2019, **11**, 11706–11714.
31. L. Zhang, S. Ma, Y. Chen, Y. Wang, J. Ou, H. Uyama and M. Ye, *Anal. Chem.* 2019, **91**, 2985–2993.
32. Z. Liu, H. Wang, J. Ou, L. Chen and M. Ye, *J. Hazard. Mater.* 2018, **355**, 145–153.
33. N. Wang, D. Yang, X. Wang, S. Yu, H. Wang, T. Wen, G. Song, Z. Yu and X. Wang, *Inorg. Chem. Front.* 2018, **5**, 2174–2182.
34. K. Zhu, C. Chen, H. Xu, Y. Gao, X. Tan, A. Alsaedi and T. Hayat, *ACS Sustainable Chem. Eng.* 2017, **5**, 6795–6802.

35. W. Tu, W. Cai, Y. Jiang, F. Kong and J. Zhou, *J. Chem. Eng. Data* 2019, **64**, 2677–2685.
36. S. Karak, K. Dey, A. Torris, A. Halder, S. Bera, F. Kanheerampockil and R. Banerjee, *J. Am. Chem. Soc.* 2019, **141**, 7572–7581.
37. Q. Sun, B. Aguila, L. D. Earl, C. W. Abney, L. Wojtas, P. K. Thallapally and S. Ma, *Adv. Mater.* 2018, **30**, 1–9.
38. H. Chen, Y. Zhou, J. Wang, J. Lu and Y. Zhou, *J. Hazard. Mater.* 2020, **389**, 121897.
39. S. Wang, K. Xiao, Y. Mo, B. Yang, T. Vincent, C. Faur and E. Guibal, *J. Hazard. Mater.* 2020, **386**, 121637.
40. C. Xu, S. Shi, X. Wang, H. Zhou, L. Wang, L. Zhu, G. Zhang and D. Xu, *J. Hazard. Mater.* 2020, **381**, 120974.
41. N. Li, Z. Li, L. Zhang, H. Shi, J. Li, J. Zhang, Z. Zhang and F. Dang, *J. Hazard. Mater.* 2020, **382**, 121113.
42. L. Chaabane, E. Beyou, A. El Ghali and M. H. V. Baouab, *J. Hazard. Mater.* 2020, **389**, 121839.
43. W. Zhang, J. Song, Q. He, H. Wang, W. Lyu, H. Feng, W. Xiong, W. Guo, J. Wu and L. Chen, *J. Hazard. Mater.* 2020, **384**, 121445.
44. M. Choudhary, R. Kumar and S. Neogi, *J. Hazard. Mater.* 2020, **392**, 122441.
45. R. Pearson, *J. Am. Chem. Soc.* 1963, **85**, 3533–3539.
46. R. Pearson and J. Songstad, *J. Am. Chem. Soc.* 1967, **89**, 1827–1836.

Concluding Remarks

In this doctoral dissertation, three biomimetic hierarchical monolithic materials were prepared by thermally induced phase separation and freeze-drying. The prepared materials have good permeability and have good application potential in enriching glycopeptides, phosphopeptides and adsorbing heavy metal ions.

In chapter 1, the biomimetic coral-like TiO_2-CM material was prepared by sol-gel method using an environmentally friendly cellulose monolith as template. The combination of inorganic TiO_2 and organic cellulose achieves high mechanical strength by imitating composition of nacre. The obtained TiO_2-CM has high mechanical strength and stability, avoiding the tedious centrifugation process in the enrichment process. The highly permeable skeleton structure improves the mass transfer efficiency between the material and the peptide, and the high specific surface area increases the active site for adsorbing the peptide. The prepared TiO_2-CM exhibited high selectivity, high detection limit and reusability for phosphopeptides. and was successfully used to enrich phosphopeptides from complex biological samples. And TiO_2-CM was successfully used to enrich phosphopeptides from complex biological samples, proving its application potential in enriching phosphopeptides.

In the chapter 2, a hierarchical porous monolith TiPCM with coral-like structure was prepared using green and inexpensive cellulose monoliths as precursors. After the cellulose monolith was phosphorylated, the obtained TiPCM exhibited satisfactory hydrophilicity. In addition, the phosphate groups on the cellulose surface chelated a large amount of titanium ions, which enabled TiPCM to simultaneously enrich glycopeptides and phosphopeptides. The coral-like structure of TiPCM increases the permeability, improves the mass transfer rate between the material and the peptide, and greatly reduces the steric effect between the peptide and the material. And its rough surface provides a large number of adsorption sites. TiPCM exhibits excellent selective specificity and detection sensitivity for both phosphopeptides and glycopeptides, and has reusability for phosphopeptides. TiPCM was successfully enriched phosphopeptides and glycopeptides from complex samples, and TiPCM has good application

potential in phosphorylation and glycosylation analysis.

In chapter 3, a COF monolith ChM-COF was prepared using chitosan monolith with honeycomb-like structure as precursors. COFs with mesoporous structure are grown on the surface of chitosan monolith macropores, introducing a hierarchical porous structure, avoiding the highly stacked nature of COFs, and making it easy to utilize their complete structures, especially the core of COFs. Therefore, compared with amorphous COFs, ChM-COF exhibit higher adsorption rates in metal ion adsorption. In addition, its preparation process is very simple, the starting materials are cheap, and it has good processability. The resulting ChM-COF has good heavy metal adsorption capacity and has good potential for amorphous COF processing.

In summary, the thesis developed three efficient strategies for fabricating biomimetic monolith with hierarchical porous structures. The research in this thesis demonstrated the biomimetic monolithic material has a great potential for the application of adsorbent material. The methods established in this thesis may provide guidance for the future development of phosphorylation analysis, glycosylation analysis and deep processing of COF.

List of Publications

1. Robust dual-biomimetic titanium dioxide-cellulose monolith for enrichment of phosphopeptide

Luwei Zhang, Yan Wang, Wanjun Zhang, Yu-I Hsu*, Taka-Aki Asoh, Baoyun Qi*, and Hiroshi Uyama*

ACS Biomaterials Science & Engineering, **2022**, 8, 2676–2683

DOI: 10.1021/acsbiomaterials.2c00385

2. Fabrication of a reusable bifunctional biomimetic Ti^{4+}-phosphorylated cellulose monolith with a coral-like structure for enrichment of phosphorylated and glycosylated peptides

Luwei Zhang, Yan Wang, Lei Pan, Ruizhi Tang, Taka-Aki Asoh*, Junjie Ou, and Hiroshi Uyama*

Green Chemistry, **2021**, 23, 7674−7684.

DOI: 10.1039/D1GC02206G

3. Integration of covalent organic frameworks into hydrophilic membrane with hierarchical porous structure for fast adsorption of metal ions

Luwei Zhang, Ya Li, Yan Wang, Shujuan Ma*, Junjie Ou*, Yehua Shen, Mingliang Ye, and Hiroshi Uyama

Journal of Hazardous Materials, **2021**, 407, 124390.

DOI: 10.1016/j.jhazmat.2020.124390

Acknowledgments

First, I would like to express my deepest appreciation to my supervisor, Prof. Hiroshi Uyama. I am very thankful to him for giving me opportunity to study at Osaka University. I learned a lot from him. This thesis would not have been possible without his support and help. His positive and optimistic attitude towards scientific research and life has deeply influenced me. Besides my supervisor, I would like to thank Prof. Norimitsu Tohnai and Prof. Masaya Nogi. Their insightful comments were very helpful in improving the quality of my dissertation. I also want to thank Assoc. Prof. Taka-aki Asoh, he is always passionate about his work and helped me a lot in experiments and paper writing. I want to appreciate Assoc. Prof. Yu-I Hsu for her kind help to improve the quality of my paper and dissertation. And I want to appreciate Assist. Prof. Akihide Sugawara for his kind help on revise my defense slides and dissertation. He gives me many wonderful memories. And I would like to thank Prof. Junjie Ou and Prof. Wanjun Zhang. Thanks for their help with my experiments in analyzing biological samples.

I really want to thank Ms. Yoko Uenishi and Ms. Tomoko Shimizu for their kind help during these three years. I am very thankful to the support of past and present members in Uyama Lab: Dr. Yasushi Takeuchi, Dr. Xinnan Cui, Dr. Chen Qian, Dr. Toshiki Tamiya, Dr. Shunsuke Mizuno, Dr. Naharullah Bin Jamaluddin, Dr. Raghav Soni, Mr. Mark Adam Malaluan Ferry, Mr. Yuxiang Jia, Ms. Juan Wang, Mr. Peng Du, Mr. Emil Hajili, Ms. Madhurangika Panchabashini Horathal Pedige, Mr. Kazuki Shibasaki, Ms. Zeying Cao, Ms. Linxuan Li, Ms. Xunran Guo, Ms. Jiaxin Chen, Ms. Guan Wang, Ms. Ying Yao, Mr. Toshiki Honda, Ms. Airi Ozaki, Mr. Yuya Fujiwara, Ms. Yuka Kashihara, Mr. Yuji Kiba, Mr. Takeshi Hiraoka, Mr. Atsushi Koizumi, Mr. Yuki Shioji, Mr. Nontarin Roopsung, Ms. May Myat Noe, Ms. Hasinah Binti Mohamed Rafiq, Ms. Judit Rebeka Molnar, Ms. Izzah Durrati Binti Haji Abdul Hamid, Ms. Sooyeon Noh, Ms. Thuy Le Huynh An, Mr. Motoi Oda, Ms. Suzune Miki, Mr. Kaita Kikuchi, Mr. Koki Tsujita, Mr. Hajime Fujimori, Ms. Rika Onishi, Mr. Shotaro Yano, Ms. Rina Kugimiya, Ms. Kyoko Tanimura, Ms. Chikabo Abe, Ms. Erina Katsuragawa, Mr. Yasushi Takeuchi, Mr. Atsuki Takagi and etc. for their kind-hearted help in my lab and daily life.

And I would like to thank Dr. Xiaowei Li, Mr. Ruizhi Tang and Ms. Lei Pan. We often

discuss experimental details together. And really thanks for their help with my experiments in analyzing biological samples.

I would like to thank Dr. Bozhi Chen, Dr. Yankun Jia, Dr. Zhengtian Xie, Dr. Haomin Yan, Dr. Hanyu Wen, Dr. Yanting Lyu, Ms. Meng Wei, Mr. Junyi Han and Ms. Manjie He. We have a lot of nice memories in Japan. Thanks to the members of the non-official organization Osaka University Chinese Lure Club, we successfully caught tuna, hope we can catch the great marlin together in the future.

I would like to thanks to my family members. They always support me when I need help and care. I would like to thank my wife Yan Wang, we are the best partners, whether in research or life, with you by my side, I have nothing to fear (except for the roller coaster and waves over 5 meters).

Finally, I would like to appreciate the China Scholarship Council for the constant support for me and my wife during these three years.

June 2022

ZHANG LUWEI